



저작자표시-비영리-변경금지 2.0 대한민국

이용자는 아래의 조건을 따르는 경우에 한하여 자유롭게

- 이 저작물을 복제, 배포, 전송, 전시, 공연 및 방송할 수 있습니다.

다음과 같은 조건을 따라야 합니다:



저작자표시. 귀하는 원저작자를 표시하여야 합니다.



비영리. 귀하는 이 저작물을 영리 목적으로 이용할 수 없습니다.



변경금지. 귀하는 이 저작물을 개작, 변형 또는 가공할 수 없습니다.

- 귀하는, 이 저작물의 재이용이나 배포의 경우, 이 저작물에 적용된 이용허락조건을 명확하게 나타내어야 합니다.
- 저작권자로부터 별도의 허가를 받으면 이러한 조건들은 적용되지 않습니다.

저작권법에 따른 이용자의 권리는 위의 내용에 의하여 영향을 받지 않습니다.

이것은 [이용허락규약\(Legal Code\)](#)을 이해하기 쉽게 요약한 것입니다.

[Disclaimer](#)

**Doctor of Philosophy**

**Development of sodium titanate semiconductor for removal of organic dyes  
from aqueous solutions and hydrogen production using photoelectrochemical  
(PEC) water splitting**

**The Graduate School  
of the University of Ulsan**

**Department of civil and  
Environmental Engineering  
Morteza Kolaei**

**Development of sodium titanate semiconductor for removal of organic dyes  
from aqueous solutions and hydrogen production using photoelectrochemical  
(PEC) water splitting**

**Doctoral thesis submitted to the Department of Environmental Engineering  
University of Ulsan**

**By  
Morteza Kolaei**

**Supervised by Prof. Byeong-Kyu Lee**

**November 2021**

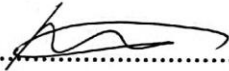
**Development of Sodium titanate semiconductor for removal of organic dyes  
from aqueous solutions and hydrogen production using photoelectrochemical  
(PEC) water splitting**

**This certified that this dissertation of**


**Morteza Kolaei is approved**

Committee Chairman: .....  



**Prof. Dae-seung Kyung**

Committee Member: .....  


**Prof. Sung-Deuk Choi**

Committee Member: .....  


**Prof. Eun-Woo Shin**

Committee Member: .....  


**Prof. Hung-Suck Park**

Committee Member: .....  


**Prof. Byeong-Kyu Lee**

**Department of civil and Environmental Engineering**

**Ulsan, South Korea**

**December 2021**

## **ACKNOWLEDGMENTS**

My first and big appreciation goes to my supervisor Prof. Byeong-Kyu Lee that took me on as a student and continued to have faith in me over the years. This work would not have been possible without his constant support, guidance, patience, and assistance.

I would also like to thank to all my friends in Environmental and Energy Research Laboratory members especially Dr. Meysam Tayyebi and Dr. Ahmad Tayyebi that kindly helped and shared their knowledge and living experience during my study in Korea.

Finally, my special thanks to my parents whose constant love and support keep me motivated and confident.

**Morteza Kolaei**

**November 2021**

## List of Publication

[1] **Morteza Kolaei**, Meysam Tayebi , Byeong-Kyu Lee

The synergistic effects of acid treatment and silver (Ag) loading for substantial improvement of photoelectrochemical and photocatalytic activity of Na<sub>2</sub>Ti<sub>3</sub>O<sub>7</sub>/TiO<sub>2</sub> nanocomposite, **Applied Surface Science** 540 (2021) 148359

[2] **Morteza Kolaei**, Meysam Tayebi, Zohreh Masoumi, Ahmad Tayyebi; Byeong-Kyu

Lee<sup>1,\*</sup>. Decoration of CdS nanoparticle on dense and multi edge sodium titanate nanorods to form a highly efficient and stable photoanode with great enhancement in PEC performance, **Environmental Science: Nano**, 2021,8, 1667-1679

## List of Conference

[1] **Morteza Kolaei**, Byeong-Kyu Lee

One-spot synthesis of TiO<sub>2</sub>-Graphene Nanocomposites for enhance Photocatalytic activity. . International Conference on Photocatalysis and Photoenergy 2019, poster presentation, May 22-25, 2019, Incheon, Korea.

[2] **Morteza Kolaei**, Meysam Tayeb, Byeong-Kyu Lee

ZnO/CdS/MoS<sub>2</sub> Photoanode with Multi-heterojunctions for Highly Efficient Photoelectrochemical Hydrogen Evolution. 4th International Conference on Bioresources, Energy, Environment, and Materials Technology (BEEM 2020), Oral presentation, Sep 6-9, 2020, Incheon, Korea.

## **Table of contents**

<b>Abstract .....</b>	<b>1</b>
<b>Thesis outline .....</b>	<b>2</b>
<b>Chapter 1: Introduction .....</b>	<b>3</b>
1.1. Wastewater treatment .....	3
1.2. Climate change .....	5
1.3. Basic of PEC water splitting .....	6
1.4. Sodium titanate .....	7
1.5. Improving of the photoelectrochemical and photocatalytic activity of sodium titanate .....	10
1.5.1. Acidic treatment with the assistance of ultrasonic waves .....	10
1.5.2. Loading of noble metal .....	11
1.5.3. Heterojunction with visible semiconductor .....	12
1.5.4. Optimization of NaOH concentration .....	12
References .....	14
<b>Chapter 2: Acid treatment and silver (Ag) loading, two different strategies for improvement of photoelectrochemical and photocatalytic activity sodium titanate .....</b>	<b>17</b>
Abstract .....	17
2.1. Introduction .....	18
2.2. Experimental procedure .....	21
2.2.1. Catalyst preparation .....	21
2.2.2. Photocatalytic degradation .....	22
2.2.3. Photoelectrochemical (PEC) measurement .....	22
2.3. Results and discussion .....	23
2.3.1. Characterization of the synthesized photocatalysts .....	23
2.3.2. Photocatalytic properties .....	31

2.3.3. Photoelectrochemical (PEC) properties .....	38
2.4. Conclusion: .....	42
Reference: .....	44
<b>Chapter 3: Heterojunction of sodium titanate nanorods with visible semiconductor .....</b>	<b>47</b>
<b>(CdS nanoparticle).....</b>	<b>47</b>
Abstract.....	47
3.1. Introduction .....	47
3.2. Experimental procedure.....	50
3.2.1. Catalyst preparation .....	50
3.2.2. Photoelectrochemical (PEC) performance .....	50
3.3. Results and discussion .....	51
3.3.1. Characterization of the synthesized photoanodes.....	51
3.3.2. Photoelectrochemical (PEC) properties .....	60
3.3.3. Mechanism of PEC enhancement .....	67
3.4. Conclusion .....	68
Reference: .....	70
<b>Chapter 4: The effect of NaOH concentration on growth of sodium titanate nanoflower on TiO<sub>2</sub> thin film.....</b>	<b>73</b>
Abstract.....	73
4.1. Introduction .....	74
4.2. Experimental procedure.....	76
4.2.1. Preparation of Photoelectrodes.....	76
4.2.2. PEC measurement.....	77
4.3. Results and discussion .....	78
4.3.1. Characterization results .....	78
4.3.2. Photoelectrochemical (PEC) Properties .....	88



4.3.3. Measurement of evolved H <sub>2</sub> and O <sub>2</sub> .....	102
4.3.4. Mechanism of PEC performance enhancement .....	102
4.4. Conclusions .....	103
Reference: .....	105
<b>Conclusion .....</b>	<b>108</b>

## Table of Figures

### Chapter 1

Figure1. 1 Possible mechanism for photocatalytic degradation of dye .....	5
Figure1. 2 The mechanism and principle of Photoelectrochemical cell[9] .....	7
Figure1. 3 Band gap and band-edge energy level of sodium titanate and water splitting ability. 10	

### Chapter 2

Figure 2. 1 (a) XRD patterns of NTO, NTOH0.01, NTOH0.05, NTOH0.1, and NTOH0.1/Ag0.5, (b) Raman spectra of NTO, NTOH0.1, and NTOH0.1/Ag0.5.....	24
Figure 2. 2. (a) XPS survey spectra of samples and high-resolution XPS spectra of (b) Ti, (c) NTOH0.1/Ag0.3, (d) NTOH0.1/Ag0.5, (e) NTOH0.1/Ag1 and (f) NTOH0.1/Ag2 .....	27
Figure 2. 3 UV-Vis diffuse reflectance spectra of (a) NTO, NTOH0.1, and NTOH0.1/Ag0.5 and (b) NTOH0.1/Ag with varying Ag loading (0.3, 0.5, 1, and 2 wt%).....	28
Figure 2. 4 (a) SEM image of NTO, (b) EDX analysis of NTO, (c) SEM image of NTOH0.05, (d) EDX analysis of NTOH0.05, (e) SEM image of NTOH0.1, and (f) EDX analysis of NTOH0.1 .....	30
Figure 2. 5. (a) and (b) TEM image of NTO, (c) and (d) TEM image of NTOH0.1 .....	31
Figure 2. 6. (a) Effect of HCl concentration on photocatalytic activity of NTO, (b) Photodegradation of RhB by NTO under 150 w Xe lamp (c). PI spectra of NTO and NTOH0.1 photocatalysts, and (d) photocatalytic degradation of RhB by NTO, NTOAg0.5, NTOH0.1, and NTOH0.1/Agx .....	33
Figure 2. 7 Reusability test of NTOH0.1/Ag0.5.....	34
Figure 2. 8. Photocatalytic degradation of RhB on NTOH0.1/Ag0.5 with addition of different scavengers. ....	36
Figure 2. 9. Schematic model illustrating the surface of the photocatalyst and the degradation of RhB (a) before acid treatment, and (b) after acid treatment and silver loading.....	38
Figure 2. 10. (a) Photocurrent response at a potential of 0.3 V (vs. Ag/AgCl), (b) EIS Nyquist plot, and (c) Mott–Schottky plot of the NTO, NTOH0.1, and NTOH0.1/Ag0.5 electrodes under 100 mW.cm <sup>-2</sup> irradiation; the supporting electrolyte was a 0.5M aqueous solution of Na <sub>2</sub> SO <sub>3</sub> .40	

### Chapter 3

Figure 3. 1. (a) XRD patterns of Ti foil, NTO and NTO/CdS12, (b) Raman spectra of NTO, (c) Raman spectra of NTO/CdS12 .....	52
Figure 3. 2. XPS survey spectra of (a) NTO, (b) NTO/CdS12 and high-resolution XPS spectra of (c) Cd, (d) S, (e) Ti and (f) O, valance band edge for (g) pure NTO and (h) CdS .....	55
Figure 3. 3. (a) UV-Vis diffuse reflectance spectra and (b) PL spectra of NTO, NTO/CdS7, NTO/CdS9, NTO/CdS12, NTO/CdS15.....	56
Figure 3. 4. SEM image of (a) NTO, (c) NTO/CdS9, (e) NTO/CdS12, (g) NTO/CdS15 and EDX analysis (b) NTO, (d) NTO/CdS9, (f) NTO/CdS12, (h) NTO/CdS15.....	58
Figure 3. 5. TEM images of a) NTO and b) NTO/CdS12, c) HRTEM image of NTO/CdS12 and d) elemental mapping of NTO/CdS12 photoelectrode. The inset is the corresponding selected area electron diffraction (SAED) patterns of NTO/CdS12.....	60

Figure 3. 6. Linear sweep voltammetry (LSV) of NTO and NTO/CdSx photoelectrodes under (a) continuous and (b) chopped illumination .....	61
Figure 3. 7. (a) photocurrent response at the potential of 1 V vs. RHE, (b) long time photocurrent stability of NTO/CdS12 photoanode .....	62
Figure 3. 8. (a) Transient OCP and (b) EIS Nyquist plot of NTO and NTO/CdSx photoanodes. 63	
Figure 3. 9. Mott–Schottky plot of NTO and NTO/CdSx photoanodes .....	65
Figure 3. 10. (a) Photoconversion efficiency as a function of applied voltage vs RHE for NTO and NTO/CdSx photoanodes and (b) IPCE spectra of NTO and NTO/CdS12 photoanodes at 1 V vs. RHE.....	66
Figure 3. 11. (a) H2 and (b) O2 evolution vs. reaction time per illuminated area (1cm2) for NTO and the NTO/CdS12 electrodes at a potential of 1V (vs. RHE). Under 100 mW.cm-2 irradiation, electrolyte was a 0.5M (PH=9) aqueous solution of Na2SO3.....	67
Figure 3. 12. Possible mechanism for enhanced PEC performance and photogenerated charge carrier transfer over NTO/CdSx electrodes. ....	68

## Chapter 4

Figure 4. 1. XRD patterns of (a) Ti+H0.25M, (b) 500oC-6h, (c) 500oC-6h+H0.25M, (d) 500oC-6h+H2M and (e) 500oC-6h+H4M (f) JCPDS Card.no of TiO2 Anatase (JCPDS Card no.21-1272), TiO2 Rutile (JCPDS Card no.21-1276), TiO2 Brookite (JCPDS Card no.29-1360), Sodium titanate (JCPDS Card no.31-1329) and Ti (JCPDS Card no.65-3362) .....	79
Figure 4. 2 UV-Vis diffuse reflectance spectra of (a) Ti+H0.25M, 500oC-6h, 500oC-6h+H0.25M, 500oC-6h+H2M and 500oC-6h+H4M (b) High resolution UV-Vis diffuse reflectance spectra of 500oC-6h, 500oC-6h+H0.25M and 500oC-6h+H2M samples .....	80
Figure 4. 3. Estimated bandgap energy of (a) Ti+H0.25M and (b) 500oC-6h .....	81
Figure 4. 4. XPS survey spectra of (a) all samples, high-resolution XPS spectra of (b) Na, (c) O for 500oC-6h, (d) O for 500oC-6h+H2M, (e) Ti for 500oC-6h, (f) Ti for 500oC-6h+H2M and (g) XPS valence band .....	83
Figure 4. 5. SEM image of (a), (b) and (c) Ti+H0.25M, (d) and (e) 500oC-6h, (f) 500oC-6h+H0.25M, (g), (h), (i) and (j) 500oC-6h+H2M and (k), (l), (m) and (n) 500oC-6h+H4M .....	85
Figure 4. 6. (a) 500oC-6h + H2M EDX analysis, (b) elemental mapping of 500oC-6h+H2M, (c) EDX analysis of 500oC-6h+H4M, (d) elemental mapping of 500oC-6h+H4M .....	87
Figure 4. 7. PL spectra of 500oC-6h and 500oC-6h+H2M .....	87
Figure 4. 8. (a) and (b) LSV dark illumination, LSV of (c) 500oC-1h, 500oC-3h and 500oC-6h samples and (d) Ti+H0.25M, 500oC-6h, 500oC-6h+H0.25M, 500oC-6h+H2M, 500oC-6h+H4M samples, (e) and (f) LSV chopped illumination of different photoanodes. ....	90
Figure 4. 9. (a) Photocurrent response at the potential of 0.3 V versus Ag/AgCl and (b) long time stability of 500oC-6h+H2M.....	91
Figure 4. 10. SEM image of 500oC-6h + H2M after 4 h chronoamperometric measurement. ....	92
Figure 4. 11. (a) Transient OCP and (b) EIS Nyquist plot of Ti+H0.25M, 500oC-6h, 500oC-6h+H0.25M, 500oC-6h+H2M, 500oC-6h+H4M samples.....	93
Figure 4. 12. Mott-Schottky plot of 500oC-6h, 500oC-6h+H0.25M, 500oC-6h+H2M and 500oC-6h+H4M at different frequencies (a) 1000HZ, (b) 500 HZ, (C) and (d) 100 HZ (a). ....	95
Figure 4. 13. (a) Photoconversion efficiency as a function of applied voltage versus Ag / AgCl and (b) IPCE spectra of different photoanodes at 0.3 V versus Ag / AgCl. ....	97

Figure 4. 14. XRD patterns of (a) 500oC-6h+H2M, (b) 500oC-6h+H2M+500oC (c) 500oC-6h+H2M+600oC, (d) 500oC-6h+H2M+700oC.....	99
Figure 4. 15. SEM images of (a) and (b) 500oC-6h+H2M+500oC, (c) and (d)500oC-6h+H2M+600oC, (d) and (f) 500oC-6h+H2M+700oC.....	100
Figure 4. 16. (a)Linear sweep voltammetry of the 500oC-6h+H2M, 500oC-6h+H2M+500oC, 500oC-6h+H2M+600oC and 500oC-6h+H2M+700oC photoanodes and (b) Linear sweep voltammetry of the 500oC-6h+H2M photoanode in different electrolyte solutions .....	101
Figure 4. 17. (a) Evolution of H2 and (b) O2 versus reaction time per illuminated area (1cm2) for Ti+H0.25M, 500oC-6h and 500oC-6h+H2M electrodes at a potential of 0.3V (versus Ag / AgCl). Under 100 mW.cm-2 irradiation, the electrolyte was an aqueous solution of Na2SO3 0.5M (PH = 10).....	102
Figure 4. 18. Possible transfer mechanism of photogenerated charge carriers in 500oC-6h+H2M photoanode.....	103

## List of Tables

### Chapter 2

Table 2. 1. Specific surface area, pore diameter, and pore volume of NTO and NTOH0.1 ..... 38

Table 2. 2. Summarized  $V_{fb}$  and  $N_D$  values obtained from the intercept and the slope in Mott-Schottky plots..... 42

### Chapter 3

Table 3. 1. Summarized  $V_{fb}$  and  $N_D$  values obtained from the intercept and the slope in Mott-Schottky plots..... 65

### Chapter 4

Table 4. 1. Calculated  $R_s$  and  $R_{ct}$  for different photoanodes using the Randles circuit model ... 93

Table 4. 2. Summarized  $V_{fb}$  and  $N_D$  values obtained from the X intercept and the slope in the Mott-Schottky plots ..... 95

## **Abstract**

The widespread presence of organic dyes in industrial waste- waters from the paper, textile and apparel industries results in substantial environmental contamination. Carcinogenic and toxic properties of dyes are harmful to human beings and aquatic life. Hence, the removal of dyes from waste- waters is of crucial importance. The photodegradation of pollutants has gained enormous popularity in the past several years. Degradation of pollutant by this method does not form the secondary toxic products and organic pollutants can be completely mineralized to relatively non-hazardous products (water and CO<sub>2</sub>). Another environment issue comes from emission of CO<sub>2</sub> from combustion of fossil fuels to produce energy that resulted in the global warming and global climate change issues. Photoelectrochemical (PEC) water splitting using semiconductor as a photoelectrode is one of the most promising routes for clean production of hydrogen. Hydrogen is most attractive and cleanest solar chemical fuel that does not result in any carbon emission during its oxidation in a fuel cell. Sodium titanate have been widely used as photocatalyst because of its high chemical inertness, low cost, abundance, lack of toxicity, thermal stability, and their proper band edge position for both photoelectrochemical water splitting and photocatalytic degradation of dye pollutant. However, some drawbacks of this type of photocatalyst such as inefficient usage of solar light due to its wide bandgap, low crystallinity, and High recombination rate of photogenerated electron and holes need to be solved. This thesis examines the effect of 4 strategies (acidic treatment with the assistance of ultrasonic waves, loading of noble metal, heterojunction with visible semiconductor, and optimization of NaOH concentration) to improve the photocatalytic and photoelectrochemical activity of sodium titanate for efficient degradation of organic pollutant and hydrogen production.

## **Thesis outline**

The aim of this thesis is to develop and understand an inexpensive, stable, and efficient photocatalytic semiconductor materials for improving photocatalytic wastewater treatment and photoelectrochemical water splitting H<sub>2</sub> production. Chapter 1 gives a general overview on environmental problems, principles of photocatalytic degradation of dye pollutant, and photoelectrochemical hydrogen production. Moreover, it briefly introduces sodium titanate and explains the reasons of the choice. In chapter 2 the effect of Ag loading and acid treatment on sodium titanate photocatalytic and Photoelectrochemical (PEC) activity is investigated. In chapter 3 we study the effect CdS decoration on sodium titanate nanorods to form a highly efficient and stable photoanode with great enhancement in PEC performance for hydrogen production. In chapter 4 we investigate the effect of NaOH concentration and Ti source (Ti foil and TiO<sub>2</sub> thin film) for growing optimum sodium titanate nanoflower to get the highest photoelectrochemical hydrogen production. Finally, chapter 5 concludes our research study.

# **Chapter 1: Introduction**

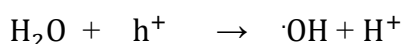
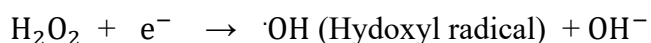
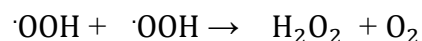
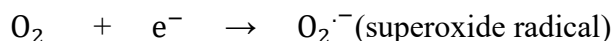
## **1.1. Wastewater treatment**

The widespread presence of organic dyes in industrial waste- waters from the paper, textile and apparel industries results in substantial environmental contamination. Several studies reported that 10–12% of dyes like Rhodamine B, Victoria blue, Rose Bengal, Eriochrome, Methylene Blue (MB), and Thymol blue are utilized annually in textile industries of which a major portion (20%) is lost during synthesis and processing operations and ends up in wastewater[1]. These dye-polluted effluents comprise non-biodegradable, highly poisonous, and colored pigments that are harmful to living organisms. The color of wastewater including dyes can prevent photosynthesis by aquatic plants and deteriorate water quality. In addition, the carcinogenic and toxic properties of dyes are harmful to human beings and aquatic life. Rhodamine B (RhB) is one of the most used dyes in the wastewaters of textile industries, which is sometimes discharged directly to rivers and lakes. Hence, the removal of dyes from waste- waters is important. Several strategies have been adopted to cope with this particular problem, including ozonation, membrane filtration, ion exchange removal, adsorption, photocatalytic degradation, catalytic reduction, biological/aerobic treatment and coagulation. The adsorption process is normally favored in terms of prerelease removal methodologies due to its ease of operation and economic cost. Though, the disadvantages like the low adsorption efficacy, incomplete removal of pollutants and poor mechanical stability of adsorbents create problems for the effective removal of pollutants. The photodegradation of pollutants has gained enormous popularity in the past several years. Photocatalysis is a catalytic oxidation process occurring on the surface of semiconductor photocatalyst materials by using the irradiation of sunlight to degrade various environmental contaminants, including aquatic and



atmospheric organic pollutants. Photodegradation provides advantages over the traditional wastewater treatment methods. For example, the complete degradation of organic pollutants by active photocatalysts can occur within a few hours at room temperature. Additionally, without the formation of the secondary toxic products, organic pollutants can be completely mineralized to relatively non-hazardous products (water and CO<sub>2</sub>). Furthermore, it is applied as an effective, easy-operated, green method with low cost to degrade the organic dyes pollutants.

Photocatalytic reaction is initiated when a photoelectron is promoted from the filled valence band of a semiconductor photocatalyst to the empty conduction band because of irradiation[2]. The absorbed photon has energy either equal or greater than the band gap of the semiconductor photocatalyst[3]. The excitation process leaves behind a hole in the valence band. The photogenerated holes at the valence band then react with water to produce OH<sup>•</sup> radical. The HO<sup>•</sup> radical formed on the irradiated semiconductor surface are extremely powerful oxidizing agent. While the photogenerated hole reacts with surface bound water or OH<sup>-</sup> to produce the hydroxyl radical, electron in the conduction is taken up by the oxygen in order to generate anionic superoxide radical (O<sub>2</sub><sup>•-</sup>). This superoxide ion may not only take part in the further oxidation process but also prevents the electron-hole recombination, thus maintaining electron neutrality within the semiconductor. The superoxide produced gets protonated forming hydroperoxyl radical (•OOH) and then subsequently H<sub>2</sub>O<sub>2</sub> which further dissociates into highly reactive hydroxyl radicals (•OH)[4].



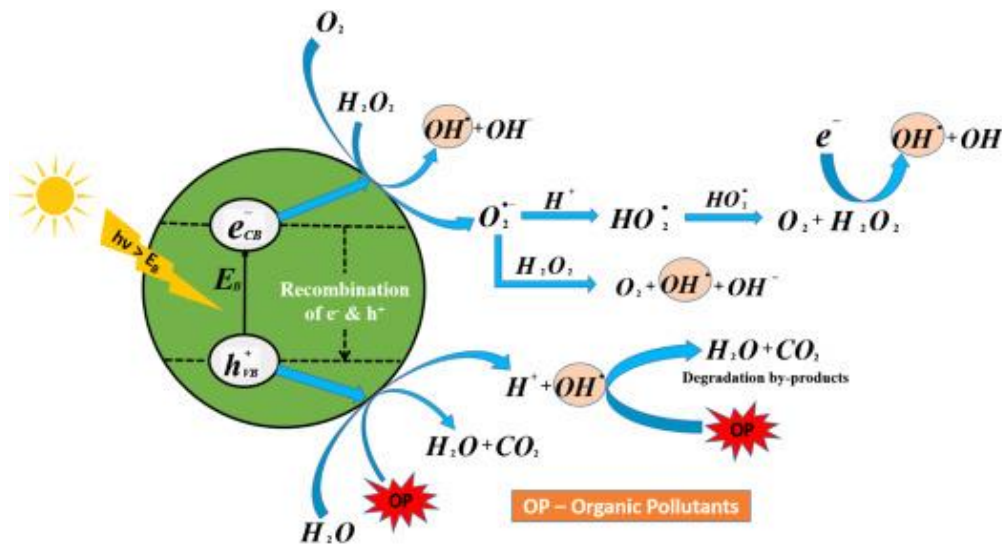
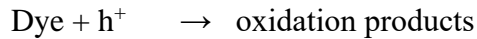
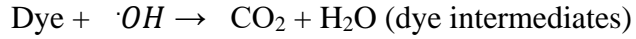


Figure 1. 1 Possible mechanism for photocatalytic degradation of dye

## 1.2. Climate change

Emissions of carbon dioxide (CO<sub>2</sub>) caused by human activity are generally considered the most important problem. The continued use of fossil fuels to meet the majority of the world's energy demand is threatened by increasing concentrations of CO<sub>2</sub> in the atmosphere and concerns over global warming. Global warming has been increasingly associated with the contribution of CO<sub>2</sub>. Currently, it is estimated that CO<sub>2</sub> contributes about 50% to the anthropogenic greenhouse effect. Usage of fossil energies must be substituted by clean and renewable energy which show relatively lower greenhouse emission. Recently, strenuous research efforts have been dedicated to generation of hydrogen energy. The carbon-free attribute renders its consideration as one of the greenest energy carriers, hence being benchmarked as a promising remedy for three critical problems

associated with anthropogenic use of fossil fuels, fuel exhaustion, air pollution, and climate changes[5].

In contradiction to the prime objectives of hydrogen energy existence, most of the existing hydrogen generating technologies are restricted to fossil fuels feedstock, contemporarily accounts for 95% of total hydrogen production. Apart from the remaining 5%, the laud of present fossil-based hydrogen generating technologies as ‘green technologies’ is highly questionable. Based on the recent life cycle analysis, fossil based H<sub>2</sub> generation lamentably comes with substantial releasing of CO<sub>2</sub> to adjoining environment. Whilst the remaining 5% of total hydrogen are predominantly derived from some other renewable resources, however, hampered from scaled-production due to uneconomical operational costs[1]. PEC water-splitting is considered a promising technology to source clean and renewable hydrogen energy, to fulfill the increasing international energy demands and to resolve current environmental concerns[6].

### **1.3. Basic of PEC water splitting**

Photoelectrochemical splitting of water is based on the conversion of photons incident on the surface of a semiconductor, having energy higher than the bandgap of semiconductor, into the electrochemical energy that can directly split water into molecular H<sub>2</sub> and O<sub>2</sub>[7]. The following processes, take place in a photoelectrochemical cell: a) absorption of light b) charge generation c) charge separation d) charge transportation, and e) chemical reactions at the electrode surfaces[2]. Electrons get excited to the conduction-band upon illumination, leaving behind positively charged holes in the valence-band. A portion of these photogenerated charge-carriers migrates to the semiconductor/ electrolyte interface due to the built-in electric field in the depletion region to carry out the desired chemical reactions. The built-in electric field in the depletion-region is formed due to the potential difference between the Fermi-level of semiconductor and the redox-potential of

water. For a PEC system with a photoanode, the photo-generated electrons migrate to the back contact through the external circuit towards the counter-electrode and reduce water to generate hydrogen; the corresponding reaction being known as hydrogen-evolution reaction (HER). On the other hand, holes in the valence-band of semiconductor reach the surface of the semiconductor to oxidize water to form molecular oxygen, thereby driving the oxygen-evolution reaction (OER).



The rest of the separated charge-carriers undergo recombination in bulk and release their energy thermally in the form of phonons, which ultimately hampers the overall activity of the photoelectrode[8].

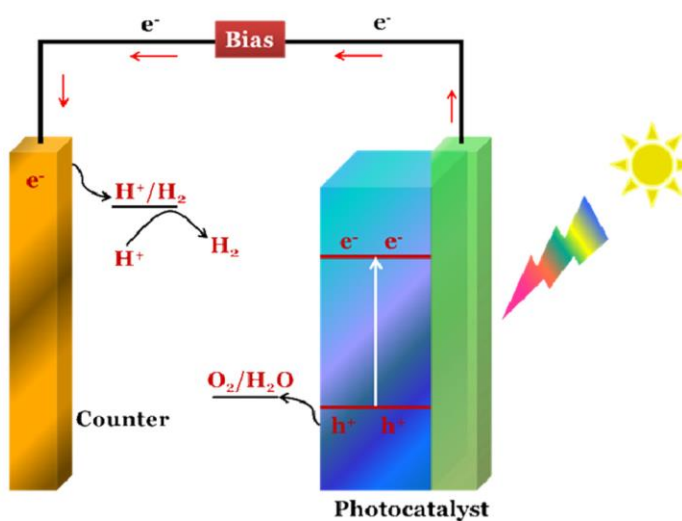


Figure 1. 2 The mechanism and principle of Photoelectrochemical cell[9]

## 1.4. Sodium titanate

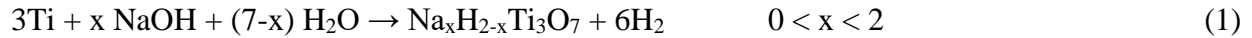
One-dimensional (1D) semiconducting nanostructures, such as nanotubes, nanorods and nanowires have been the focus of considerable attention because of their unique structural and

electronic properties. So far, they have been widely used in a variety of fields, such as photodetectors, solar cells, hydrogen production, lithium batteries, gas sensing, and photocatalysis. Especially, one-dimensional titanate nanotubes (TNTs) as photocatalyst have been remaining a subject of many investigations, such as degradation of pollutants, hydrogen production, and selective organic transformation, due to their following promising features from a viewpoint of photocatalysis. First, the 1D geometry facilitates fast and long-distance electron transport. Second, the 1D nanotubular structure is expected to have a large specific surface area and pore volume. Third, layered titanate family and  $\text{TiO}_2$  have similar structure features with  $\text{TiO}_6$  octahedra arranged in a zigzag configuration and can be topotactically transformed into  $\text{TiO}_2$  phase while maintaining their original morphology[10].

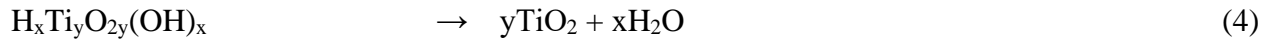
The elaboration of 1D  $\text{TiO}_2$  related materials with different morphologies and high purity may occur using three general approaches: (i) the chemical “template” method, (ii) the electrochemical “anodic oxidation” method, and (iii) the alkaline hydrothermal treatment. For large scale production of nanostructured  $\text{TiO}_2$  materials, the hydrothermal method, proposed by Kasuga et al., is the most suitable. There have been two hydrothermal treatment approaches frequently reported for the synthesis of layered titanates. The first approach involves the treatment of  $\text{TiO}_2$  in alkaline solution with high concentration (e.g., as high as 10 M NaOH or KOH). After the pioneering work on  $\text{TiO}_2$ -based nanotubes, this approach has become popular for the preparation of one-dimensional layered titanate as well as  $\text{TiO}_2$  nanostructures in forms such as nanotubes and nanorods. The second approach involves the hydrothermal treatment of Ti metal in forms of foil, mesh, and powders, in alkaline solution with relatively low concentration (e.g., low than 1 M NaOH). By this approach, highly oriented  $\text{TiO}_2$  nanoarrays could be obtained on supporting substrates in contrast to randomly dispersed nanostructures by the first one. Interestingly, not only

one-dimensional nanotubes or nanorods but also two-dimensional nanosheet arrays can grow on the Ti substrate by the second approach. Several factors can influence the formation of titania nanostructures such as: the structure of the starting material (Ti foil or TiO<sub>2</sub> thin layer), the nature and concentration of the alkaline solution, the hydrothermal temperature and duration and the post-treatment processes (acid washing and calcination)[11].

The formation of sodium titanate can be described by



Protonated titanate can be obtained by extracting the interlayered Na<sup>+</sup> ions in sodium titanate with diluted hydrochloric acid or other inorganic acid aqueous solution. TiO<sub>2</sub> can be obtained by the calcination of protonated titanate. The overall reactions can be explained as follows:



where the first step (2) represents the protonated process. The second step (3) is the desorption of absorbed water by calcining the protonated titanate at temperature T1, and the third step (4) corresponds to the decomposition of the titanate into titania at a higher temperature T2 (T2 > T1)[12].

Sodium titanate has a proper band edge position for both hydrogen reduction and water oxidation processes, which make it proper candidate for photoelectrochemical water splitting applications. However, due to its intrinsic wide bandgap of sodium titanates, which is around 3.4 eV, they can be photocatalitically active under UV light irradiation.

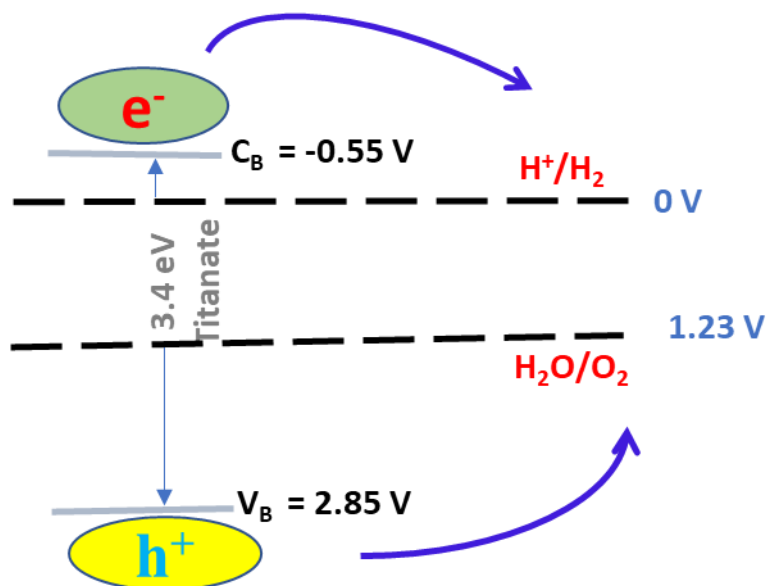


Figure 1. 3 Band gap and band-edge energy level of sodium titanate and water splitting ability.

## 1.5. Improving of the photoelectrochemical and photocatalytic activity of sodium titanate

### 1.5.1. Acidic treatment with the assistance of ultrasonic waves

Among the various metal oxides as semiconductors that have previously been applied as photocatalysts, sodium titanate have been widely used as photocatalysts because of their high chemical inertness, low cost, abundance, lack of toxicity, and thermal stability[13-18] However, the main drawback of this type of photocatalyst is its inefficient usage of solar light due to its wide bandgap; this provides motivation for the development of its band gap into the visible light region that has a much larger fraction of the sunlight spectrum than UV, which will enhance its solar light utilization and photocatalytic efficiency [19-22].

The photodegradation activity of dye pollutant depends on the specific surface areas and crystallinity of the photocatalyst used. The photocatalytic reaction occurs on the surface of the catalyst. Thus, catalysts consisting of ultrafine powders with a particle size at a scale of tens of nanometers should show higher photocatalytic activity due to the large specific surface. However, ultrafine powders also have a tendency for agglomeration to make larger particles, resulting in an adverse effect on photocatalytic activity[23].

The two main drawbacks of titanate, i.e., the poor crystallinity and tendency of agglomeration of TiO<sub>2</sub> nanoparticles, would be simultaneously improved by the formation of a composite structure that possesses both the surface properties of TiO<sub>2</sub> nanocrystals and most of the morphologies of titanate nanotubes. Titanate nanotubes provide a good platform for delicate phase and morphological tailoring via acidic post treatment with the assistance of ultrasonic waves to obtain a hydrogen titanate and titania mixed phase nanostructure. It is anticipated that controlling the concentration and the sonication time will play a key role in the transformation of titanate into titania and the replacement of Na<sup>+</sup> with H<sup>+</sup>.

### **1.5.2. Loading of noble metal**

Nano-structured layered titanate has a large surface area, which provides the possibility of achieving uniform and high loading of the active noble metal in highly dispersed form on the surface[24, 25].

Noble metal nanoparticles have been extensively applied as surface modifiers for TiO<sub>2</sub>-based photocatalysts. They reduce charge recombination by acting as “electron sinks” and thereby increasing efficient photo-reduction[26, 27]. Metal nanoparticles also show the surface plasmon resonance (SPR) effect, which consists of being optically excited under the visible region, and they are also being intensively investigated as potential visible sensitizers[28, 29]. Several works by



other researchers have demonstrated the effect of silver loading on photocatalytic activity of TiO<sub>2</sub>[30-35]. While no systematic study has yet optimized the loading percentage of Ag on TiO<sub>2</sub>-based nanocomposite.

### **1.5.3. Heterojunction with visible semiconductor**

Their high-rate recombination of photoinduced electrons and holes cause to low quantum efficiency of photocatalytic reactions. Even though there have been some reports that showed photoelectrochemical properties of sodium titanate in powder form, some issues for practical applications of NTO, such as aggregation, scattering and separation of powder from substrate should be resolved [36, 37]. Growing sodium titanate directly on the surface of Ti foil substrate can improve noticeably these problems. Furthermore, direct contacts of sodium titanate nanostructures with metal substrate can facilitate transfer of photogenerated charge carriers from active nanoparticle to the substrate [38]. Thus, the introduction of smart ideas to decrease the resistance of charge transfer can contribute to greatly improving the PEC performance of the NTO photoelectrodes.

Light absorption limitation of sodium titanate nanostructures because of their wide band gap energy under solar light irradiation can be solved by depositing narrow band gap materials onto the NTO nanostructures. CdS is a supreme narrow band gap semiconductor that can sensitize sodium titanate to improve its photoresponse to the visible light region [39-41]. In addition, suitable band alignment between sodium titanate and CdS can modulate the separation and transfer of photogenerated charge carriers to consequently increase their photoelectrochemical properties.

### **1.5.4. Optimization of NaOH concentration**

The nucleation of Na<sub>2</sub>Ti<sub>3</sub>O<sub>7</sub> most likely occurred at the defect sites on the thin layer of TiO<sub>2</sub> during the hydrothermal reaction and can lead to a significant reduction in the number of defect sites.

Optimizing NaOH concentration in the second approach to sodium titanate preparation leads to the formation of a new  $\text{TiO}_2/\text{Na}_2\text{Ti}_3\text{O}_7$  photoanode that has both titania photocatalytic activity and a large surface area of sodium titanate with nanoflower morphology. Furthermore, a suitable alignment of the band edge between  $\text{TiO}_2$  and  $\text{Na}_2\text{Ti}_3\text{O}_7$  and their direct contacts with the Ti foil significantly facilitate the separation and transfer of photogenerated electrons from the active phases to the substrate.

## References

- [1] A. Rafiq, M. Ikram, S. Ali, F. Niaz, M. Khan, Q. Khan, M.J.J.o.I. Maqbool, E. Chemistry, Photocatalytic degradation of dyes using semiconductor photocatalysts to clean industrial water pollution, (2021).
- [2] M.R. Hoffmann, S.T. Martin, W. Choi, D.W.J.C.r. Bahnemann, Environmental applications of semiconductor photocatalysis, 95 (1995) 69-96.
- [3] J. Saien, A.R.J.J.o.I. Soleymani, E. Chemistry, Feasibility of using a slurry falling film photo-reactor for individual and hybridized AOPs, 18 (2012) 1683-1688.
- [4] A. Ajmal, I. Majeed, R.N. Malik, H. Idriss, M.A.J.R.A. Nadeem, Principles and mechanisms of photocatalytic dye degradation on TiO<sub>2</sub> based photocatalysts: a comparative overview, 4 (2014) 37003-37026.
- [5] T. Ishaq, M. Yousaf, I.A. Bhatti, A. Batool, M.A. Asghar, M. Mohsin, M.J.I.J.o.H.E. Ahmad, A perspective on possible amendments in semiconductors for enhanced photocatalytic hydrogen generation by water splitting, (2021).
- [6] M. Ali, E. Pervaiz, U. Sikandar, Y.J.I.J.o.H.E. Khan, A review on the recent developments in zirconium and carbon-based catalysts for photoelectrochemical water-splitting, (2021).
- [7] A. Mills, S.J.J.o.p. Le Hunte, p.A. Chemistry, An overview of semiconductor photocatalysis, 108 (1997) 1-35.
- [8] I. Hamdani, A.J.R. Bhaskarwar, S.E. Reviews, Recent progress in material selection and device designs for photoelectrochemical water-splitting, (2020) 110503.
- [9] S. Chandrasekaran, J.S. Chung, E.J. Kim, S.H.J.J.o.E.S. Hur, Technology, Advanced nano-structured materials for photocatalytic water splitting, 7 (2016) 1-12.
- [10] Z.-R. Tang, X. Yin, Y. Zhang, Y.-J.J.I.c. Xu, Synthesis of titanate nanotube–CdS nanocomposites with enhanced visible light photocatalytic activity, 52 (2013) 11758-11766.
- [11] C. Wang, X. Zhang, Y. Zhang, Y. Jia, J. Yang, P. Sun, Y.J.T.J.o.P.C.C. Liu, Hydrothermal growth of layered titanate nanosheet arrays on titanium foil and their topotactic transformation to heterostructured TiO<sub>2</sub> photocatalysts, 115 (2011) 22276-22285.
- [12] J. Huang, Y. Cao, M. Wang, C. Huang, Z. Deng, H. Tong, Z.J.T.J.o.P.C.C. Liu, Tailoring of low-dimensional titanate nanostructures, 114 (2010) 14748-14754.
- [13] S.-W. Lai, J.-W. Park, S.-H. Yoo, J.-M. Ha, E.-H. Song, S.-O.J.i.j.o.h.e. Cho, Surface synergism of Pd/H<sub>2</sub>Ti<sub>3</sub>O<sub>7</sub> composite nanowires for catalytic and photocatalytic hydrogen production from ammonia borane, 41 (2016) 3428-3435.
- [14] P. Sokhandani, A.A. Babaluo, M. Rezaei, M. Shahrezaei, A. Hasanzadeh, S.G. Mehmandoust, R. Mehdizadeh, Nanocomposites of PVC/TiO<sub>2</sub> nanorods: Surface tension and mechanical properties before and after UV exposure, Journal of Applied Polymer Science, 129 (2013) 3265-3272.
- [15] M. Shahrezaei, S. Habibzadeh, A.A. Babaluo, H. Hosseinkhani, M. Haghghi, A. Hasanzadeh, R. Tahmasebpour, Study of synthesis parameters and photocatalytic activity of TiO<sub>2</sub> nanostructures, Journal of Experimental Nanoscience, 12 (2017) 45-61.
- [16] R. Tahmasebpour, A.A. Babaluo, J.R. Shahrouzi, M. Tahmasebpour, M. Shahrezaei, Theoretical and experimental studies on the anodic oxidation process for synthesis of self-ordering TiO<sub>2</sub> nanotubes: Effect of TiO<sub>2</sub> nanotube lengths on photocatalytic activity, Journal of environmental chemical engineering, 5 (2017) 1227-1237.
- [17] M. Shahrezaei, A.A. Babaluo, S. Habibzadeh, M. Haghghi, Photocatalytic Properties of 1D TiO<sub>2</sub> Nanostructures Prepared from Polyacrylamide Gel–TiO<sub>2</sub> Nanopowders by Hydrothermal Synthesis, European Journal of Inorganic Chemistry, 2017 (2017) 694-703.

- [18] X. Hu, Z. Sun, J. Song, G. Zhang, C. Li, S.J.J.o.c. Zheng, i. science, Synthesis of novel ternary heterogeneous BiOCl/TiO<sub>2</sub>/sepiolite composite with enhanced visible-light-induced photocatalytic activity towards tetracycline, 533 (2019) 238-250.
- [19] D. Gong, W.C.J. Ho, Y. Tang, Q. Tay, Y. Lai, J.G. Highfield, Z.J.J.o.S.S.C. Chen, Silver decorated titanate/titania nanostructures for efficient solar driven photocatalysis, 189 (2012) 117-122.
- [20] S. Wu, H. Hu, Y. Lin, J. Zhang, Y.H.J.C.E.J. Hu, Visible light photocatalytic degradation of tetracycline over TiO<sub>2</sub>, 382 (2020) 122842.
- [21] V.M. Daskalaki, M. Antoniadou, G. Li Puma, D.I. Kondarides, P.J.E.s. Lianos, technology, Solar light-responsive Pt/CdS/TiO<sub>2</sub> photocatalysts for hydrogen production and simultaneous degradation of inorganic or organic sacrificial agents in wastewater, 44 (2010) 7200-7205.
- [22] V. Etacheri, C. Di Valentin, J. Schneider, D. Bahnemann, S.C.J.J.o.P. Pillai, P.C.P. Reviews, Visible-light activation of TiO<sub>2</sub> photocatalysts: Advances in theory and experiments, 25 (2015) 1-29.
- [23] H. Zhu, X. Gao, Y. Lan, D. Song, Y. Xi, J.J.J.o.t.A.C.S. Zhao, Hydrogen titanate nanofibers covered with anatase nanocrystals: a delicate structure achieved by the wet chemistry reaction of the titanate nanofibers, 126 (2004) 8380-8381.
- [24] X. Sun, Y.J.C.A.E.J. Li, Synthesis and characterization of ion-exchangeable titanate nanotubes, 9 (2003) 2229-2238.
- [25] D.V. Bavykin, J.M. Friedrich, F.C.J.A.m. Walsh, Protonated titanates and TiO<sub>2</sub> nanostructured materials: synthesis, properties, and applications, 18 (2006) 2807-2824.
- [26] A. Scalfani, M.-N. Mozzanega, P.J.J.o.P. Pichat, P.A. Chemistry, Effect of silver deposits on the photocatalytic activity of titanium dioxide samples for the dehydrogenation or oxidation of 2-propanol, 59 (1991) 181-189.
- [27] B. Neppolian, A. Bruno, C.L. Bianchi, M.J.U.s. Ashokkumar, Graphene oxide based Pt–TiO<sub>2</sub> photocatalyst: ultrasound assisted synthesis, characterization and catalytic efficiency, 19 (2012) 9-15.
- [28] X. Chen, H.Y. Zhu, J.C. Zhao, Z.F. Zheng, X.P.J.A.C.I.E. Gao, Visible-light-driven oxidation of organic contaminants in air with gold nanoparticle catalysts on oxide supports, 47 (2008) 5353-5356.
- [29] B. Neppolian, H. Jung, H.J.J.o.A.O.T. Choi, Photocatalytic degradation of 4-chlorophenol using TiO<sub>2</sub> and Pt-TiO<sub>2</sub> nanoparticles prepared by sol-gel method, 10 (2007) 369-374.
- [30] O. Nasr, O. Mohamed, A.-S. Al-Shirbini, A.-M.J.J.o.P. Abdel-Wahab, P.A. Chemistry, Photocatalytic degradation of acetaminophen over Ag, Au and Pt loaded TiO<sub>2</sub> using solar light, 374 (2019) 185-193.
- [31] Y. Sun, Y. Gao, J. Zeng, J. Guo, H.J.M.L. Wang, Enhancing visible-light photocatalytic activity of Ag-TiO<sub>2</sub> nanowire composites by one-step hydrothermal process, 279 (2020) 128506.
- [32] L. Lu, G. Wang, Z. Xiong, Z. Hu, Y. Liao, J. Wang, J.J.C.I. Li, Enhanced photocatalytic activity under visible light by the synergistic effects of plasmonics and Ti<sup>3+</sup>-doping at the Ag/TiO<sub>2</sub>-x heterojunction, (2020).
- [33] Y. Zhang, T. Wang, M. Zhou, Y. Wang, Z.J.C.I. Zhang, Hydrothermal preparation of Ag-TiO<sub>2</sub> nanostructures with exposed {001}/{101} facets for enhancing visible light photocatalytic activity, 43 (2017) 3118-3126.
- [34] C. Díaz-Urbe, J. Vilorio, L. Cervantes, W. Vallejo, K. Navarro, E. Romero, C.J.I.J.o.P. Quiñones, Photocatalytic activity of Ag-TiO<sub>2</sub> composites deposited by photoreduction under UV irradiation, 2018 (2018).

- [35] R. Zhou, S. Lin, H. Zong, T. Huang, F. Li, J. Pan, J.J.J.o.N. Cui, Continuous synthesis of Ag/TiO<sub>2</sub> nanoparticles with enhanced photocatalytic activity by pulsed laser ablation, 2017 (2017).
- [36] A. Abdal-hay, K. Gulati, T. Fernandez-Medina, M. Qian, S.J.A.S.S. Ivanovski, In situ hydrothermal transformation of titanium surface into lithium-doped continuous nanowire network towards augmented bioactivity, 505 (2020) 144604.
- [37] M. Kolaei, M. Tayebi, B.-K.J.A.S.S. Lee, The synergistic effects of acid treatment and silver (Ag) loading for substantial improvement of photoelectrochemical and photocatalytic activity of Na<sub>2</sub>Ti<sub>3</sub>O<sub>7</sub>/TiO<sub>2</sub> nanocomposite, 540 (2021) 148359.
- [38] Y. Tang, L. Hong, Q. Wu, J. Li, G. Hou, H. Cao, L. Wu, G.J.E.A. Zheng, TiO<sub>2</sub> (B) nanowire arrays on Ti foil substrate as three-dimensional anode for lithium-ion batteries, 195 (2016) 27-33.
- [39] R. Wang, L. Wang, Y. Zhou, Z.J.A.C.B.E. Zou, Al-ZnO/CdS photoanode modified with a triple functions conformal TiO<sub>2</sub> film for enhanced photoelectrochemical efficiency and stability, 255 (2019) 117738.
- [40] P. Pathak, S. Gupta, K. Grosulak, H. Imahori, V.J.T.J.o.P.C.C. Subramanian, Nature-inspired tree-like TiO<sub>2</sub> architecture: a 3D platform for the assembly of CdS and reduced graphene oxide for photoelectrochemical processes, 119 (2015) 7543-7553.
- [41] H.S. Han, W. Park, A. Sivanantham, S.W. Hwang, S. Surendran, U. Sim, I.S.J.C.I. Cho, Facile fabrication of nanotubular heterostructure for enhanced photoelectrochemical performance, 47 (2021) 3972-3977.

## **Chapter 2: Acid treatment and silver (Ag) loading, two different strategies for improvement of photoelectrochemical and photocatalytic activity sodium titanate**

### **Abstract**

This study investigated the effects of acid treatment and silver (Ag) loading on  $\text{Na}_2\text{Ti}_3\text{O}_7/\text{TiO}_2$  nanocomposite (NTO), synthesized through a hydrothermal method, to improve the photoelectrochemical (PEC) performance and photodegradation of Rhodamine B (RhB). Due to the high specific surface area of this nanocomposite ( $199.06 \text{ m}^2/\text{gr}$ ) and well dispersion of Ag nanoparticles on the surface of the catalyst, the best photocatalytic efficiency obtained by very small percentage of optimized silver loading. The morphology, chemical state, and optical property changes of the NTO by the acid treatments and Ag loading were obtained by XRD, Raman, UV-DRS, PL, XPS, SEM, and TEM analyses. Under visible light irradiation, 97.3 % of the RhB in the aqueous solution was photodegraded by the optimized NTO with 0.1M HCl treatment and 0.5wt% Ag loading (NTOH0.1/Ag0.5), which is much higher than that of pristine NTO. The PEC properties of the NTOH0.1/Ag0.5 photoanode were measured under  $100 \text{ mW}\cdot\text{cm}^{-2}$  illuminations in 0.5 M aqueous solution of  $\text{Na}_2\text{SO}_3$  as the electrolyte, and it showed 2.7 times higher photocurrent density than that of the untreated NTO. Combined analyses of Mott-Schottky plots and electrochemical impedance spectroscopy (EIS) of the NTOH0.1/Ag0.5 nanocomposite confirmed that the acid treatment and silver (Ag) loading increased its donor concentration ( $N_D$ ) and charge carrier transfer efficiency, resulting in substantially improved PEC performance.

**Keywords:**  $\text{Na}_2\text{Ti}_3\text{O}_7/\text{TiO}_2$  nanocomposite, acid treatments, silver (Ag) loading, recombination, plasmonic effect.

## 2.1. Introduction

A primary aim of environmental remediation is eliminating dyes and other commercial colorants from wastewater effluents of dye processing units. The color of wastewater including dyes can prevent photosynthesis by aquatic plants and deteriorate water quality. In addition, the carcinogenic and toxic properties of dyes are harmful to human beings and aquatic life[1-5]. The textile, leather, paper, and paint industries are the principal sources of this kind of dye pollutants. Rhodamine B (RhB) is one of the most used dyes in the wastewaters of these industries, which are sometimes discharged directly to rivers and lakes[6].

Several treatment processes have been applied for the removal of dyes in water, and these can be categorized into two major groups: chemical and physical procedures. Physical procedures are typically nondestructive and produce sludge or solid waste, thus necessitating further treatment that can be costly. Chemical methods using powerful oxidants such as chlorine or ozone are more effective, but they are not economically practical due to the high dosages of expensive chemicals needed[7, 8].

Photocatalytic oxidation is an advanced oxidation process that has attracted attention by virtue of being an efficient, low-cost, and environmentally-friendly process by which organics can be completely mineralized into CO<sub>2</sub> and H<sub>2</sub>O during the photocatalytic process[9-11].

Solar energy is the major energy source on Earth. Prior efforts have converted solar energy to electrical energy using technology such as solar panels. In another method, direct sunlight has been applied to split water molecules into O<sub>2</sub> and H<sub>2</sub>. Water splitting can be accomplished through photoelectrochemical (PEC) reactions, which apply a semiconductor as the photoactive material. With fuel cell systems, hydrogen can be used to generate electricity without producing any pollution[12-17]. Among the various metal oxides as semiconductors that have previously been

applied as photocatalysts, TiO<sub>2</sub>-based materials have been widely used as photocatalysts because of their high chemical inertness, low cost, abundance, lack of toxicity, and thermal stability [18-23]. However, the main drawback of this type of photocatalyst is its inefficient usage of solar light due to its wide bandgap; this provides motivation for the development of its band gap into the visible light region that has a much larger fraction of the sunlight spectrum than UV, which will enhance its solar light utilization and photocatalytic efficiency [24-27].

The photodegradation activity of RhB depends on the specific surface areas and crystallinity of the photocatalyst used. The photocatalytic reaction occurs on the surface of the catalyst. Thus, catalysts consisting of ultrafine powders with a particle size at a scale of tens of nanometers should show higher photocatalytic activity due to the large specific surface. However, ultrafine powders also have a tendency for agglomeration to make larger particles, resulting in an adverse effect on photocatalytic activity [28]. It has been reported that alkali titanate (A<sub>2</sub>Ti<sub>n</sub>O<sub>2n+1</sub>, A= Li, Na and K) can be an active photocatalyst under UV irradiation because of their poor crystallinity and wide band gap (3.4 eV) [29, 30].

The two main drawbacks of titanate, i.e., the poor crystallinity and tendency of agglomeration of TiO<sub>2</sub> nanoparticles, would be simultaneously improved by the formation of a composite structure that possesses both the surface properties of TiO<sub>2</sub> nanocrystals and most of the morphologies of titanate nanotubes. Titanate nanotubes provide a good platform for delicate phase and morphological tailoring via acidic post treatment with the assistance of ultrasonic waves to obtain a hydrogen titanate and titania mixed phase nanostructure. It is anticipated that controlling the concentration and the sonication time will play a key role in the transformation of titanate into titania and the replacement of Na<sup>+</sup> with H<sup>+</sup>. Furthermore, nano-structured layered titanate has a



large surface area, which provides the possibility of achieving uniform and high loading of the active noble metal in highly dispersed form on the surface[31, 32].

Noble metal nanoparticles have been extensively applied as surface modifiers for TiO<sub>2</sub>-based photocatalysts. They reduce charge recombination by acting as “electron sinks” and thereby increasing efficient photo-reduction[33, 34]. Metal nanoparticles also show the surface plasmon resonance (SPR) effect, which consists of being optically excited under the visible region, and they are also being intensively investigated as potential visible sensitizers[35, 36]. Several works by other researchers have demonstrated the effect of silver loading on photocatalytic activity of TiO<sub>2</sub>[37-42]. While no systematic study has yet optimized the loading percentage of Ag on TiO<sub>2</sub>-based nanocomposite. Due to higher specific surface area of the Na<sub>2</sub>Ti<sub>3</sub>O<sub>7</sub>/TiO<sub>2</sub> nanocomposite which cause the great dispersion of Ag nanoparticles on the surface of the catalyst, the best efficiency can obtain by lower percentage of silver loading.

In the present study, we reported a simple method for preparing delicate hydrogen titanate-titania nanocomposites (NTOH) loaded with different amounts of silver cocatalyst (0.3-2 wt%), which showed remarkable activity under visible light irradiation. The preparation of the materials consisted of three stages: hydrothermal modification of TiO<sub>2</sub> powder, acid treatment with the assistance of ultrasonic waves, and impregnation deposition of Ag. The effects of the sonication in post acid treatments with different concentrations of aqueous HCl solutions and different amounts of silver loading were investigated in terms of the photocatalytic degradation of RhB and photoelectrochemical (PEC) properties.

## **2.2. Experimental procedure**

### **2.2.1. Catalyst preparation**

#### **2.2.1.1. Na<sub>2</sub>Ti<sub>3</sub>O<sub>7</sub>/TiO<sub>2</sub> nanocomposite (NTO) preparation**

Na<sub>2</sub>Ti<sub>3</sub>O<sub>7</sub>/TiO<sub>2</sub> nanocomposites (NTO) were synthesized through an alkali hydrothermal treatment process using commercial titanium dioxide as a starting material. Briefly, 2.0 g of TiO<sub>2</sub> (30% rutile and 70% anatase) was mixed in 160 mL of 10 M NaOH aqueous solution, then subjected to hydrothermal treatment in a Teflon-lined autoclave at 130 °C for 20 h. The white products were collected and sufficiently washed with deionized water and ethanol to remove the excess of non-reacted sodium hydroxide before being dried at 100 °C for 10 h.

#### **2.2.1.2. Replacement of Na<sup>+</sup> by H<sup>+</sup>**

First, 0.5 g of as-prepared NTO was added into 100 ml of each of the 0.01, 0.05, and 0.1M HCl aqueous solutions. Next, the mixture was sonicated for 5 h at 50 °C. Depending on their HCl concentrations, the prepared samples were simply named NTOH0.01, NTOH0.05, and NTOH0.1, respectively. In another sample, 0.5 g of NTO was mixed with 100 ml of 0.1M HCl and stirred for 5 h (NTOH0.1-stirring).

#### **2.2.1.3. Silver loading**

Ag cocatalyst was loaded on the photocatalyst using an impregnation method. Here, 1 g of NTOH0.1 was suspended in 100 mL of deionized water with the desired amount of AgNO<sub>3</sub>, then evaporated at 353 K to remove water and dried for 24 h at 373 K. The Ag-loaded NTOH0.1 samples are denoted by NTOH0.1/Ag0.3, NTOH0.1/Ag0.5, NTOH0.1/Ag1, and NTOH0.1/Ag2 according to the loading amounts of Ag, which are 0.3, 0.5, 1, and 2 wt%, respectively.

#### **2.2.1.4. Preparation of NTO, NTOH0.1, and NTOH0.1/Ag0.5 photoanodes**

To prepare the working electrodes, fluorine tin oxide (FTO) glass was cleaned under sonication in a mixture of ethanol, acetone, and distilled water (1:1:1) to remove all organic residues on the FTO surface. Next, 10 mg of each of the as-prepared samples was dispersed in 900  $\mu\text{L}$  of ethanol with 100  $\mu\text{L}$  of nafion. The mixture was sonicated to obtain a uniform gel suspension. Finally, 100  $\mu\text{L}$  of suspension was dropped onto the surface of FTO glass substrates and then dried in an oven at 70  $^{\circ}\text{C}$  for 2 h.

#### **2.2.2. Photocatalytic degradation**

The photocatalytic activities of the as-prepared samples were tested by decolorization and mineralization of an aqueous solution of Rhodamine B (RhB). In a typical run, 25 mg of photocatalyst was immersed in 50 mL of RhB solution (5 ppm) under exposure of three fluorescent lamps (55 W) with an emission peak at 550 nm under continuous magnetic stirring. To ensure adsorption-desorption equilibrium, the suspension was magnetically stirred for 1 h in the dark, then placed under visible light radiation for 2 h. During the light irradiation, 4 mL of the reaction mixture was sampled at each designated time interval, and then the liquid phase was easily separated by centrifugation. The removal efficiency of RhB was determined based on the absorption peak at 554 nm, as determined by a UV-Vis spectrophotometer.

#### **2.2.3. Photoelectrochemical (PEC) measurement**

PEC measurements were performed with a standard three-electrode cell consisting of a working electrode, Pt wire as a counter electrode, and Ag/AgCl (saturated with KCl) as a reference electrode immersed in 0.5M (pH=12) aqueous solution of  $\text{Na}_2\text{SO}_3$  as an electrolyte.

The PEC performances of the NTO, NTOH0.1, and NTOH0.1/Ag0.5 photoanodes were investigated under irradiation with a 300W Xenon lamp at a light intensity of 100mW/cm<sup>2</sup> from the front sides of the photoanodes in a voltage range from -0.7 to 0.7 V (vs. Ag/AgCl).

## 2.3. Results and discussion

### 2.3.1. Characterization of the synthesized photocatalysts

#### 2.3.1.1. XRD

Fig.1a shows the X-ray diffraction patterns of NTO, NTOH0.01, NTOH0.05, NTOH0.1, and NTOH0.1/Ag0.5. After the hydrothermal process, Na<sub>2</sub>Ti<sub>3</sub>O<sub>7</sub> became the dominant component of the synthesized NTO nanocomposites. The diffraction pattern of Na<sub>2</sub>Ti<sub>3</sub>O<sub>7</sub> showed four main characteristic peaks at  $2\theta = 10.1, 24.3, 28.4,$  and  $48.2^\circ$  which are typical of the monoclinic layered structure of Na<sub>2</sub>Ti<sub>3</sub>O<sub>7</sub> corresponding to the (0 0 1), (2 0 1), (1 1 1), and (0 2 0) crystal planes, respectively. These wide diffraction peaks indicate the poorly crystalline nature of the prepared sodium titanate nanotubes, which can be attributed to neither rutile nor anatase[10].

The as-synthesized NTO shows a strong diffraction peak at  $27.42^\circ$ , indicating TiO<sub>2</sub> in the rutile phase, and two other peaks located at  $37.7$  and  $54^\circ$ , corresponding to TiO<sub>2</sub> in the anatase phase[43]. Comparing the NTO and NTOH samples (NTOH0.01, NTOH0.05, and NTOH0.1) shows that there was a significant weakening of the diffraction peaks for the NTOH samples at  $2\theta = 10.1$  and  $28.4^\circ$  with increasing HCl concentration. This has been ascribed to the replacement of sodium cations with protons, which leads to a decreased Na<sup>+</sup>:H<sup>+</sup> ratio[10, 44]. It should be noted that the NTOH0.1 sample still shows two broad peaks at  $2\theta = 25$  and  $48.2^\circ$ , reflecting the presence of Na<sub>2</sub>Ti<sub>3</sub>O<sub>7</sub>. In this sample, the broad reflection peak at  $2\theta = 24.3^\circ$  related to Na<sub>2</sub>Ti<sub>3</sub>O<sub>7</sub> showed a slight shift to higher  $2\theta$  values at  $25^\circ$ .

In the reaction of NTO with the highest concentration of HCl (NTOH0.1), it can be seen that the diffraction peaks related to anatase ( $2\theta = 37.7$  and  $54^\circ$ ) and rutile  $\text{TiO}_2$  ( $2\theta = 27.42^\circ$ ) becomes sharper, and a new peak appears at the  $2\theta$  value of  $41.5^\circ$ , which is related to rutile phase. These observations confirm the increase in crystallinity and the progressive phase-transition from titanate nanostructure to anatase and rutile  $\text{TiO}_2$  during the acid treatment of sodium titanate nanotubes. The XRD spectrum of NTOH0.1/Ag0.5 is identical to that of NTOH0.1, indicating that silver did not significantly affect the monoclinic layered structure of sodium titanate.

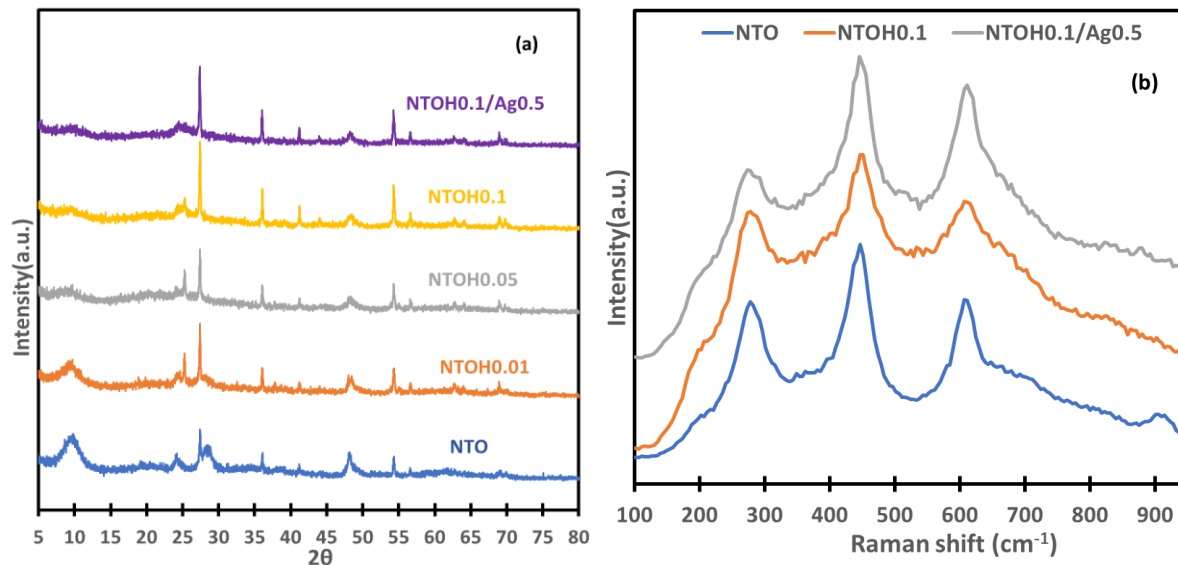


Figure 2. 1 (a) XRD patterns of NTO, NTOH0.01, NTOH0.05, NTOH0.1, and NTOH0.1/Ag0.5, (b) Raman spectra of NTO, NTOH0.1, and NTOH0.1/Ag0.5

### 2.3.1.2. Raman spectroscopy

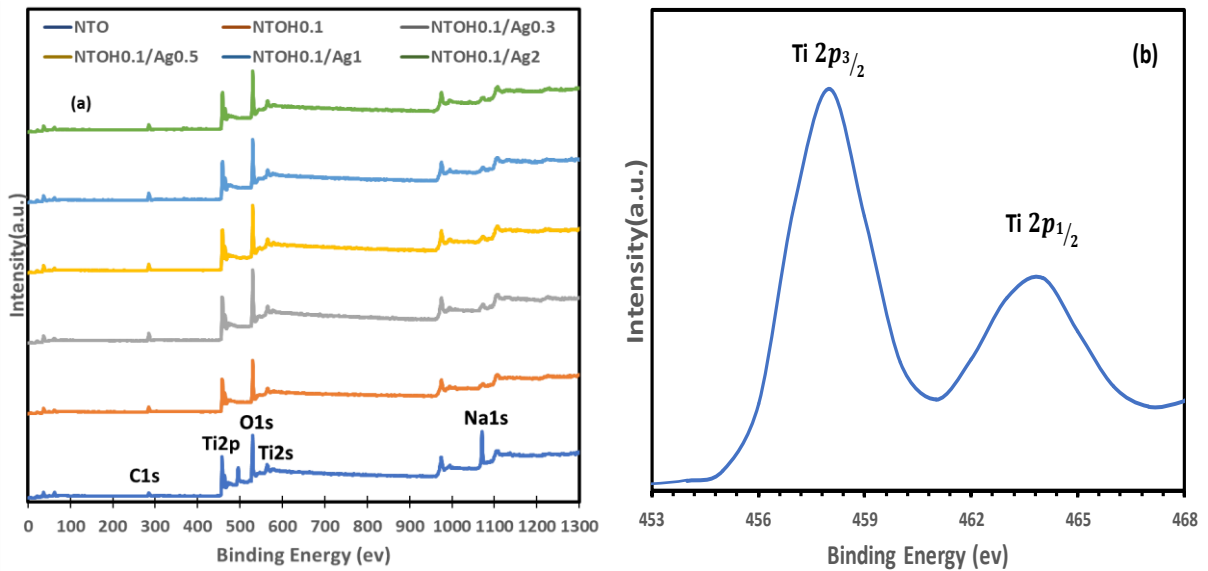
Raman spectrum analyses were conducted to identify the nature of the surface phases of NTO, NTOH0.1, and NTOH0.1/Ag0.5. The Raman scattering spectrum of NTO (Fig.1b) shows four typical peaks at 278, 447, 613, and  $908\text{ cm}^{-1}$ , as well as a shoulder peak at  $195\text{ cm}^{-1}$ . The peaks at 278, 447, and  $908\text{ cm}^{-1}$  were attributed to  $\text{Na}_2\text{Ti}_3\text{O}_7$ . The shoulder peak appearing at  $195\text{ cm}^{-1}$  and another peak at  $613\text{ cm}^{-1}$  are respectively assigned to the presences of anatase and rutile  $\text{TiO}_2$ , and

this is consistent with the XRD results[44]. Generally, the spectrum of sodium titanate after the elimination of sodium shares many common bands with the typical scattering pattern of sodium titanate, aside from the peak at  $908\text{ cm}^{-1}$ , which is attributed to Na-O-Ti bonds. The disappearance of this peak at NTOH0.1 is due to the removal of sodium from this sample. However, all the peaks assigned to Ti-O bonds are still observed in NTOH0.1[45]. This sample also shows a slight red shift from  $447$  to  $451\text{ cm}^{-1}$  after the removal of sodium. Moreover, the bands in the range from  $550$  to  $750\text{ cm}^{-1}$  showed a tendency to become broader in this sample relative to those of NTO. This tendency of becoming wider corresponds to the higher water content in the NTOH0.1 nanotubular titanate structure[44]. The Raman spectra of NTOH0.1/Ag0.5 show all the vibration frequencies of NTOH0.1.

### **2.3.1.3. XPS**

Different samples were characterized using an XPS technique to obtain an accurate and comprehensive understanding of their element composition in the surface layer. Fig.2a shows the XPS spectra survey of the NTO, NTOH0.1, and Ag-loaded NTOH0.1 samples. The XPS spectrum survey of NTO (Fig.2a) shows three peaks located at  $1070.9$ ,  $457.8$ , and  $529.4\text{ eV}$ , which are attributable to Na1s, Ti2p, and O1s, respectively[46]. This confirms the existence of Na, Ti, and O elements in NTO. The two binding energies positioned at  $458.1$  and  $463.9\text{ eV}$  (Fig.2b) indicate Ti $2p_{3/2}$  and Ti $2p_{1/2}$ , respectively[47]. The intrinsic peak at  $529.4\text{ eV}$  corresponds to the crystal lattice oxygen of the samples (Ti-O-Ti)[48]. Compared with the XPS spectra survey of NTO, the binding energy centered at  $1070.9$  that was indicated to Na1s disappeared for NTOH0.1. This proves that after acid treatment of NTO, Na<sup>+</sup> cations were replaced with H<sup>+</sup> in existing nanotubular Na<sub>2</sub>Ti<sub>3</sub>O<sub>7</sub> in NTO.

Moreover, the high-resolution XPS spectra of the NTOH0.1 samples loaded with different amounts of Ag show two peaks at 367.8 and 373.7 eV (Fig.2 (c)-(f)), which respectively correspond to Ag 3d<sub>5/2</sub> and Ag 3d<sub>3/2</sub>. Deconvolution of Ag XPS spectra show that Ag 3d<sub>5/2</sub> at 367.2 eV and Ag 3d<sub>3/2</sub> at 372.8.0 eV correspond to metallic Ag, while Ag 3d<sub>5/2</sub> at 368 eV and Ag 3d<sub>3/2</sub> at 374 eV belong to Ag<sup>+</sup> in Ag<sub>2</sub>O[49].



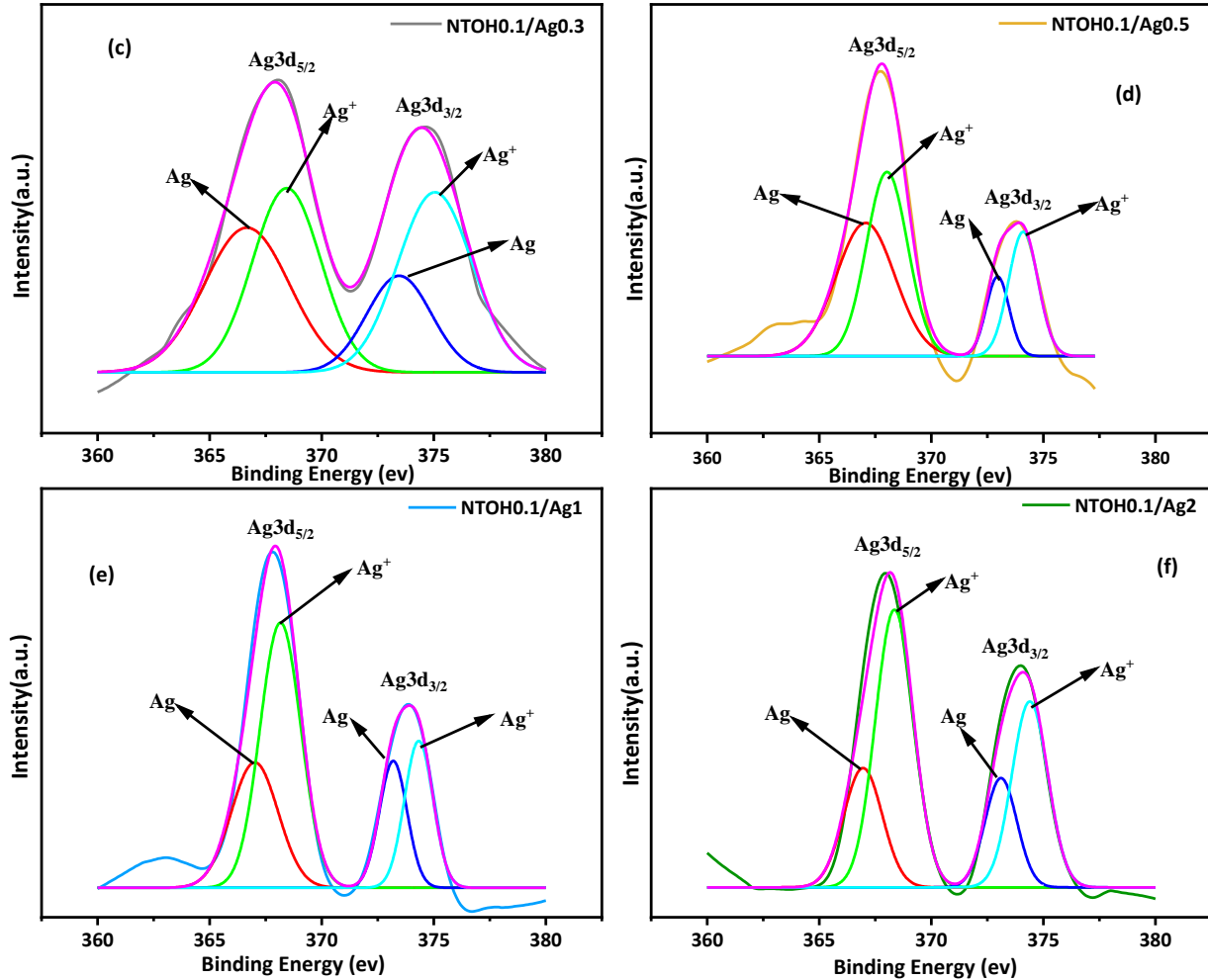


Figure 2. 2. (a) XPS survey spectra of samples and high-resolution XPS spectra of (b) Ti, (c) NTOH0.1/Ag0.3, (d) NTOH0.1/Ag0.5, (e) NTOH0.1/Ag1 and (f) NTOH0.1/Ag2

### 2.3.1.4. Optical absorption of samples by UV-Vis

The optical properties of as-prepared NTO, NTOH0.1, and Ag-loaded NTOH0.1 were assessed using a UV-Vis spectrophotometer. As shown in Fig.3a, NTO exhibits two different absorption edges that corresponded to different electron transitions in the NTO structure. The first absorption edge around 365 nm corresponded to the band gap energy of 3.4 eV for Na<sub>2</sub>Ti<sub>3</sub>O<sub>7</sub>, while the second one around 400 nm corresponded to the band gap energy of about 3.1 eV related to TiO<sub>2</sub>. This means that the spectra assigned to both sodium titanate and TiO<sub>2</sub> can clearly be seen in the absorption spectra of NTO. These results are consistent with the XRD results that showed



diffraction peaks for both  $\text{Na}_2\text{Ti}_3\text{O}_7$  and  $\text{TiO}_2$  in NTO. Moreover, there was no absorption of visible light for this sample. After  $\text{Na}^+$  was replaced with  $\text{H}^+$  during the acid treatment of NTO, the absorption edge related to  $\text{Na}_2\text{Ti}_3\text{O}_7$  in NTOH0.1 moved toward the absorption edge of  $\text{TiO}_2$ , confirming that the titanate nanotubes were partially converted to  $\text{TiO}_2$  during this process. The absorption of NTOH0.1 extended to a higher wavelength than that of NTO, also light absorption in the visible region was enhanced in this sample, which means it can potentially be used as a visible light driven photocatalyst. Compared with NTOH0.1, the NTOH0.1/Ag0.5 sample shows higher absorption in the visible light region, which is attributed to the surface plasmon resonance effect of silver NPs on NTOH0.1. The DR UV-vis spectra of the NTOH0.1/Ag samples loaded with silver (0.3 to 2 wt%) using an impregnation method are plotted in Fig.3b. Based on these results, NTOH0.1/Ag0.5 shows the highest visible light absorption, and its absorption edge shifted to a higher wavelength as well.

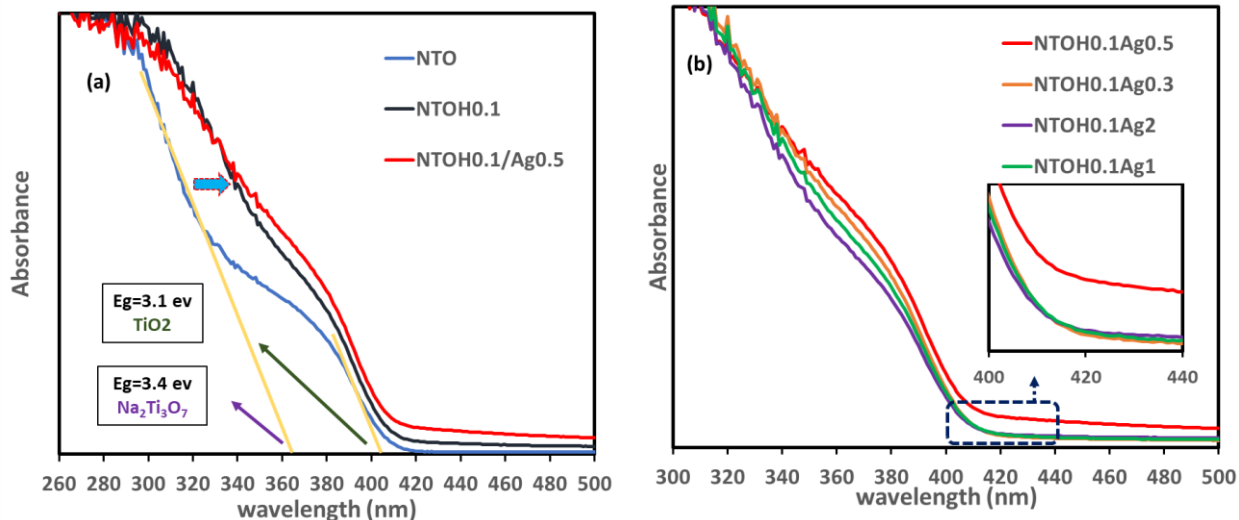
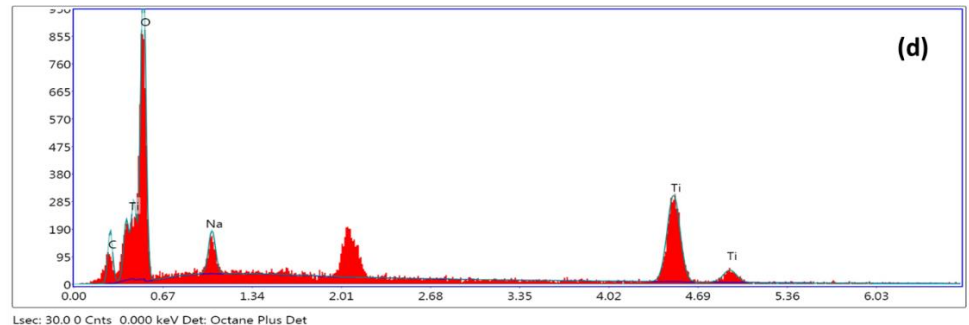
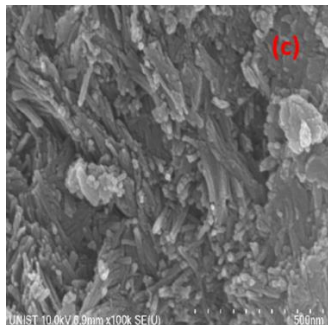
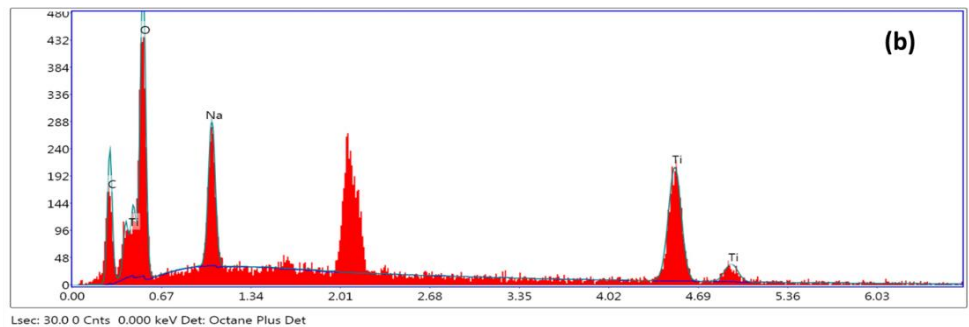
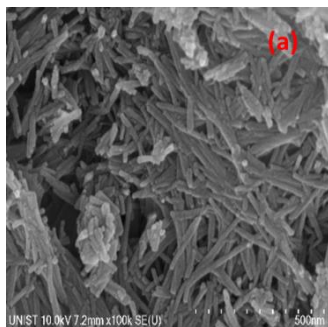


Figure 2. 3 UV-Vis diffuse reflectance spectra of (a) NTO, NTOH0.1, and NTOH0.1/Ag0.5 and (b) NTOH0.1/Ag with varying Ag loading (0.3, 0.5, 1, and 2 wt%)

### 2.3.1.5. SEM

The SEM images demonstrate the morphology change of NTO before and after the acid treatment with aqueous HCl solution. As shown in Fig.4a, the formed NTO samples are composed of sodium titanate with nanotubular morphology, along with a negligible proportion of TiO<sub>2</sub> nanoparticles formed over the outer surface of them. The specimen obtained by acid treatment with 0.05M HCl shows a phase transition from sodium titanate to TiO<sub>2</sub> nanoparticles, but nanotubes still comprise a noticeable proportion of this sample (Fig.4c). After the treatment with a higher concentration of HCl (NTOH0.1), a much larger fraction of titanate nanotubes is converted to TiO<sub>2</sub> nanoparticles, leading to the coexistence of connecting phases that comprise both the surface photocatalytic properties of TiO<sub>2</sub> and the high surface area of titanate nanotubes (Fig.4e).

The elemental compositions of NTO and NTOH0.05, obtained from the EDX spectrum (Fig.4b and d), demonstrated a decrease in Na<sup>+</sup> ion content from 10.49% to 4.31%, which is attributed to the replacement of Na<sup>+</sup> with H<sup>+</sup> during the acid treatment process. By increasing the concentration of HCl to 0.1M, the Na<sup>+</sup> content will decrease to nearly zero percent (Fig.4f).



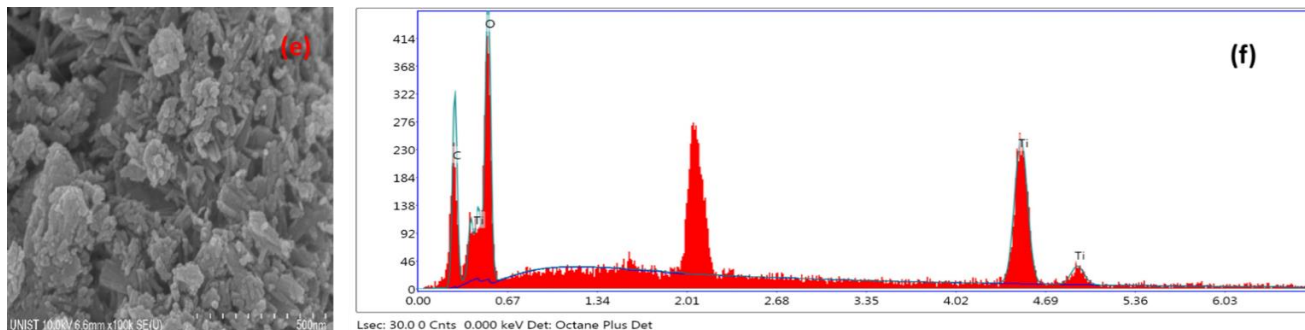
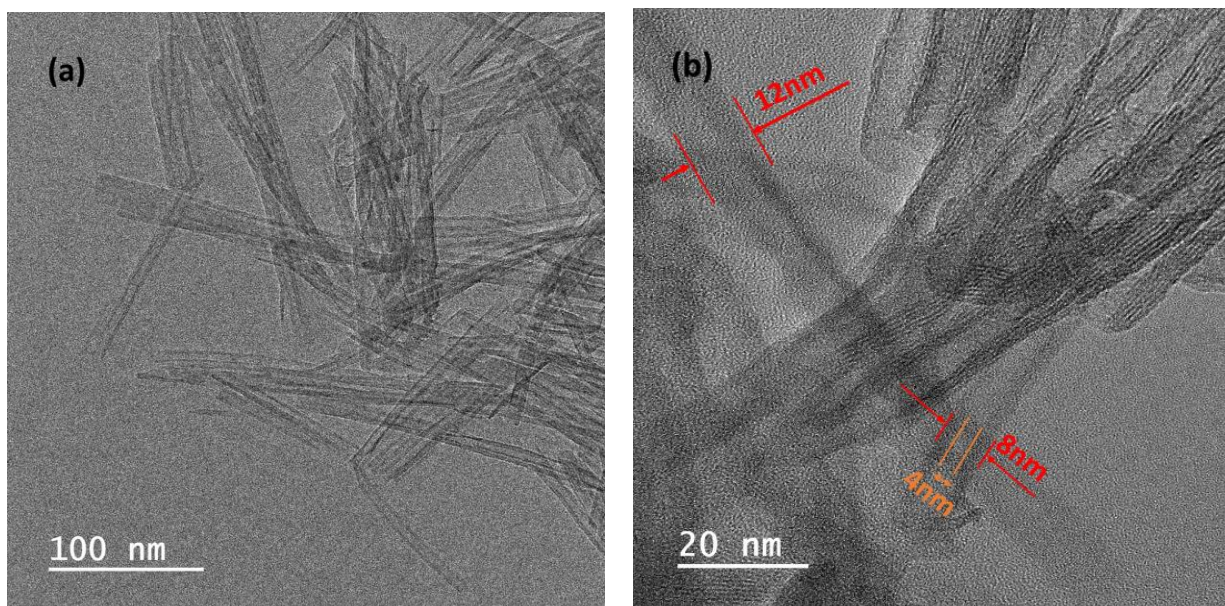


Figure 2. 4 (a) SEM image of NTO, (b) EDX analysis of NTO, (c) SEM image of NTOH0.05, (d) EDX analysis of NTOH0.05, (e) SEM image of NTOH0.1, and (f) EDX analysis of NTOH0.1

### 2.3.1.6. TEM

TEM images of the NTO sample are shown in Fig.5a and b. The as-formed initial  $\text{Na}_2\text{Ti}_3\text{O}_7$  in this sample shows a hollow nanotubular structure with a length of several hundred nanometers, an inner diameter under 5 nm, and an outer diameter from 8 nm to 12 nm. It can be observed that the acid treatment causes a loss of the nanotubular structure and the emergence of titania plate-like nanoparticles on the surface of sodium titanate nanotubes (Fig.5c and d). These plate-like nanoparticles exhibit a width smaller than 12 nm, which suggests the rupturing of nanotubes accompanied by the unfolding process.





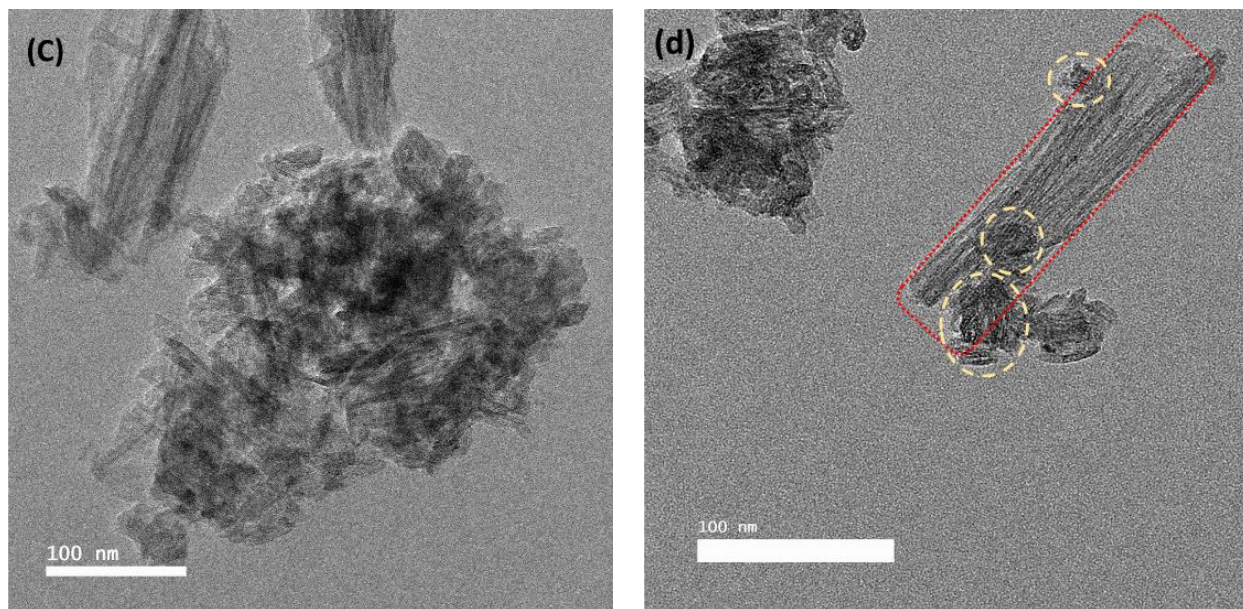


Figure 2. 5. (a) and (b) TEM image of NTO, (c) and (d) TEM image of NTOH0.1

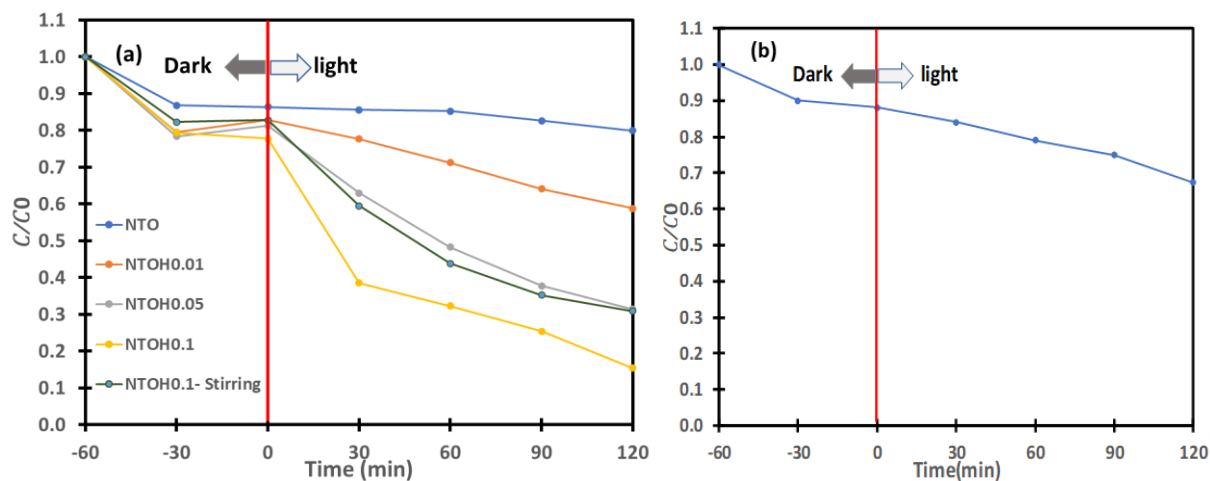
## 2.3.2. Photocatalytic properties

### 2.3.2.1. Effect of HCl concentration

The effect of HCl concentration during the acid treatment process on the activity of NTO for the removal of RhB as a pollutant in aqueous solution was investigated. Fig.6a shows the photodegradation of RhB as a function of irradiation time. NTO shows negligible photodegradation activity on RhB molecules under visible light irradiation after 120 min, which is attributed to the large band gap (3.4 eV) of the sodium titanate. One more experiment was performed using a 150 W Xe lamp for NTO (Fig. 6b). An Xe lamp as a light source gives out a wavelength coinciding with the band gap adsorption of sodium titanate. NTO only shows around a 12% increase in photodegradation activity compared to visible light irradiation. This may indicate the poor crystallinity of sodium titanate nanotubes. When the concentration of HCl aqueous solution was increased up to 0.1 M during the ultrasonic acid treatment process, the removal rate of RhB increased from 20% (for NTO) to 41.2, 68.5, and 84.5% for NTOH0.01,

NTOH0.05, and NTOH0.1, respectively, within 120 min (Fig.6a). The higher photoactivity of NTOH0.1 can be attributed to the increased amount of  $\text{Na}^+$  replaced with  $\text{H}^+$ . Previous studies have confirmed that  $\text{Na}^+$  can act as a recombination center in sodium titanate and consequently decrease the photodegradation efficiency (Fig. 6c)[44].

This study compared the photocatalytic degradation results of the two kinds of experiments conducted with the aid of either stirring or ultrasonic waves to synthesize NTOH0.1 during the acid treatment process. The NTOH0.1 that was obtained by the ultrasonic process showed 15.4% higher photocatalytic activity compared to the NTOH0.1-stirring. This indicates that sonication can promote the replacement of  $\text{Na}^+$  by  $\text{H}^+$ . Consequently, all further experiments to synthesize NTOH0.1 and NTOH0.1Agx were conducted directly by sonication treatment.



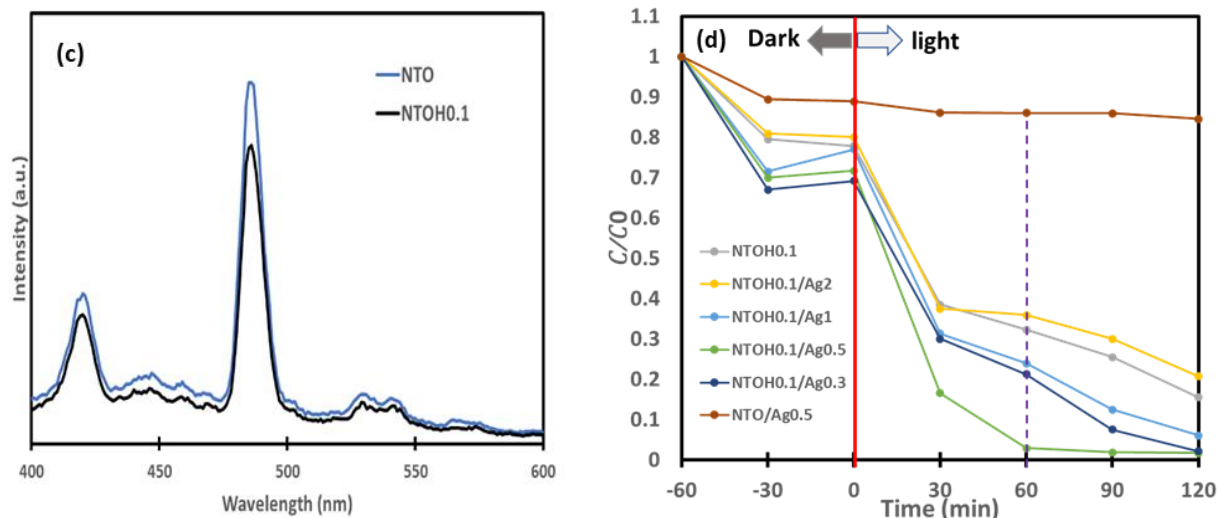


Figure 2. 6. (a) Effect of HCl concentration on photocatalytic activity of NTO, (b) Photodegradation of RhB by NTO under 150 w Xe lamp (c). PL spectra of NTO and NTOH0.1 photocatalysts, and (d) photocatalytic degradation of RhB by NTO, NTOAg0.5, NTOH0.1, and NTOH0.1/Agx

### 2.3.2.2. Effect of silver loading

Fig.6d shows the photodegradation results of RhB over all the photocatalysts loaded with silver (NTO/Ag0.5 and NTOH0.1/Agx samples) under visible light irradiation. NTO/Ag0.5 showed negligible degradation of RhB, as only 14% of RhB was removed after 60 minutes of visible light irradiation. The NTOH0.1/Ag0.5 sample exhibited the highest photocatalytic activity among all photocatalysts tested. After 60 minutes of visible light irradiation, the removal rates of RhB were 64.1, 67.7, 76.1, 78.8, and 97.3% for NTOH0.1/Ag2, NTOH0.1, NTOH0.1/Ag1, NTOH0.1/Ag0.3 and NTOH0.1/Ag0.5, respectively, indicating that the photocatalytic activity of NTOH0.1/Ag0.5 was increased by 29.4% compared to pristine NTOH0.1. The highest photocatalytic activity of NTOH0.1/Ag0.5 among all silver-loaded NTOH0.1 samples is attributed to its visible light absorption, which is also the highest among these samples (see Fig.3b). However, further increasing the silver loading above 0.5 wt% will decrease the RhB degradation activity of photocatalysts as it will cover more of the active sites on the surface of NTOH0.1.

### 2.3.2.3. Reusability of the photocatalyst

The reusability of a photocatalyst is an essential consideration for its practical performance. Therefore, the sample with the best photocatalytic activity performance (NTOH0.1/Ag0.5) has been selected for the evaluation of its reusability properties under identical conditions. After each photodegradation experiment, the photocatalyst was separated from the reaction solution by centrifugation, then washed with distilled water. As shown in Fig.7, there is no considerable loss in degradation rates during five consecutive cycles of the photodegradation of RhB (less than 10%), which can be attributed to the strong contact of silver nanoparticles on the surface of NTOH0.1. The results confirm that the synthesized NTOH0.1/Ag0.5 photocatalyst shows excellent stability for practical performance.

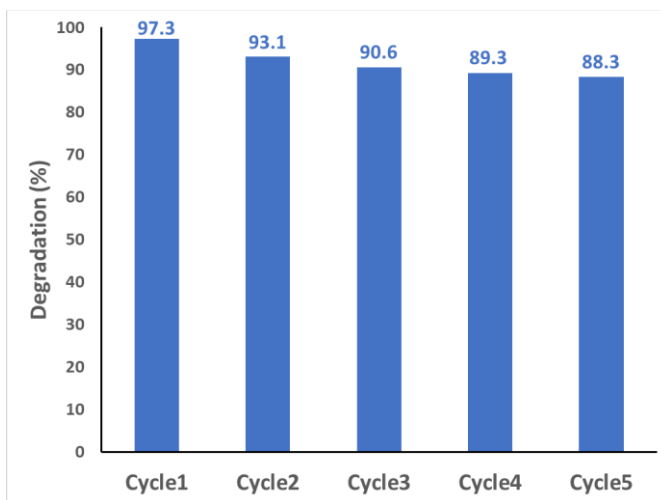
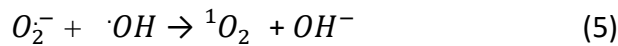
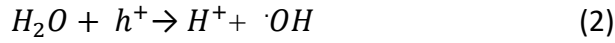
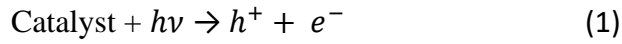


Figure 2. 7 Reusability test of NTOH0.1/Ag0.5

### 2.3.2.4. Mechanism of photocatalytic degradation

A common process for the photocatalytic degradation of a pollutant starts with the photoexcitation of a photocatalyst by providing proper energy above its band gap, leading to the generation of electron-hole pairs. The separated electrons and holes can then react with H<sub>2</sub>O, O<sub>2</sub>, and other groups of chemicals that are absorbed on the surface of the catalyst to form reactive oxygen species

(  $\cdot OH, O_2^-$  and  $^1O_2$  ). Some general processes for the generation of reactive oxygen species (ROS) are given in the following equations:



The role of the main active oxidant species during the photocatalytic process can be determined by adding different scavengers (Fig.8). The 10mM of ethylenediaminetetraacetic acid (EDTA),  $AgNO_3$ ,  $NaN_3$ , or tert-butyl alcohol (TBA) added into the reaction solution respectively acted as an  $h^+$ ,  $e^-$ ,  $^1O_2$ , or  $\cdot OH$  quencher during the photodegradation process. The addition of  $\cdot OH$  scavenger did not lead to any significant change in the photodegradation of RhB after 60 mins. By contrast, when  $NaN_3$  was added into the reaction solution, 57% of RhB was removed during the process, indicating that the degradation of RhB was noticeably suppressed by the addition of  $^1O_2$  scavenger. As shown in equations (4) and (5), singlet oxygen can be formed by the oxidation of  $O_2^-$  by holes or the reaction of  $O_2^-$  with  $\cdot OH$ . Removing  $\cdot OH$  showed almost no effect on the photodegradation process, and consequently, most of  $^1O_2$  will be generated according to Eq. 4. Moreover, the photodegradation efficiency was substantially decreased to 48.4% with the addition of EDTA as a hole scavenger. It can be concluded that most of the holes will participate in the Eq. 4 reaction to produce singlet oxygen, and the remaining ones will act as oxidative agents to react with RhB directly. Photocatalytic activity was only decreased by 11% when  $AgNO_3$  was used as the electron scavenger. With the addition of  $AgNO_3$  and the elimination of the electron,  $^1O_2$  was not formed based on Eqs. 3 and 4, which means that  $^1O_2$  could not participate in the oxidation



process. On the other hand, recombination of electrons and holes will decrease as electrons are captured, and a higher number of holes can be released to react as a direct oxidant during the photodegradation of RhB. Ultimately, the addition of  $\text{AgNO}_3$  reduces the photocatalytic activity from 97.3% to 86% based on these two opposite effects.

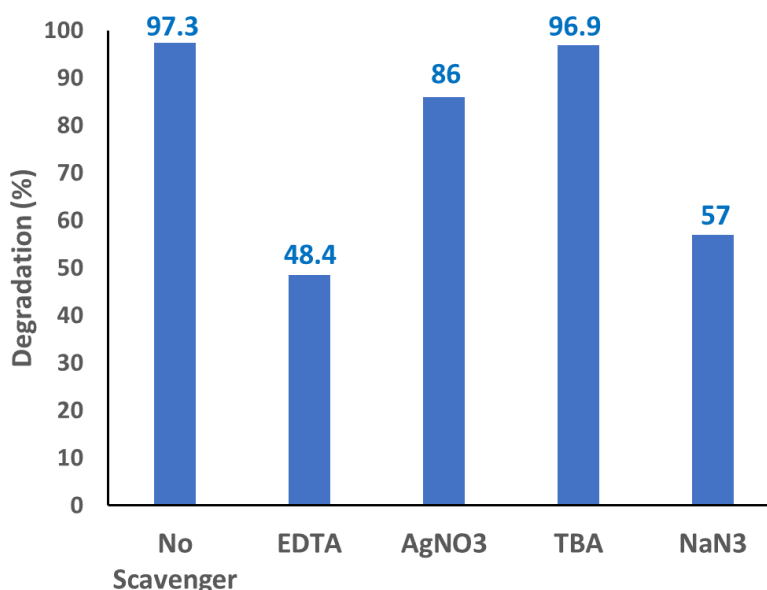
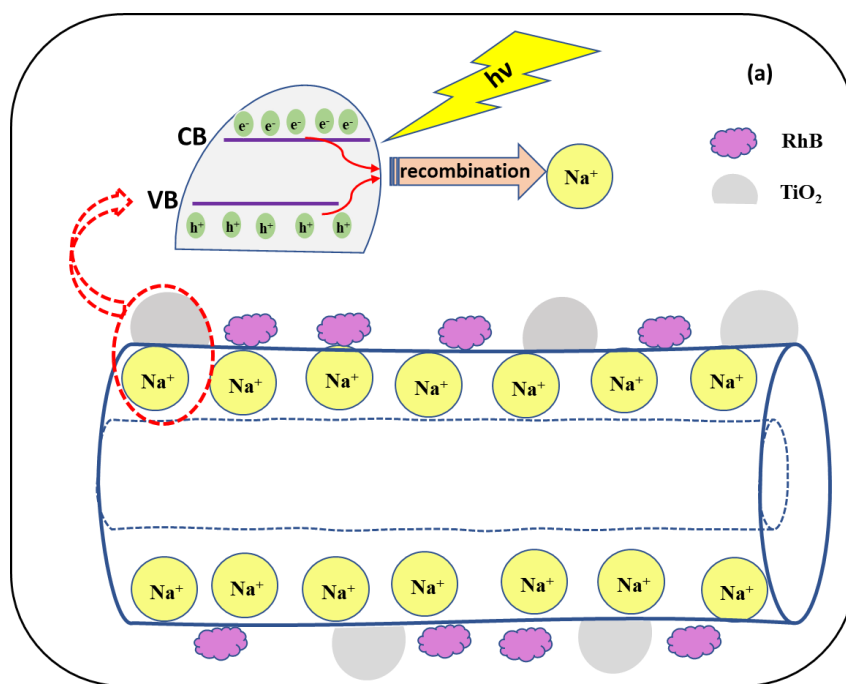


Figure 2. 8. Photocatalytic degradation of RhB on NTOH0.1/Ag0.5 with addition of different scavengers.

Crystallinity, surface area, proportion of light absorption, charge carrier separation, fraction of  $\text{TiO}_2$  phase, and amount of silver loading are several factors that affect the photocatalytic activity of  $\text{Na}_2\text{Ti}_3\text{O}_7/\text{TiO}_2$  nanocomposite. As shown in Fig.9a, when NTO is irradiated with visible light, the poor crystallinity of NTO due to the high percentage of sodium titanate nanotubes, the insignificant amount of light absorption in the visible region, and the presence of  $\text{Na}^+$  as a recombination center lead to insufficient numbers of photogenerated electrons and holes for the photodegradation of RhB. The acid treatment and loading of silver nanoparticles on NTO (Fig.9b)

lead to 1) the removal of  $\text{Na}^+$ , which reduces the recombination of  $e^-$  and  $h^+$  (see Fig. 6c); 2) improved crystallinity of the photocatalyst due to the higher portion of  $\text{TiO}_2$  phase (see Fig.1a); 3) enhanced visible light absorption due to the surface plasmon resonance effect of silver NPs (see Fig.3b); and 4) increased surface area (see Table 1). These several aspects can lead to increases in the numbers of photo-induced electrons and holes as well as the number of absorbed RhB molecules on the surface of the photocatalyst, leading to excellent photocatalytic activity of NTOH0.1/Ag0.5 under visible light irradiation.



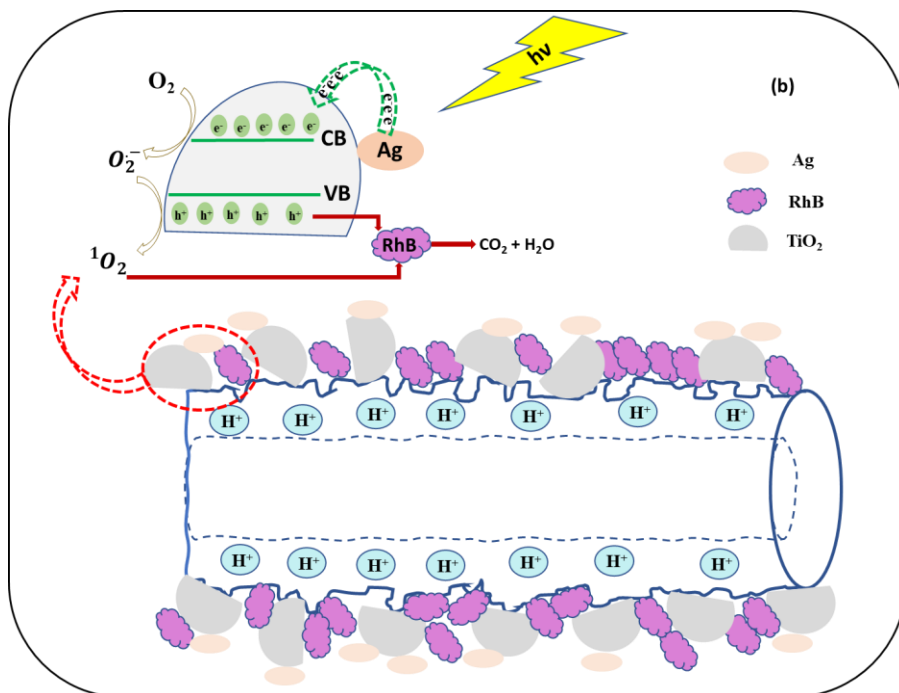


Figure 2. 9. Schematic model illustrating the surface of the photocatalyst and the degradation of RhB (a) before acid treatment, and (b) after acid treatment and silver loading

Table 2. 1. Specific surface area, pore diameter, and pore volume of NTO and NTOH0.1

Catalyst	BET-SA(m <sup>2</sup> /gr)	Pore diameter (nm)	Pore volume (cm <sup>3</sup> /gr)
NTO	151.71	14.73	0.52
NTOH0.1	199.06	11.38	0.49

### 2.3.3. Photoelectrochemical (PEC) properties

Fig.10a shows the photocurrent response of the pure NTO, NTOH0.1, and NTOH0.1/Ag0.5 photoanodes at a constant potential of 0.3 V vs. Ag/AgCl under 100 mW.cm<sup>-2</sup> irradiation. After acid treatment and silver loading, the photocurrent density is significantly enhanced, particularly for the NTOH0.1/Ag0.5 electrode, which shows 2.7 times higher photocurrent density than that of pure NTO. These results suggest that the acid treatment and Ag loading on NTO can result in faster electron-hole transfer and separation, thus leading to a lower charge recombination rate.

Furthermore, improved light harvesting of the NTOH0.1/Ag0.5 electrode leads to increased photocurrent density and PEC performance.

To further study the contributions of the NTO, NTOH0.1, and NTOH0.1/Ag0.5 electrodes, electrochemical impedance spectroscopy (EIS) and Mott-Schottky plots were measured. Fig.10b demonstrates the Nyquist plot of the EIS data obtained for the NTO, NTOH0.1, and NTOH0.1/Ag0.5 electrodes. After combining the acid treatment and Ag loading, the semicircle radius decreases in the following order: NTOH0.1/Ag0.5 < NTOH0.1 < pure NTO. The smaller semicircle radius for the NTOH0.1/Ag0.5 photoanode indicates an increase in the efficient charge carrier transfer at the electrolyte/electrode interface. Furthermore, the increased diffusion of ions to the NTOH0.1/Ag0.5 electrode is due to the high surface area and nanotubular structure of titanites. Hence, the EIS investigation indicates that the electrolyte ions can be diminished due to the lower charge transfer resistance, and this is one of the reasons for the improvement in photocatalytic activity[50].

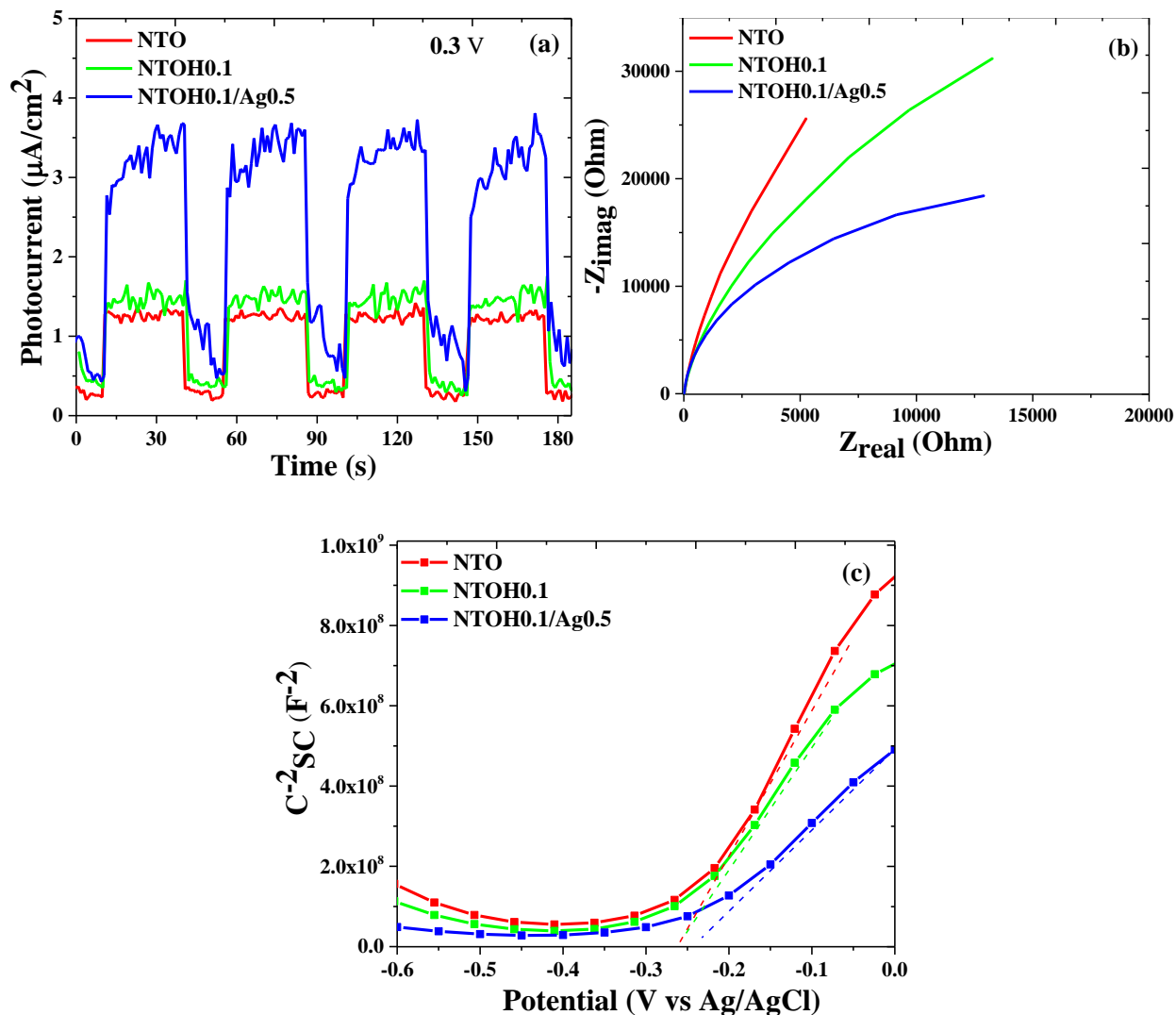


Figure 2. 10. (a) Photocurrent response at a potential of 0.3 V (vs. Ag/AgCl), (b) EIS Nyquist plot, and (c) Mott-Schottky plot of the NTO, NTOH0.1, and NTOH0.1/Ag0.5 electrodes under 100  $\text{mW}\cdot\text{cm}^{-2}$  irradiation; the supporting electrolyte was a 0.5M aqueous solution of  $\text{Na}_2\text{SO}_3$ .

Furthermore, Mott-Schottky plot analysis was conducted to evaluate the donor concentrations ( $N_D$ ) and flat band potentials of the NTO, NTOH0.1, and NTOH0.1/Ag0.5 photoelectrodes. Donor concentration and flat band potential were estimated on the Mott-Schottky plot using the following equations [51-53].

$$\frac{1}{C^2} = \frac{2}{\epsilon\epsilon_0 A^2 e N_D} \left( V - V_{fb} - \frac{K_B T}{e} \right)$$

$$Slope = \frac{2}{\epsilon\epsilon_0 A^2 e N_D} \rightarrow N_D = \frac{2}{\epsilon\epsilon_0 A^2 e (Slope)}$$

$$intercept = V_{fb} + \frac{K_B T}{e} \rightarrow V_{fb} = intercept - \frac{K_B T}{e}$$

Where C is the capacitance of the space charge layers,  $e$  is the electron charge ( $1.60 \times 10^{-19}$  C),  $\epsilon$  is the dielectric constant of the  $\text{Na}_2\text{Ti}_3\text{O}_7$  (3.9),  $\epsilon_0$  is the vacuum permittivity ( $8.854 \times 10^{-14}$  F/cm),  $N_D$  is the donor density ( $\text{cm}^{-3}$ ), and  $k_B$  is the Boltzmann constant ( $1.38 \times 10^{-23}$  J.  $\text{K}^{-1}$ ).

The donor concentration can be measured from the slope of the Mott-Schottky plot, and  $V_{fb}$  is obtained as the value of the x-intercept. Fig.10c shows that the Mott-Schottky curves have a less steep slope after the acid treatment and Ag loading in the linear region, which indicates an increased donor concentration ( $N_D$ ). The flat band potential ( $V_{fb}$ ) and donor concentration results calculated using the intercepts and slopes of the Mott-Schottky plots are summarized in Table 2.

The  $N_D$  of the NTOH0.1/Ag0.5 electrode is  $6.60 \times 10^{27} \text{ m}^{-3}$ , which is 1.8 times higher than that of pure NTO ( $3.50 \times 10^{27} \text{ m}^{-3}$ ). This is strong evidence of the improved electron transport and reduced recombination of charge carriers in the NTOH0.1/Ag0.5 photoanode after the acid treatment and Ag loading, which in turn helps enhance the photocurrent density and photoelectrochemical performance.

Table 2. 2. Summarized  $V_{fb}$  and  $N_D$  values obtained from the intercept and the slope in Mott-Schottky plots

<b>Samples</b>	<b>slope</b>	<b>intercept</b>	<b><math>N_D</math> (<math>m^{-3}</math>)</b>	<b><math>V_{fb}</math> (V)</b>
<b>NTO</b>	2.58E+09	-0.26	3.50E+27	-0.28
<b>NTOH0.1</b>	2.04E+09	-0.26	4.43E+27	-0.28
<b>NTOH0.1/Ag0.5</b>	1.37E+09	-0.24	6.60E+27	-0.26

## 2.4. Conclusion:

The acid treatment with different concentrations of HCl aqueous solution (0.01, 0.05, and 0.1M) under ultrasonic irradiation at 50°C and the Ag loading (0.3, 0.5, 1, and 2 wt%) by the impregnation method on the  $Na_2Ti_3O_7/TiO_2$  nanocomposite greatly improved the PEC performance and the photodegradation of RhB in aqueous solution. The acid treatment with HCl 0.1M led to a desirable loss of nanotubular structure along with the emergence of titania plate-like nanoparticles (width smaller than 12 nm) on the surface of hydrogen titanate nanotubes. The nanocomposite with the surface properties of the  $TiO_2$  nanocrystal and the high surface area of titanate nanotubes showed a remarkable increase in photocatalytic activity under visible light irradiation. The acid-treated NTOH0.1 showed 64.5% higher photodegradation activity than that of the untreated catalyst after 120 min. This enhancement is attributed to the removal of  $Na^+$  as a recombination center of  $e^-$  and  $h^+$ , improving the crystallinity of the photocatalyst, enhancing the visible light absorption and increasing the surface area during the acid treatment process. The NTOH0.1/Ag0.5 nanocomposite with the optimized acid treatment and silver loading showed 97.3% photodegradation of RhB after 60 min irradiation, which was 82.6% higher than that of the pristine catalyst, due to a combination of the acid treatment effect and the greatly enhanced surface plasmon effect of silver on the photocatalyst. The NTOH0.1/Ag0.5 photoanode also showed 2.7 times higher photocurrent

density than that of the untreated photoanode. Combined analyses of Mott-Schottky plots and electrochemical impedance spectroscopy (EIS) of NTOH0.1/Ag0.5 nanocomposite confirmed that the acid treatments and silver (Ag) loading increased the donor concentration ( $N_D$ ) and the charge carrier transfer efficiency, thus leading to improved PEC performance.



## Reference:

- [1] M. Tayebi, A. Tayyebi, Z. Masoumi, B.-K. Lee, Photocorrosion suppression and photoelectrochemical (PEC) enhancement of ZnO via hybridization with graphene nanosheets, *Applied Surface Science*, 502 (2020) 144189.
- [2] M. Tayebi, A. Tayyebi, T. Soltani, B.-K. Lee, pH-Dependent photocatalytic performance of modified bismuth vanadate by bismuth ferrite, *New Journal of Chemistry*, 43 (2019) 9106-9115.
- [3] A. Tayyebi, M. Tayebi, A. Shafikhani, S.S. Şengör, ZnO quantum dots-graphene composites: Formation mechanism and enhanced photocatalytic activity for degradation of methyl orange dye, *Journal of Alloys and Compounds*, 663 (2016) 738-749.
- [4] J. Chen, X. Zhou, C. Mei, J. Xu, C.-P.J.E.A. Wong, Improving the sodiation performance of Na<sub>2</sub>Ti<sub>3</sub>O<sub>7</sub> through Nb-doping, 224 (2017) 446-451.
- [5] J. Wang, D.N. Tafen, J.P. Lewis, Z. Hong, A. Manivannan, M. Zhi, M. Li, N.J.J.o.t.A.C.S. Wu, Origin of photocatalytic activity of nitrogen-doped TiO<sub>2</sub> nanobelts, 131 (2009) 12290-12297.
- [6] X. Zhang, J. Yuan, H. Yu, X. Zhu, Z. Yin, H. Shen, Y.J.J.o.A. Xie, Compounds, Synthesis, conversion, and comparison of the photocatalytic and electrochemical properties of Na<sub>2</sub>Ti<sub>6</sub>O<sub>13</sub> and Li<sub>2</sub>Ti<sub>6</sub>O<sub>13</sub> nanobelts, 631 (2015) 171-177.
- [7] H. Yoshida, L. Zhang, M. Sato, T. Morikawa, T. Kajino, T. Sekito, S. Matsumoto, H.J.C.T. Hirata, Calcium titanate photocatalyst prepared by a flux method for reduction of carbon dioxide with water, 251 (2015) 132-139.
- [8] C.-Y. Xu, J. Wu, P. Zhang, S.-P. Hu, J.-X. Cui, Z.-Q. Wang, Y.-D. Huang, L.J.C. Zhen, Molten salt synthesis of Na<sub>2</sub>Ti<sub>3</sub>O<sub>7</sub> and Na<sub>2</sub>Ti<sub>6</sub>O<sub>13</sub> one-dimensional nanostructures and their photocatalytic and humidity sensing properties, 15 (2013) 3448-3454.
- [9] M. Tayebi, M. Kolaie, A. Tayyebi, Z. Masoumi, Z. Belbasi, B.-K.J.S.E. Lee, Reduced graphene oxide (RGO) on TiO<sub>2</sub> for an improved photoelectrochemical (PEC) and photocatalytic activity, 190 (2019) 185-194.
- [10] A. Sandoval, C. Hernández-Ventura, T.E.J.F. Klimova, Titanate nanotubes for removal of methylene blue dye by combined adsorption and photocatalysis, 198 (2017) 22-30.
- [11] T. Zhang, Y. Liu, Y. Rao, X. Li, D. Yuan, S. Tang, Q.J.C.E.J. Zhao, Enhanced photocatalytic activity of TiO<sub>2</sub> with acetylene black and persulfate for degradation of tetracycline hydrochloride under visible light, 384 (2020) 123350.
- [12] M.A.B. Adnan, K. Arifin, L.J. Minggu, M.B.I.I.J.o.H.E. Kassim, Titanate-based perovskites for photochemical and photoelectrochemical water splitting applications: a review, 43 (2018) 23209-23220.
- [13] M. Tayebi, B.-K. Lee, Recent advances in BiVO<sub>4</sub> semiconductor materials for hydrogen production using photoelectrochemical water splitting, *Renewable and Sustainable Energy Reviews*, 111 (2019) 332-343.
- [14] M. Tayebi, A. Tayyebi, B.-K. Lee, Improved photoelectrochemical performance of molybdenum (Mo)-doped monoclinic bismuth vanadate with increasing donor concentration, *Catalysis Today*, 328 (2019) 35-42.
- [15] M. Tayebi, A. Tayyebi, B.-K. Lee, C.-H. Lee, D.-H. Lim, The effect of silver doping on photoelectrochemical (PEC) properties of bismuth vanadate for hydrogen production, *Solar Energy Materials and Solar Cells*, 200 (2019) 109943.
- [16] C.W. Kim, S.H. Ji, D.I. Kang, Y.S. Kang, Growth of Single Crystalline TiO<sub>2</sub> Nanorods as a Photoanode for Dye-Sensitized Solar Cell, *Materials Science Forum*, Trans Tech Publ, 2017, pp. 144-150.
- [17] C.-H. Li, C.-W. Hsu, S.-Y.J.J.o.c. Lu, i. science, TiO<sub>2</sub> nanocrystals decorated Z-schemed core-shell CdS-CdO nanorod arrays as high efficiency anodes for photoelectrochemical hydrogen generation, 521 (2018) 216-225.

- [18] S.-W. Lai, J.-W. Park, S.-H. Yoo, J.-M. Ha, E.-H. Song, S.-O.J.i.j.o.h.e. Cho, Surface synergism of Pd/H<sub>2</sub>Ti<sub>3</sub>O<sub>7</sub> composite nanowires for catalytic and photocatalytic hydrogen production from ammonia borane, 41 (2016) 3428-3435.
- [19] P. Sokhandani, A.A. Babaluo, M. Rezaei, M. Shahrezaei, A. Hasanzadeh, S.G. Mehmandoust, R. Mehdizadeh, Nanocomposites of PVC/TiO<sub>2</sub> nanorods: Surface tension and mechanical properties before and after UV exposure, *Journal of Applied Polymer Science*, 129 (2013) 3265-3272.
- [20] M. Shahrezaei, S. Habibzadeh, A.A. Babaluo, H. Hosseinkhani, M. Haghighi, A. Hasanzadeh, R. Tahmasebpour, Study of synthesis parameters and photocatalytic activity of TiO<sub>2</sub> nanostructures, *Journal of Experimental Nanoscience*, 12 (2017) 45-61.
- [21] R. Tahmasebpour, A.A. Babaluo, J.R. Shahrouzi, M. Tahmasebpour, M. Shahrezaei, Theoretical and experimental studies on the anodic oxidation process for synthesis of self-ordering TiO<sub>2</sub> nanotubes: Effect of TiO<sub>2</sub> nanotube lengths on photocatalytic activity, *Journal of environmental chemical engineering*, 5 (2017) 1227-1237.
- [22] M. Shahrezaei, A.A. Babaluo, S. Habibzadeh, M. Haghighi, Photocatalytic Properties of 1D TiO<sub>2</sub> Nanostructures Prepared from Polyacrylamide Gel–TiO<sub>2</sub> Nanopowders by Hydrothermal Synthesis, *European Journal of Inorganic Chemistry*, 2017 (2017) 694-703.
- [23] X. Hu, Z. Sun, J. Song, G. Zhang, C. Li, S.J.J.o.c. Zheng, i. science, Synthesis of novel ternary heterogeneous BiOCl/TiO<sub>2</sub>/sepiolite composite with enhanced visible-light-induced photocatalytic activity towards tetracycline, 533 (2019) 238-250.
- [24] D. Gong, W.C.J. Ho, Y. Tang, Q. Tay, Y. Lai, J.G. Highfield, Z.J.J.o.S.S.C. Chen, Silver decorated titanate/titania nanostructures for efficient solar driven photocatalysis, 189 (2012) 117-122.
- [25] S. Wu, H. Hu, Y. Lin, J. Zhang, Y.H.J.C.E.J. Hu, Visible light photocatalytic degradation of tetracycline over TiO<sub>2</sub>, 382 (2020) 122842.
- [26] V.M. Daskalaki, M. Antoniadou, G. Li Puma, D.I. Kondarides, P.J.E.s. Lianos, technology, Solar light-responsive Pt/CdS/TiO<sub>2</sub> photocatalysts for hydrogen production and simultaneous degradation of inorganic or organic sacrificial agents in wastewater, 44 (2010) 7200-7205.
- [27] V. Etacheri, C. Di Valentin, J. Schneider, D. Bahnemann, S.C.J.J.o.P. Pillai, P.C.P. Reviews, Visible-light activation of TiO<sub>2</sub> photocatalysts: Advances in theory and experiments, 25 (2015) 1-29.
- [28] H. Zhu, X. Gao, Y. Lan, D. Song, Y. Xi, J.J.J.o.t.A.C.S. Zhao, Hydrogen titanate nanofibers covered with anatase nanocrystals: a delicate structure achieved by the wet chemistry reaction of the titanate nanofibers, 126 (2004) 8380-8381.
- [29] M.A. Tsiamsouri, P.K. Allan, A.J. Pell, J.M. Stratford, G. Kim, R.N. Kerber, P.C. Magusin, D.A. Jefferson, C.P.J.C.o.M. Grey, Exfoliation of layered Na-ion anode material Na<sub>2</sub>Ti<sub>3</sub>O<sub>7</sub> for enhanced capacity and cyclability, 30 (2018) 1505-1516.
- [30] Y.-C. Chang, J.-C. Lin, S.-H.J.J.o.A. Wu, Compounds, One-step growth of Na<sub>2</sub>Ti<sub>3</sub>O<sub>7</sub> nanorods for enhanced photocatalytic activities and recyclability, 749 (2018) 955-960.
- [31] X. Sun, Y.J.C.A.E.J. Li, Synthesis and characterization of ion-exchangeable titanate nanotubes, 9 (2003) 2229-2238.
- [32] D.V. Bavykin, J.M. Friedrich, F.C.J.A.m. Walsh, Protonated titanates and TiO<sub>2</sub> nanostructured materials: synthesis, properties, and applications, 18 (2006) 2807-2824.
- [33] A. Sclafani, M.-N. Mozzanega, P.J.J.o.P. Pichat, P.A. Chemistry, Effect of silver deposits on the photocatalytic activity of titanium dioxide samples for the dehydrogenation or oxidation of 2-propanol, 59 (1991) 181-189.
- [34] B. Neppolian, A. Bruno, C.L. Bianchi, M.J.U.s. Ashokkumar, Graphene oxide based Pt–TiO<sub>2</sub> photocatalyst: ultrasound assisted synthesis, characterization and catalytic efficiency, 19 (2012) 9-15.
- [35] X. Chen, H.Y. Zhu, J.C. Zhao, Z.F. Zheng, X.P.J.A.C.I.E. Gao, Visible-light-driven oxidation of organic contaminants in air with gold nanoparticle catalysts on oxide supports, 47 (2008) 5353-5356.

- [36] B. Neppolian, H. Jung, H.J.J.o.A.O.T. Choi, Photocatalytic degradation of 4-chlorophenol using TiO<sub>2</sub> and Pt-TiO<sub>2</sub> nanoparticles prepared by sol-gel method, 10 (2007) 369-374.
- [37] O. Nasr, O. Mohamed, A.-S. Al-Shirbini, A.-M.J.J.o.P. Abdel-Wahab, P.A. Chemistry, Photocatalytic degradation of acetaminophen over Ag, Au and Pt loaded TiO<sub>2</sub> using solar light, 374 (2019) 185-193.
- [38] Y. Sun, Y. Gao, J. Zeng, J. Guo, H.J.M.L. Wang, Enhancing visible-light photocatalytic activity of Ag-TiO<sub>2</sub> nanowire composites by one-step hydrothermal process, 279 (2020) 128506.
- [39] L. Lu, G. Wang, Z. Xiong, Z. Hu, Y. Liao, J. Wang, J.J.C.I. Li, Enhanced photocatalytic activity under visible light by the synergistic effects of plasmonics and Ti<sup>3+</sup>-doping at the Ag/TiO<sub>2</sub>-x heterojunction, (2020).
- [40] Y. Zhang, T. Wang, M. Zhou, Y. Wang, Z.J.C.I. Zhang, Hydrothermal preparation of Ag-TiO<sub>2</sub> nanostructures with exposed {001}/{101} facets for enhancing visible light photocatalytic activity, 43 (2017) 3118-3126.
- [41] C. Díaz-Urbe, J. Vilorio, L. Cervantes, W. Vallejo, K. Navarro, E. Romero, C.J.I.J.o.P. Quiñones, Photocatalytic activity of Ag-TiO<sub>2</sub> composites deposited by photoreduction under UV irradiation, 2018 (2018).
- [42] R. Zhou, S. Lin, H. Zong, T. Huang, F. Li, J. Pan, J.J.J.o.N. Cui, Continuous synthesis of Ag/TiO<sub>2</sub> nanoparticles with enhanced photocatalytic activity by pulsed laser ablation, 2017 (2017).
- [43] K. Thamaphat, P. Limsuwan, B.J.K.J. Ngotawornchai, Phase characterization of TiO<sub>2</sub> powder by XRD and TEM, 42 (2008) 357-361.
- [44] A. Turki, H. Kochkar, C. Guillard, G. Berhault, A.J.A.C.B.E. Ghorbel, Effect of Na content and thermal treatment of titanate nanotubes on the photocatalytic degradation of formic acid, 138 (2013) 401-415.
- [45] H. Liu, Z. Zheng, D. Yang, E. Waclawik, X. Ke, H. Zhu, S. Palmer, R.L.J.J.o.R.S. Frost, A Raman spectroscopic study on the allocation of ammonium adsorbing sites on H<sub>2</sub>Ti<sub>3</sub>O<sub>7</sub> nanofibre and its structural derivation during calcination, 41 (2010) 1601-1605.
- [46] X. Yan, D. Sun, J. Jiang, W. Yan, Y.J.J.o.A. Jin, Compounds, Self-assembled twine-like Na<sub>2</sub>Ti<sub>3</sub>O<sub>7</sub> nanostructure as advanced anode for sodium-ion batteries, 697 (2017) 208-214.
- [47] Y. Wang, Y. Su, L. Qiao, L. Liu, Q. Su, C. Zhu, X.J.N. Liu, Synthesis of one-dimensional TiO<sub>2</sub>/V<sub>2</sub>O<sub>5</sub> branched heterostructures and their visible light photocatalytic activity towards Rhodamine B, 22 (2011) 225702.
- [48] J. Li, J. Xu, J.J.C. Huang, Nanofibrous vanadium-doped rutile titania derived from cellulose substance by flame synthesis, 16 (2014) 375-384.
- [49] Z.H. Shah, J. Wang, Y. Ge, C. Wang, W. Mao, S. Zhang, R.J.J.o.M.C.A. Lu, Highly enhanced plasmonic photocatalytic activity of Ag/AgCl/TiO<sub>2</sub> by CuO co-catalyst, 3 (2015) 3568-3575.
- [50] S.P. Vattikuti, P.A.K. Reddy, P. NagaJyothi, J. Shim, C. Byon, Hydrothermally synthesized Na<sub>2</sub>Ti<sub>3</sub>O<sub>7</sub> nanotube-V<sub>2</sub>O<sub>5</sub> heterostructures with improved visible photocatalytic degradation and hydrogen evolution-Its photocorrosion suppression, Journal of Alloys and Compounds, 740 (2018) 574-586.
- [51] M. Tayebi, B.-K. Lee, The Effects of W/Mo-co-doped BiVO<sub>4</sub> Photoanodes for Improving Photoelectrochemical Water Splitting Performance, Catalysis Today, (2020).
- [52] J. Xia, H. Zhao, W.K. Pang, Z. Yin, B. Zhou, G. He, Z. Guo, Y. Du, Lanthanide doping induced electrochemical enhancement of Na<sub>2</sub>Ti<sub>3</sub>O<sub>7</sub> anodes for sodium-ion batteries, Chemical science, 9 (2018) 3421-3425.
- [53] M. Tayebi, A. Tayyebi, B.-K. Lee, Photocharged molybdenum-doped BiVO<sub>4</sub> photoanodes for simultaneous enhancements in charge transport and surface passivation, Solar Energy, 191 (2019) 427-434.

# **Chapter 3: Heterojunction of sodium titanate nanorods with visible semiconductor (CdS nanoparticle)**

## **Abstract**

This study provided preparation and application of a highly efficient photoanode having dense and efficient sodium titanate (NTO) nanorods decorated with CdS nanoparticles. The (NTO) nanorods were grown densely on the surface of Ti foil by one step hydrothermal method, which provide many step edges on the surface of nanorods, and a direct pathway for transfer of photogenerated electrons to the Ti substrate to improve water splitting ability. The CdS nanoparticles were deposited on the surface of NTO nanorods using a simple and low-cost successive ionic layer adsorption and reaction (SILAR) method to greatly enhance the absorption of visible light. Rough surfaces of as synthesized nanorods were favored places for growing the CdS nanoparticles, which formed a tremendous connection and heterojunction at the interface between the NTO and CdS. This efficient connection caused the noticeable enhancement in photocurrent density with great stability in integrated NTO/CdS photoanodes, due to the efficient separation and transfer of charge carriers. The NTO/CdS12 electrode with the optimum SILAR cycles showed the highest photocurrent density around  $2.37 \text{ mA/cm}^2$  at 1 V vs RHE, which was 36 times higher than that of the pure NTO (around  $0.066 \text{ mA/cm}^2$ ), and interestingly, this electrode retained more than 95% of its initial photocurrent density, even after 6,000 seconds.

## **3.1. Introduction**

During recent decades, the rapid growth in the human population and industrialization has generated two crucial problems: environmental pollution and energy shortage. Emission of  $\text{CO}_2$

from combustion of fossil fuels to produce energy has resulted in the global warming and global climate change issues. Efficient and practical techniques for conversion of tremendous solar energy into clean energy sources are needed to solve the two crucial issues that we faced in the present century [1-6].

Solar water splitting and CO<sub>2</sub> reduction would be the greenest technology for Conversion of water and CO<sub>2</sub> into H<sub>2</sub> and hydrocarbons, as a renewable energy resource and solar chemical fuel, respectively. Hydrogen is most attractive and cleanest solar chemical fuel that does not result in any carbon emission during its oxidation in a fuel cell [7-10]. Photoelectrochemical (PEC) water splitting using semiconductor as a photoelectrode is one of the most promising routes for clean production of hydrogen, which can strongly compete with other traditional hydrogen generation methods, like steam reforming of methane [11-16].

Among the numerous semiconductors, sodium titanate nanostructures (NTO) have received considerable attention, due to their special physical and chemical properties that include large specific area, good structural stability, high chemical inertness and ion exchange stability [17]. Moreover, sodium titanate has a proper band edge position for both hydrogen reduction and water oxidation processes, which make it proper candidate for photoelectrochemical water splitting applications. However, due to its intrinsic wide bandgap of sodium titanates, which is around 3.4 eV, they can be photocatalytically active under UV light irradiation [18]. Their high rate recombination of photoinduced electrons and holes cause to low quantum efficiency of photocatalytic reactions. Even though there have been some reports that showed photoelectrochemical properties of sodium titanate in powder form, some issues for practical applications of NTO, such as aggregation, scattering and separation of powder from substrate should be resolved [19, 20]. Growing sodium titanate directly on the surface of Ti foil substrate

can improve noticeably these problems. Furthermore, direct contacts of sodium titanate nanostructures with metal substrate can facilitate transfer of photogenerated charge carriers from active nanoparticle to the substrate [21]. Thus, the introduction of smart ideas to decrease the resistance of charge transfer can contribute to greatly improving the PEC performance of the NTO photoelectrodes.

Light absorption limitation of sodium titanate nanostructures because of their wide band gap energy under solar light irradiation can be solved by depositing narrow band gap materials onto the NTO nanostructures. CdS is a supreme narrow band gap semiconductor that can sensitize sodium titanate to improve its photoresponse to the visible light region [22-24]. In addition, suitable band alignment between sodium titanate and CdS can modulate the separation and transfer of photogenerated charge carriers to consequently increase their photoelectrochemical properties. To the best of our knowledge, this is the first study to investigate the PEC performance of pure NTO nanorods with many step edges on their top surface that were grown densely on the surface of Ti foil by a hydrothermal method, without any further treatment. The successive ionic layer adsorption and reaction (SILAR) method was employed to deposit CdS nanoparticles on the surface of NTO nanorods. The number of SILAR cycles deposition on NTO nanorods were optimized by measuring the photocurrent density of the different photoanode samples. This study systematically investigated the PEC improvement behaviors of different NTO/CdS<sub>x</sub> samples by electrochemical impedance spectroscopy (EIS), Mott-Schottky, open circuit potential (OCP), applied bias photon to current conversion efficiency (ABPE) and incident photon current efficiency (IPCE) analyses.

## **3.2. Experimental procedure**

### **3.2.1. Catalyst preparation**

#### **3.2.1.1. Fabrication of NTO nanorods film**

Ti foil with appropriate size as a substrate was first immersed in acetone, ethanol and distilled water solution for 15 min under sonication, to remove the surface organic contamination. After rinsing with distilled water, Ti foil was placed in 50 mL of Teflon lined stainless steel autoclave that was filled with 20 mL of 0.25 M NaOH aqueous solution, followed by hydrothermal treatment at 200 °C for 20 h. The sample was then rinsed with distilled water and ethanol, and finally dried in an air oven at 60 °C.

#### **3.2.1.2. Fabrication of NTO/CdS<sub>x</sub> photoanodes**

The CdS nanoparticles were deposited on the NTO nanorods by SILAR technique. NTO nanorods film was immersed in 0.5 M cadmium nitrate (1:1 methanol-water) solution for 5 min for Cd<sup>2+</sup> cations to adhere to the surface of nanorods. Then, sample was rinsed with ethanol and distilled water to remove the weakly anchored Cd<sup>2+</sup> dots. Afterwards, the film was dipped in 0.5 M sodium sulfide aqueous solution for 5 min to react S<sup>2-</sup> with Cd<sup>2+</sup> cations, following by rinsing. The above procedure was named one SILAR cycle. We prepared different samples with 3, 7, 9, 12 and 15 cycles, which were named as NTO/CdS<sub>3</sub>, NTO/CdS<sub>7</sub>, NTO/CdS<sub>9</sub>, NTO/CdS<sub>12</sub> and NTO/CdS<sub>15</sub>, respectively. In the last stage, all samples were placed in the furnace for 2 h at 300 °C for a calcination.

### **3.2.2. Photoelectrochemical (PEC) performance**

Photoelectrochemical measurements of different photoanodes were investigated with a typical three-electrode electrochemical cell. Photoanode was as a working electrode, Pt wire as the

counter electrode, and the RHE as a reference electrode. The electrolyte was a 0.5M aqueous solution of  $\text{Na}_2\text{SO}_3$  at pH=9.

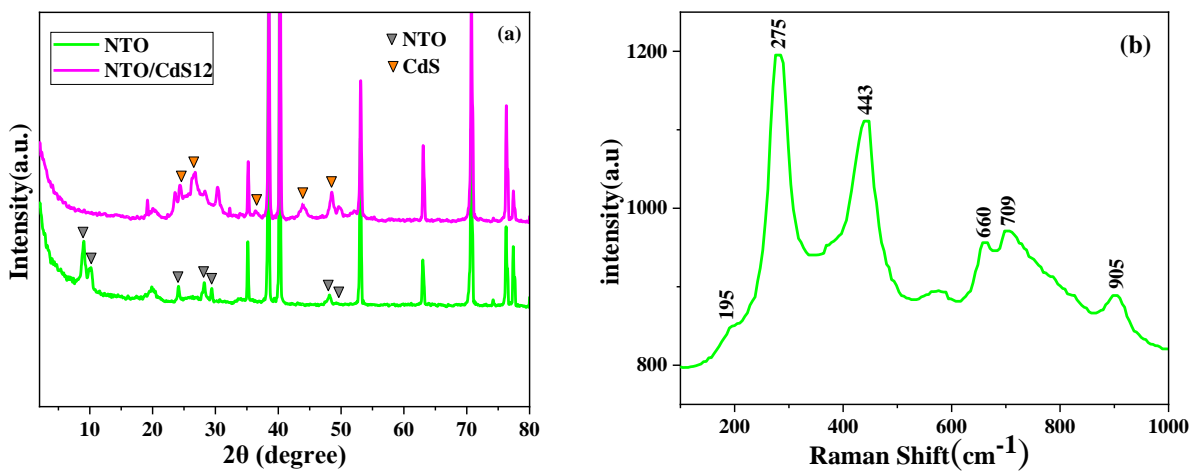
The PEC activity of the pure NTO and NTO/CdSx photoanodes were measured under irradiation of a 300W Xenon lamp calibrated to  $100 \text{ mW/cm}^2$  from the front side of the photoanodes in the scan range from -0.15 to 2 V (vs. RHE).

### 3.3. Results and discussion

#### 3.3.1. Characterization of the synthesized photoanodes

##### 3.3.1.1. XRD

Figure 1a demonstrates the XRD patterns of sodium titanate nanorod film (NTO) and NTO nanorod film loaded with 12 SILAR cycles of Cd and S ions (NTO/CdS12). The presence of additional peaks at the two-theta angle of  $9.36^\circ, 10.1^\circ, 24.2^\circ, 28.1^\circ, 29.5^\circ, 48.2^\circ$  and  $49.36^\circ$  in the XRD patterns of NTO compared to Ti foil confirmed the formation of sodium titanate (which consist of both sodium trititanate and sodium hexatitanate) [25, 26]. In addition, the presence of diffraction peaks at  $2\theta = 24.96, 26.6, 36.7, 43.71$  and  $47.86^\circ$  correspond to the (100), (002), (102), (110) and (103) planes are assigned to the existence of hexagonal CdS phase in NTO/CdS12 [27].





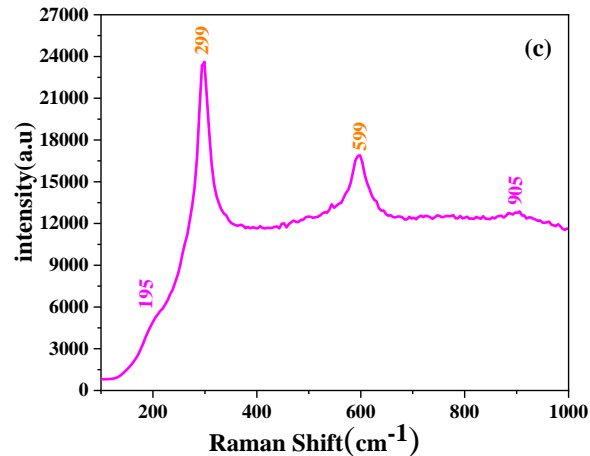


Figure 3. 1. (a) XRD patterns of Ti foil, NTO and NTO/CdS12, (b) Raman spectra of NTO, (c) Raman spectra of NTO/CdS12

### 3.3.1.2 Raman

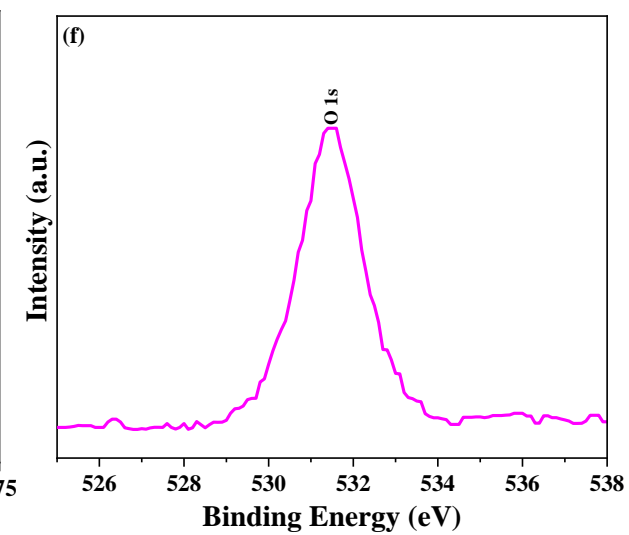
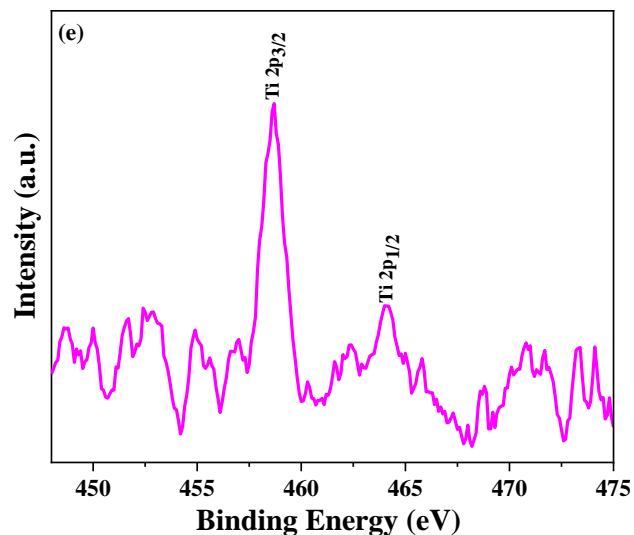
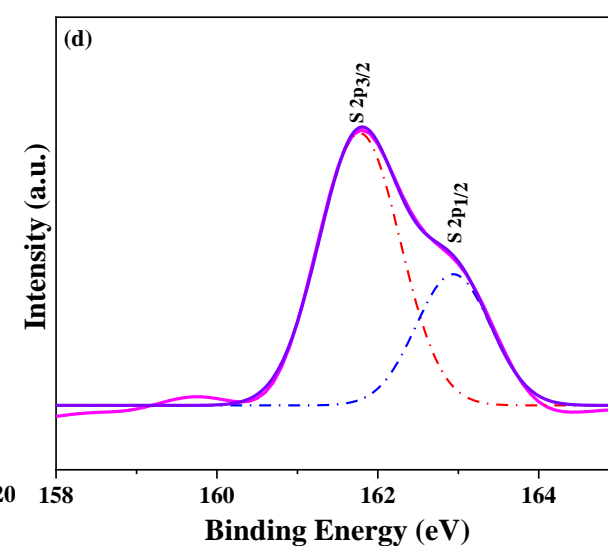
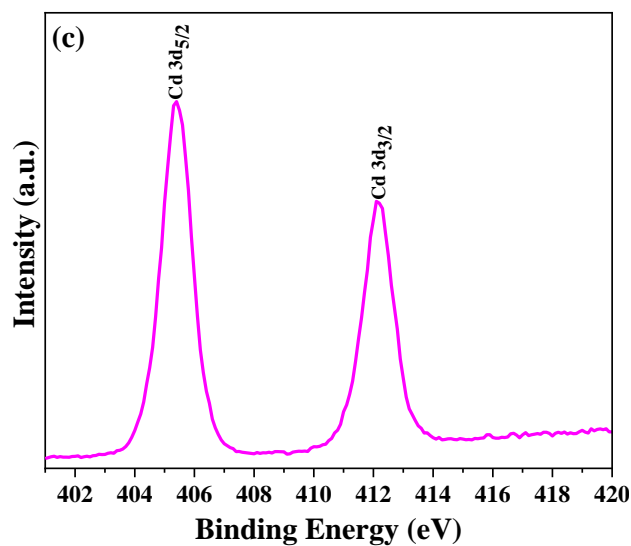
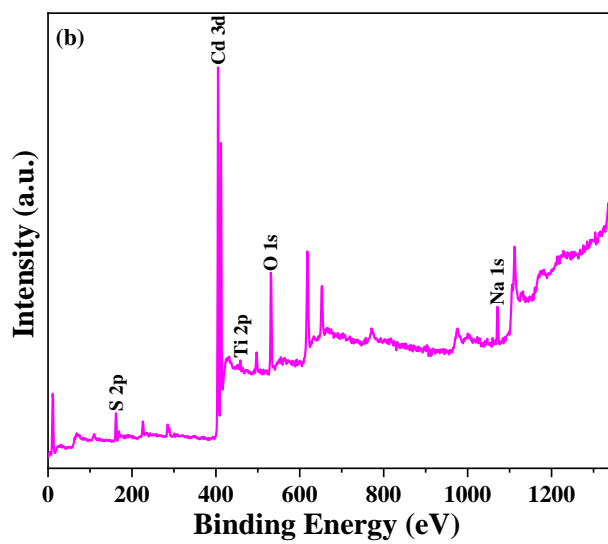
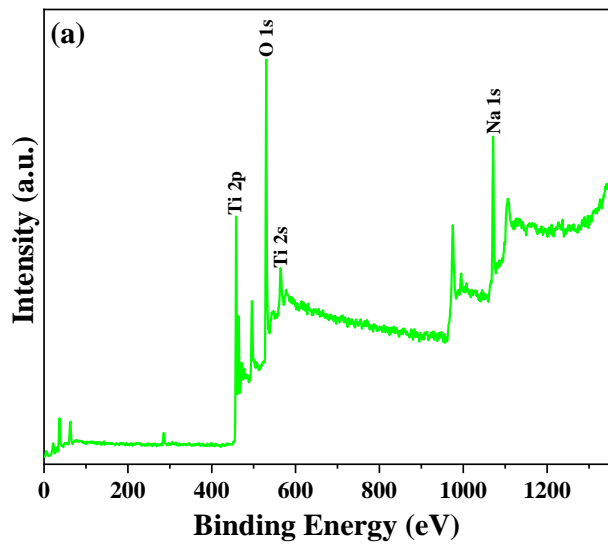
Raman scattering spectroscopy was performed to clarify the surface phases of as synthesized samples of NTO. The Raman spectroscopy of pristin NTO nanorods revealed six typical peaks at 195, 275, 443, 660, 709 and 905  $\text{cm}^{-1}$  (Fig. 1b). The Raman peaks at 195 $\text{cm}^{-1}$  has totally corresponded to Ti-O vibrations of anatase. Two other bands at about 275 and 443  $\text{cm}^{-1}$  can be attributed to the stretching of Na-O-Ti and vibrations of Ti-O-Ti, respectively. Two peaks located at 660 and 709  $\text{cm}^{-1}$  are assigned to stretching of Ti-O-Ti bands in edge-shared  $\text{TiO}_6$ . The Raman band at 905  $\text{cm}^{-1}$  is assigned to Na-O-Ti band [28-30].

The strong raman peaks located at around 299 and 599  $\text{cm}^{-1}$  of NTO/CdS12 in Fig. 1c can be attributed to first and second order longitudinal optical (LO) phonon modes of CdS, respectively. Moreover, two weak peaks at 195 and 905  $\text{cm}^{-1}$  correspond to NTO nanorods. Based on the above mentioned peaks, it can be proposed that both NTO nanorods and CdS nanoparticles were conserved in their crystal structures, and coexisted in the NTO/CdS12 heterostructured sample [29, 31].

### 3.3.1.3. XPS

XPS technique was employed to investigate the element composition on the surface of NTO and NTO/CdS12. Fig. 2 a & b show the XPS survey spectrum of NTO and NTO/CdS12, respectively. The pure NTO show three main peaks at 458.6, 531.6 and 1071 eV correspond to Ti 2p and O 1s and Na 1s, respectively [32]. Two extra peaks were found in the XPS spectrum survey of NTO/CdS12, as compared to the pure NTO, located at the binding energies 161.7 and 405.3 eV, which indicate S 2p and Cd 3d peaks (Fig. 2b) [33]. The above results confirm the existence of CdS on the surface of NTO nanorod in NTO/CdS12. Figure 2c shows the high-resolution XPS spectra of Cd 3d with two peaks of Cd 3d<sub>5/2</sub> and Cd 3d<sub>3/2</sub> positioned at the binding energies 405.3 and 412.1 eV, which are assigned to the metallic cadmium. The difference of 6.82 eV in their calculated binding energy indicates to the existence of cadmium with an oxidation state of Cd<sup>2+</sup> [34]. There is a hump-type peak in the high-resolution XPS spectra of S 2p shown in Fig. 2d, which can be divided into two separate peaks, located at binding energy of 161.7 and 162.9 eV, related to the oxidation states of S 2p<sub>3/2</sub> and S 2p<sub>1/2</sub>, respectively [35]. Two distinctive peaks centered at binding energies 458.6 and 464.1 eV in Fig. 2e are attributed to Ti 2p<sub>3/2</sub> and Ti 2p<sub>1/2</sub>, respectively. A typical peak at 531.6 eV can be observed in Fig. 2f, which is assigned to O 1s is related to lattice oxygen in NTO nanorods [36].

The valance band edge of NTO and CdS were calculated by using valance band XPS results. The valance band edges for pure NTO and CdS were estimated to be 2.85 and 1.6 eV, respectively (Figs. 2g and h).



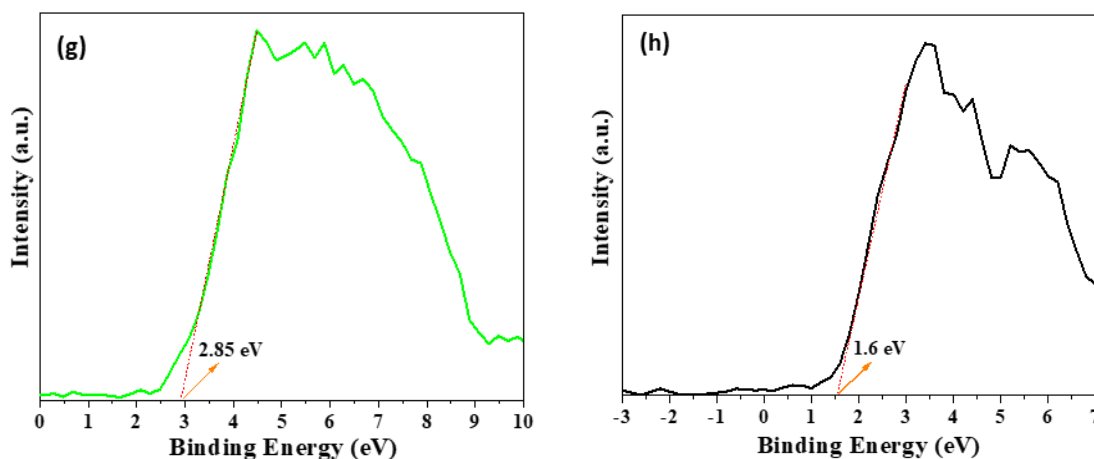


Figure 3. 2. XPS survey spectra of (a) NTO, (b) NTO/CdS12 and high-resolution XPS spectra of (c) Cd, (d) S, (e) Ti and (f) O, valance band edge for (g) pure NTO and (h) CdS

### 3.3.1.4. Optical absorption of samples by UV-Vis

Figure 3a illustrates the UV–vis diffuse reflection spectra of the as-prepared photoanodes. The optical absorption edge of NTO photoanode is 365 nm, which can be corresponded to the bandgap energy of 3.4 eV. Deposition of CdS as a semiconductor with a narrow band gap (about 2.3 eV) onto NTO can remarkably improve the absorption of visible light. All photoanode samples demonstrate the red shift of absorption edge and enhancement of their visible light absorption after the deposition of CdS with different SILAR cycles. The absorption edges of NTO/CdS7, NTO/CdS9, NTO/CdS12 and NTO/CdS15 are 551 nm, 544 nm, 546 nm and 558 nm, respectively, which show an absorption edge in visible light region, with much larger wavelengths, compared to pristine NTO photoanode. Increasing the number of SILAR cycles show an expansion in the absorption of visible light. The highest absorption enhancement of visible light region was obtained by NTO/CdS12 photoanode with 12 SILAR cycles.

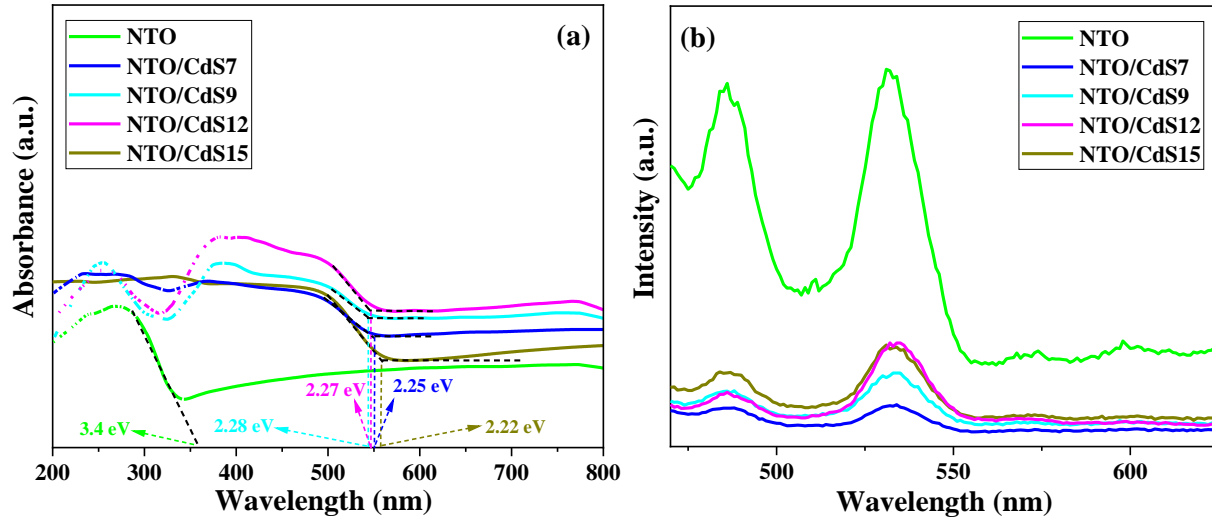


Figure 3. 3. (a) UV-Vis diffuse reflectance spectra and (b) PL spectra of NTO, NTO/CdS7, NTO/CdS9, NTO/CdS12, NTO/CdS15

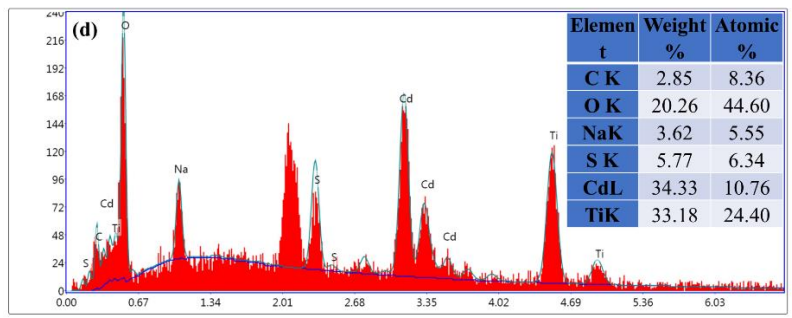
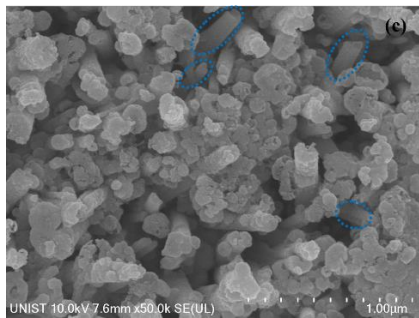
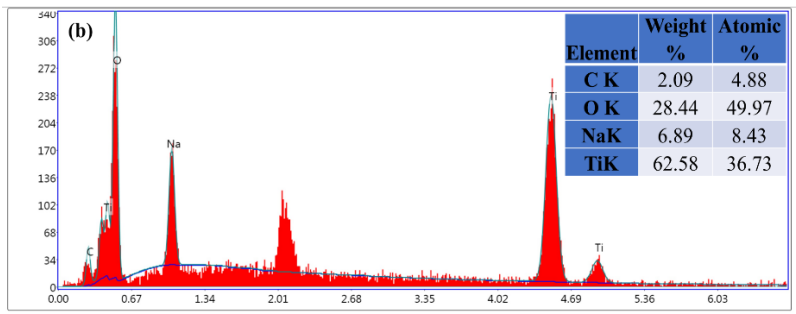
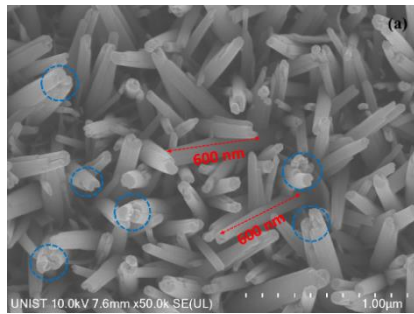
### 3.3.1.5. PL Spectra

PL spectra were carried out to investigate the recombination process of photogenerated carriers in the heterostructured photoanodes of NTO/CdS<sub>x</sub> (Fig. 3b). Two narrow emission peaks are observed in NTO at 480 and 530 nm which are attributed to the band edge recombination of electron-hole and deeply trapped emissions through the surface states, respectively [18, 26]. Deposition of CdS on NTO with different number of SILAR cycles caused to great reduction in the PL spectra peaks of all the samples compared to pure NTO, which indicates the effective improvement in separation of photogenerated electron-hole pairs by constructing the heterostructures.

### 3.3.1.6. SEM

Figure 4a displays the top view image of pure non-uniformed NTO nanorods that were grown densely and vertically or obliquely on the surface of Ti foil. The average diameter of nanorods ranged from 80 to 160 nm and their length reached up to 600nm. It can be seen that the top surface

of the as-synthesized nanorods contain many step edges, which are more favorable sites for adsorption of  $\text{Cd}^{2+}$  and  $\text{S}^{2-}$  ion for the growth of CdS, compared to side surface that is relatively smooth (Fig. 4a). Figures 4c, e, & g illustrate top view images of NTO/CdS9, NTO/CdS12 and NTO/CdS15. When the number of SILAR cycles deposition increases, a greater amount of CdS nanoparticles cover the surface of NTO nanorods. As shown in Fig. 4c, even after 9 cycles deposition, some parts of NTO were not fully covered with CdS nanoparticles. Deposition of nanorods with 12 SILAR cycles show that all the nanorod surfaces are uniformly and almost fully covered with CdS. However, further increasing the number of SILAR cycles to 15 caused the formation of an additional layer of CdS on the surface of NTO nanorods. The elemental composition of NTO/CdS with different SILAR cycles was investigated by EDX technique to detect the signals of cadmium and sulfide after deposition of CdS on the surface of NTO nanorods. Figures 4 d, f, & h clearly show that, the increase in the number of SILAR cycles from 9 to 15 leads to the increase in the weight percentage of cadmium and sulfide from 34.3 to 61.06 and 5.77 to 15.27 Wt.%, respectively.



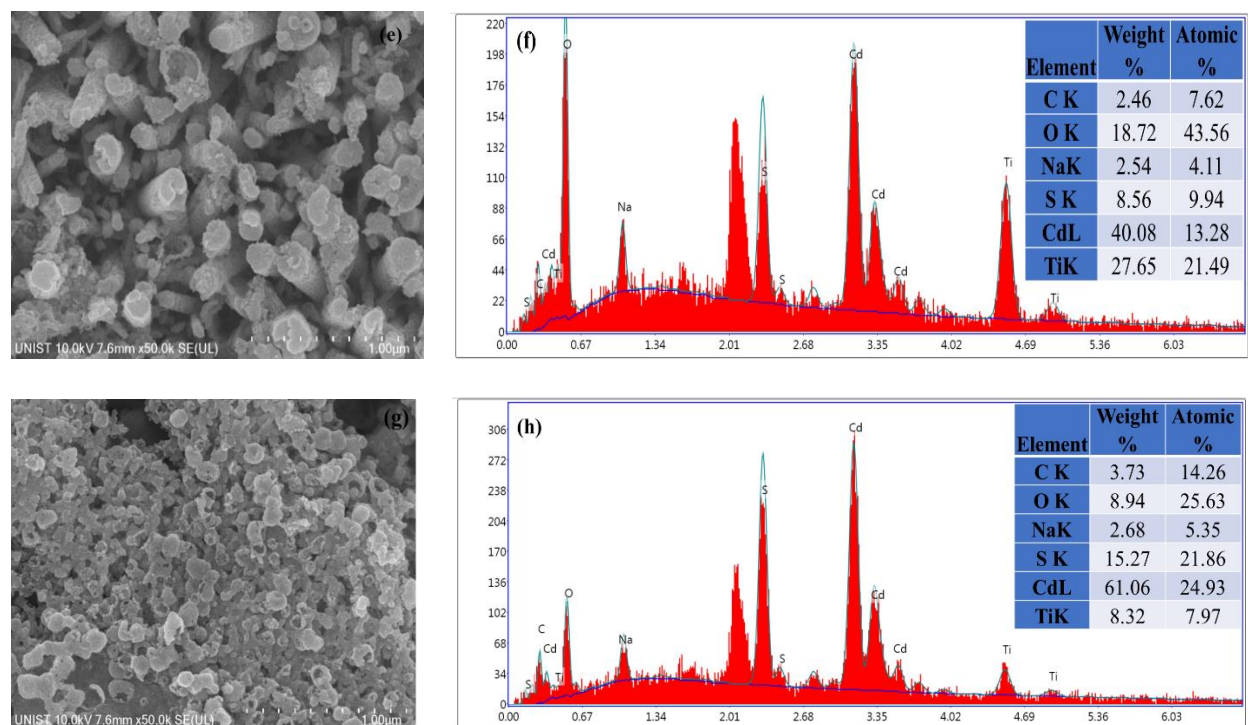


Figure 3. 4. SEM image of (a) NTO, (c) NTO/CdS9, (e) NTO/CdS12, (g) NTO/CdS15 and EDX analysis (b) NTO, (d) NTO/CdS9, (f) NTO/CdS12, (h) NTO/CdS15

### 3.3.1.7 TEM

Figure 5 shows the transmission electron microscopy (TEM), the high-resolution (HR) TEM imagery, selected area electron diffraction (SAED) pattern and elemental mapping of the pure NTO and the NTO/CdS12 photoanodes that were scratched away from the Ti foil substrate. Figure 5a shows the formation of sodium titanate nanorods on the surface of Ti foil under hydrothermal process, which is consistent with the SEM analysis. It can be seen that after 12 SILAR cycles deposition, the NTO nanorods were coated uniformly with CdS nanoparticles (Fig.5b). HRTEM imagery of the NTO/CdS12 photoelectrode in Fig. 5c exhibits the spacing of the lattice fringes of the CdS (110) plane and the sodium titanate (011) plane are 0.23 and 0.34 nm, respectively. The selected area electron diffraction (SAED) pattern in the inset of Fig. 5c, indicates the spot and ring patterns correspond to the single crystal structure of NTO NRs and polycrystalline structure of



CdS nanoparticles, respectively. A round diffraction ring corresponding to CdS (002) plane can be clearly observed which is consistent with the XRD pattern results. Furthermore, the elemental mapping images in Fig. 5d obviously show the NTO/CdS12 photoanode only contains of Na, Ti, O, Cd and S which indicate the purified synthesis of this sample.

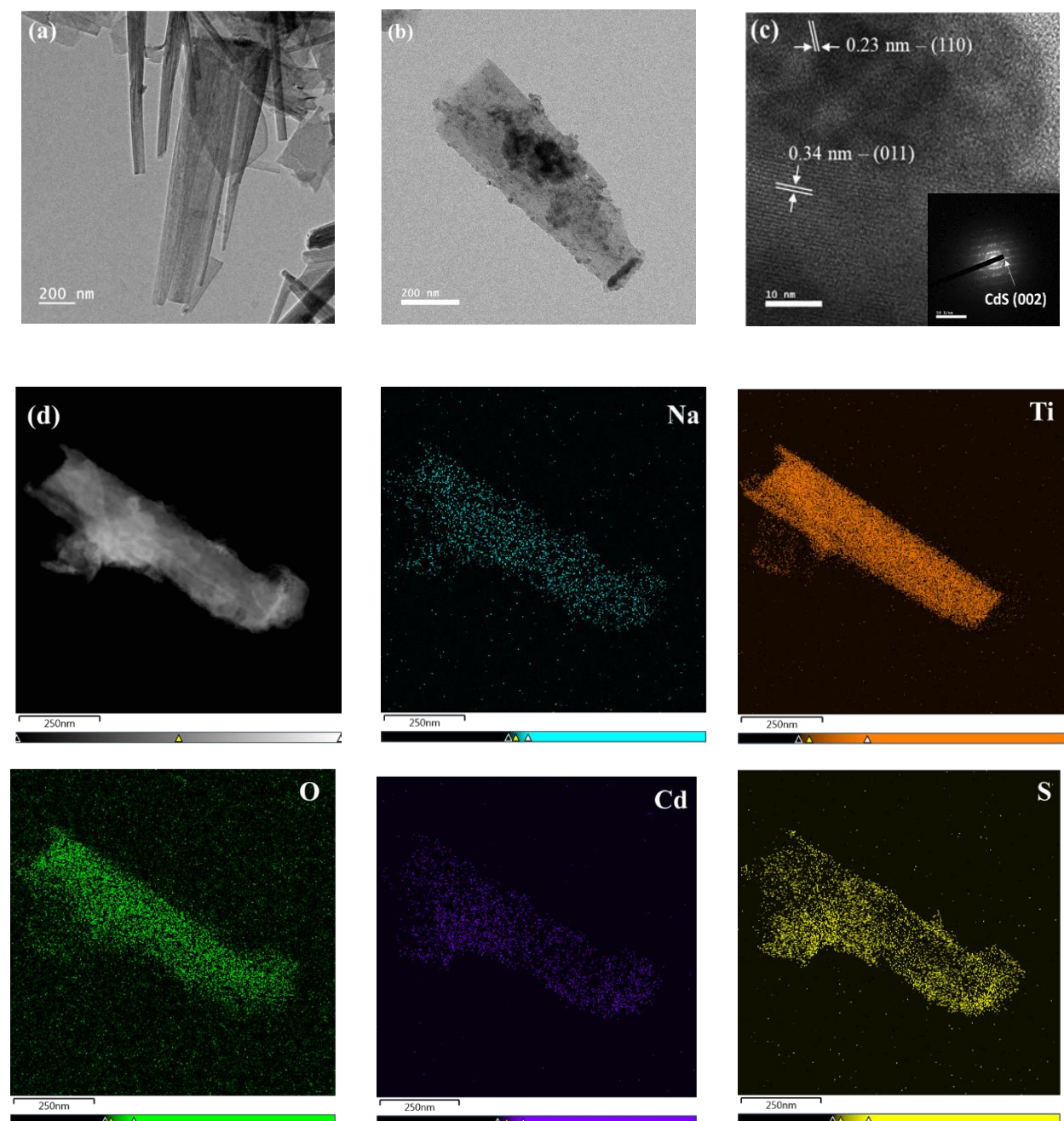




Figure 3. 5. TEM images of a) NTO and b) NTO/CdS12, c) HRTEM image of NTO/CdS12 and d) elemental mapping of NTO/CdS12 photoelectrode. The inset is the corresponding selected area electron diffraction (SAED) patterns of NTO/CdS12.

### 3.3.2. Photoelectrochemical (PEC) properties

Figure 6a represents linear sweep voltammetry (LSV) of NTO and NTO/CdS<sub>x</sub> photoelectrodes between -0.15 ~ 2 V vs. RHE in 0.5 M Na<sub>2</sub>SO<sub>3</sub> aqueous solution under continuous and chopped illumination with 100 mW.cm<sup>-2</sup> intensity. An insignificant amount of photocurrent was observed in the dark condition for all photoelectrodes. Pure NTO has a negligible photocurrent around 0.066 mA/cm<sup>2</sup> at 1 V vs. RHE. The photocurrent of different NTO/CdS<sub>x</sub> samples was greatly enhanced by increasing the number of SILAR cycles to 12 cycles. The photocurrent density of the NTO/CdS12 was 2.37 mA/cm<sup>2</sup> at 1 V vs. RHE, which is 36 times higher than that of the pure NTO. This outstanding improvement can be attributed to the large absorption of visible light from incident solar spectrum, due to both the narrow band gap energy of CdS, and the formation of type II heterojunction between CdS and NTO, which promote the generation and separation of charge carriers, leading to the excellent PEC performance. Further increasing in the number of SILAR cycles from 12 to 15 decreased the photocurrent density from 2.37 to 0.77 mA/cm<sup>2</sup> at 1 V vs. RHE. After deposition of 9 and 12 SILAR cycles, CdS nanoparticles only cover the surface of each nanorod individually. Further increasing the number of SILAR cycles to 15 caused the formation of an additional layer of CdS on the surface of NTO nanorods (Fig. 4g). Figure 3a shows all the NTO/CdS<sub>x</sub> samples have 2 different absorption edges corresponded to NTO and CdS except for the NTO/CdS15 affected by as-mentioned layer. This thick layer prevents illuminated light to reach the NTO nanorods which can suppress the formation of type II heterojunction between NTO and CdS for efficient electron-hole generation and separation in this sample. Consequently, this

layer decrease the photocurrent of the NTO/CdS15 compared to other photoelectrodes (NTO/CdS7, NTO/CdS9, NTO/CdS12) .

Figure 6a shows photocurrent density of all photoanode samples as a function of external bias voltage. The photoelectrodes with heterostructures between the NTO and the CdS nanoparticles having more than 7 SILAR cycles showed greatly improved photocurrent, even at lower external bias voltage (around 0.2 V vs. RHE), which is an interesting achievement in this heterostructured system. From chopped LSV curves, all the photoelectrodes showed current around zero in dark condition, indicating the current under light illumination was generated by the interplay of the light and photoanodes (Fig. 6b). Moreover, the quantitative value of photocurrent was identical with photocurrent density of LSV.

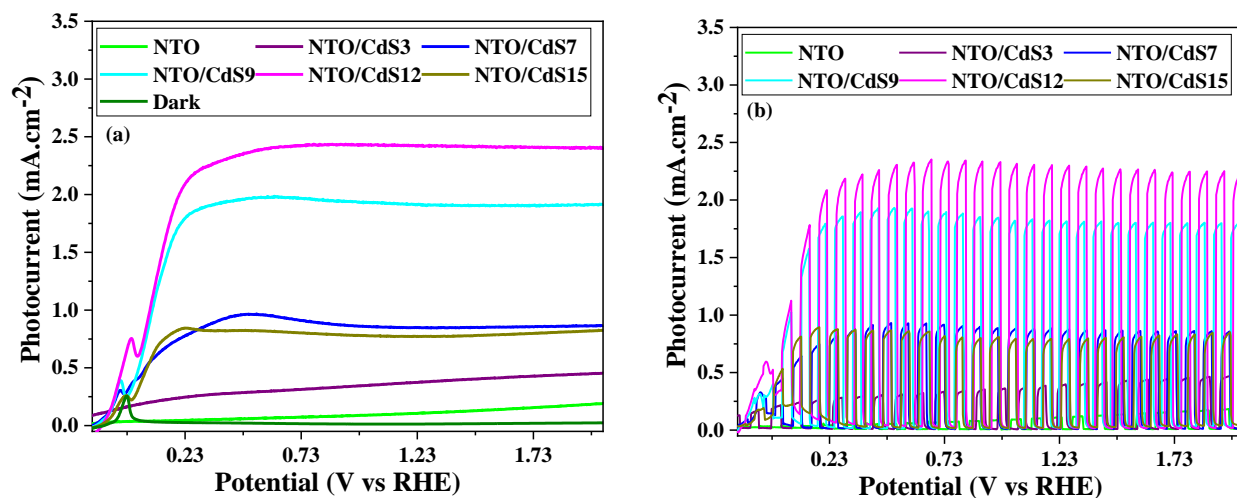


Figure 3. 6. Linear sweep voltammetry (LSV) of NTO and NTO/CdS<sub>x</sub> photoelectrodes under (a) continuous and (b) chopped illumination

Chronoamperometric analysis was conducted to investigate the photocurrent response and photocurrent stability of different NTO/CdS<sub>x</sub> photoanodes at 1 V vs. RHE (Fig. 7a). The fast response and recovery of photocurrent per each light on/off cycle demonstrates photogenerated electrons are quickly transferred through the composite layers and Ti substrate. The photocurrent density for all the photoanodes are followed the order: NTO/CdS12 > NTO/CdS9 > NTO/CdS7 >

NTO/CdS15 > NTO/CdS3 > NTO. The highest photocurrent density was obtained by NTO/CdS12 photoelectrode, which retained more than 95% of its initial photocurrent even under 20 min of light irradiation. Figure 7b illustrates the photocurrent stability of the NTO/CdS12 photoanode for 6,000 s.

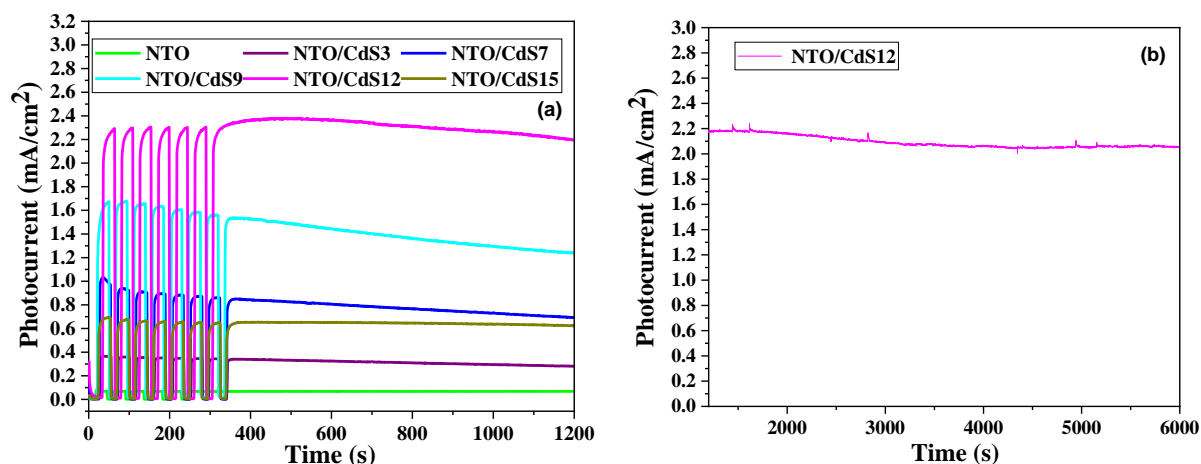


Figure 3. 7. (a) photocurrent response at the potential of 1 V vs. RHE, (b) long time photocurrent stability of NTO/CdS12 photoanode

The open circuit potential (OCP) of the NTO and NTO/CdS<sub>x</sub> electrodes were measured to evaluate the injection direction of photoinduced electrons under the light illumination. Figure 8a reveals that all the electrodes exhibit a negative increase in voltage under the light illumination, which means photoinduced electrons are transferring from semiconductor films into Ti foil substrate, leading to the generation of anodic photocurrent in chronoamperometry and LSV analysis. The negative enhancement for the voltage and positive photocurrent in different photoelectrochemical analyses confirm that the as-synthesized NTO and NTO/CdS<sub>x</sub> heterojunction samples act as an n-type semiconductor. Photogenerated voltage for NTO/CdS12 is much larger than that for the pure NTO. This indicates that NTO/CdS12 sample shows noticeable photoelectric conversion ability. As compared to pristine NTO for the NTO/CdS12 photoanode, it takes about 60 s longer to come

back to the dark equilibrium from illuminated states (around 120 s), suggesting that the heterojunction structure noticeably prolongs recombination process of the photoinduced charge carriers.

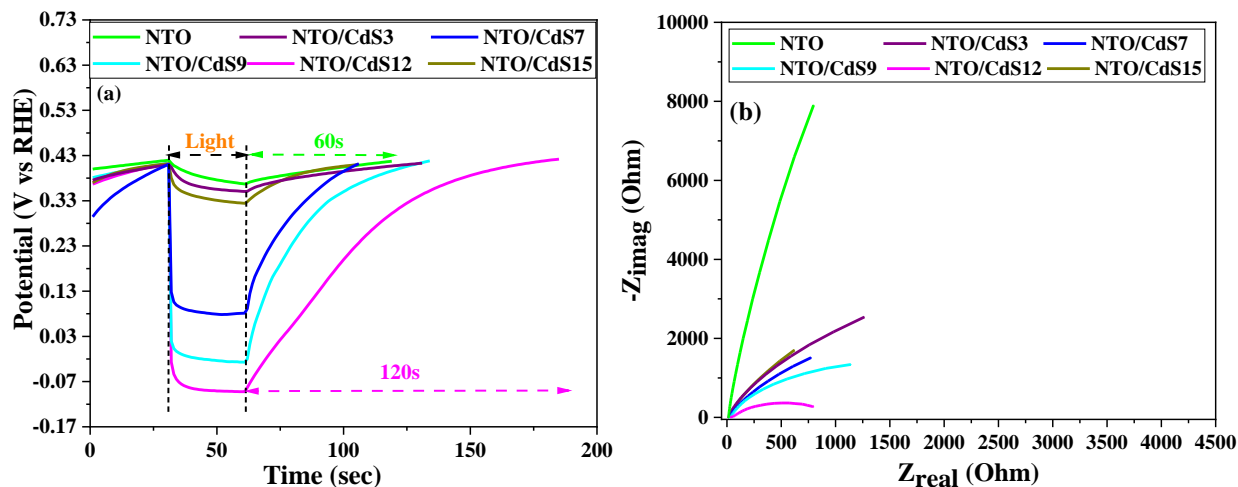


Figure3. 8. (a) Transient OCP and (b) EIS Nyquist plot of NTO and NTO/CdS<sub>x</sub> photoanodes

To investigate the the photogenerated charge transport ability of different photoanode, the electrochemical impedance spectroscopy (EIS) analysis was conducted from the frequency range of 0.1 Hz to 100 KHz under light illumination. There are two different resistances for the transference of charge carriers during electrochemical reaction in PEC cell, including the electrolyte resistance ( $R_s$ ) and the charge transfer resistance across photoanode and electrolyte solution ( $R_{ct}$ ). From Nyquist plot for different photoanodes shown in Fig. 8b, the NTO/CdS<sub>12</sub> has the smallest semicircle radius compred to the pure NTO and other NTO samples deposited by CdS with different SILAR cycles. The smaller radius demonstrates the lower  $R_{ct}$ , which can promote separation of photoinduced electron and hole pairs, and enhance interfacial charge transfer of hole from the photoanode to the electrolyte. Furthermore, the order of decrease in the radius of semicircle of the different photoelectrode samples is in consistant with their photoelectrochemical performance resultes.

Mott-Schottky analysis was also conducted to determine the carrier concentration ( $N_D$ ) and flat band potential ( $V_{fb}$ ) in all as-prepared photoanodes to further understand the improvement in PEC performance of samples after the deposition of CdS nanoparticles. Carrier concentration and flat band potential can be estimated by the slope and X-intercept of the linear region of Mott-Schottky curves with using the following equations:

$$\frac{1}{C^2} = \frac{2}{\epsilon\epsilon_0 A^2 e N_D} \left( V - V_{fb} - \frac{K_B T}{e} \right) \quad (1)$$

$$Slope = \frac{2}{\epsilon\epsilon_0 A^2 e N_D} \rightarrow N_D = \frac{2}{\epsilon\epsilon_0 A^2 e (Slope)} \quad (2)$$

$$intercept = V_{fb} + \frac{K_B T}{e} \rightarrow V_{fb} = intercept - \frac{K_B T}{e} \quad (3)$$

From Eq. (2), the improvement in carrier concentration is obtained by decrease in the slope of the curve. Figure 9 illustrates that after deposition of CdS, the slope of NTO in the linear region decreased significantly by increasing the number of SILAR cycles up to 12 cycles, indicating the highest donor concentration is achieved in NTO/CdS12 photoanode. Furthermore, loading of CdS nanoparticles decreased the flat band potential of NTO/CdS7 from 0.38 V to 0.27 V vs. RHE for NTO/CdS12 sample, which is attributed to the great reduction in the recombination of photogenerated electron and hole pairs. Table 1 shows the calculated amount of  $V_{fb}$  and  $N_D$  of all samples by using the Mott-Schottky equation.

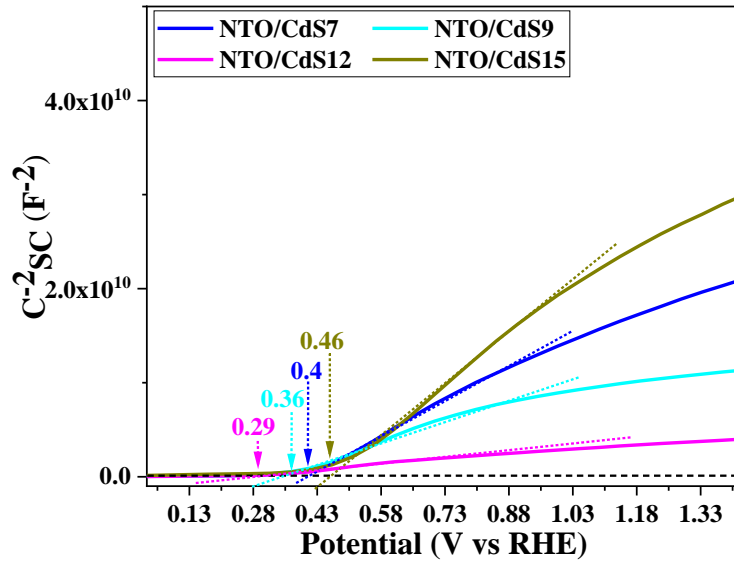


Figure3. 9. Mott–Schottky plot of NTO and NTO/CdSx photoanodes

Table 3. 1. Summarized  $V_{fb}$  and  $N_D$  values obtained from the intercept and the slope in Mott-Schottky plots

Samples	slope	intercept	$N_D$ ( $m^{-3}$ )	$V_{fb}$ (V)
NTO/CdS7	2.04E+10	0.4	3.11E+28	0.38
NTO/CdS9	1.43E+10	0.36	4.44E+28	0.34
NTO/CdS12	3.94E+09	0.29	1.61E+29	0.27
NTO/CdS15	3.14E+10	0.46	2.02E+28	0.44

The applied bias photon-to-current conversion efficiency (ABPE) for PEC activity for different photoanodes were estimated based on LSV data and following equation[37]:

$$ABPE\% = I \frac{(1.23 - V_{app})}{P_{light}} \quad (4)$$

where  $I$  is the measured photocurrent density at different applied potentials ( $V_{app}$ ), and  $P$  is the power density of the incident light. Figure 10a shows that for all the photoelectrode samples, after

the deposition of CdS with different SILAR cycles, the maximum ABPE increased. The photoconversion efficiency of the NTO/CdS12 photoanode is 1.1% at 0.65 V vs RHE which is 55 times larger than that of the pure NTO, which is around 0.02%.

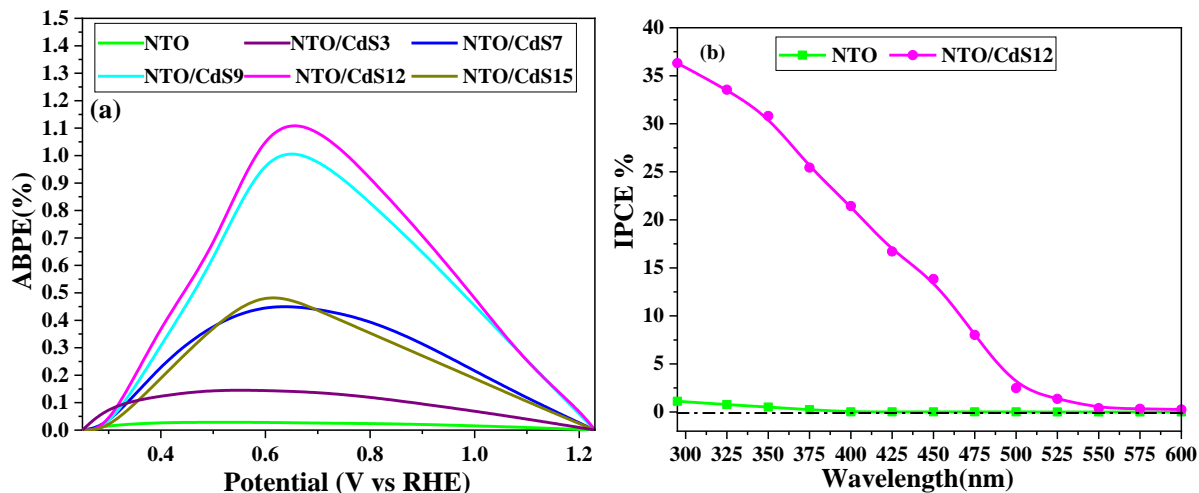


Figure 3. 10. (a) Photoconversion efficiency as a function of applied voltage vs RHE for NTO and NTO/CdSx photoanodes and (b) IPCE spectra of NTO and NTO/CdS12 photoanodes at 1 V vs. RHE.

The incident-photon-to-current-efficiencies (IPCE) analysis was also carried out for NTO and NTO/CdS12 photoanodes at a bias voltage of 1 V vs. RHE using 0.5 M aqueous solution of  $\text{Na}_2\text{SO}_3$ . The pure NTO exhibits only around 1% of IPCE value over the wavelength range 295 to 375 nm. At larger wavelength, the IPCE value of NTO reaches zero, because of its optical absorption edge. Deposition of CdS shows noticeable improvement in IPCE value of NTO/CdS12 due to enhancement in light capturing and formation of type II heterojunction between NTO and CdS nanoparticles, which lead to a better PEC activity for this photoanode. The IPCE value for NTO/CdS12 at 295 nm is around 36%, which is 36 times higher than that of the pure NTO. The IPCE of the NTO/CdS12 decreases to zero for the wavelength larger than 525 nm, which is consistent with UV visible DRS results (see Fig. 10b).

Fig. 11a and b show the generated amount of the hydrogen and oxygen as a function of the reaction time for pure NTO and the NTO/CdS12 (having optimum SILAR cycles) photoanodes. The total H<sub>2</sub> generated after 2h of irradiation for pure NTO and the NTO/CdS12 is 0.07 and 10.7 μmol.cm<sup>-2</sup>, respectively, and the total O<sub>2</sub> generated is 0.03 and 5.37 μmol.cm<sup>-2</sup>, respectively. These identified values supply clear evidence of the splitting of water into H<sub>2</sub> and O<sub>2</sub> gases.

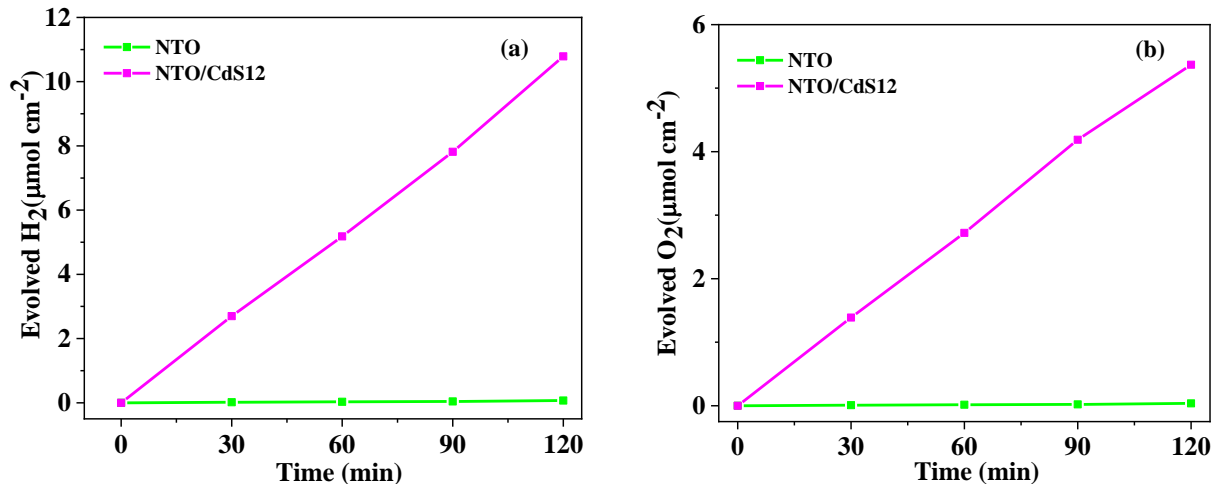


Figure 3. 11. (a) H<sub>2</sub> and (b) O<sub>2</sub> evolution vs. reaction time per illuminated area (1cm<sup>2</sup>) for NTO and the NTO/CdS12 electrodes at a potential of 1V (vs. RHE). Under 100 mW.cm<sup>-2</sup> irradiation, electrolyte was a 0.5M (PH=9) aqueous solution of Na<sub>2</sub>SO<sub>3</sub>.

### 3.3.3. Mechanism of PEC enhancement

Figure 12 shows a schematic of the energy band structure for NTO/CdS<sub>x</sub> photoanode, to show the possible transfer mechanism of charge carriers under light irradiation. The formation of type II heterojunction was formed in the NTO/CdS<sub>x</sub> system, because of the proper band edge and intimate contact between CdS nanoparticles and sodium titanate nanorods with multiple step edge. The sodium titanate and CdS are excited by UV and visible light irradiation, respectively, to produce electron-hole pairs. The potential of the conduction band (CB) of CdS nanoparticles in the NTO/CdS<sub>x</sub> photoanode (of -0.7 V) is slightly higher than the corresponding CB potential of



sodium titanate (of  $-0.55\text{V}$ ), which can cause the photogenerated electrons in CdS to transfer thermodynamically to the CB of sodium titanate nanorods. Also, due to the great contact between NTO nanorods and Ti substrate, these electrons can easily reach to the surface of Ti foil, and finally migrate to the Pt counter, to participate in hydrogen evolution reaction (HER). On the other hand, photogenerated holes in sodium titanate migrate to the VB of CdS nanoparticles to participate in the oxygen evolution reaction with electrolyte solution.

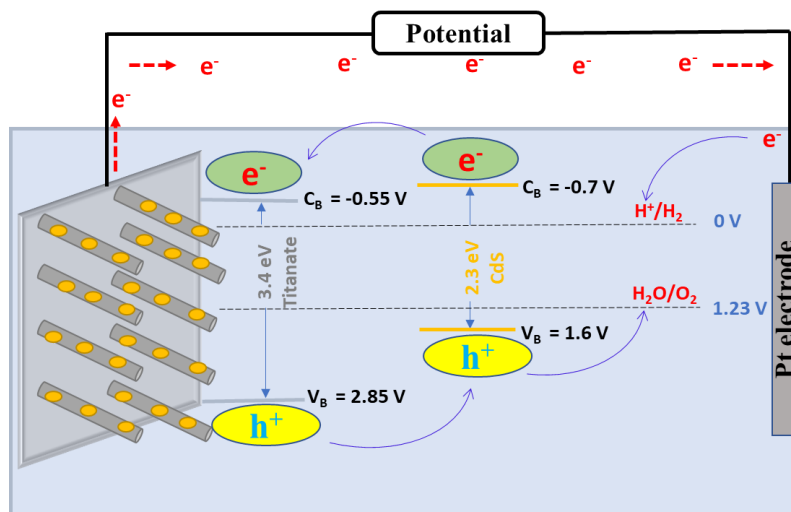


Figure 3. 12. Possible mechanism for enhanced PEC performance and photogenerated charge carrier transfer over NTO/CdSx electrodes.

### 3.4. Conclusion

Sodium titanate nanorods with multi-step edges were synthesized by one-step hydrothermal method on the surface of Ti foil as the substrate. NTOs with rough surfaces were confirmed as favorite places for deposition of CdS nanoparticles with suitable band alignment to efficiently extend the absorption edge of the NTO into visible light region. This study systematically investigated the effect of the number of SILAR cycles for deposition of CdS nanoparticles on the PEC performance of NTO/CdSx photoanodes. The NTO photoanode deposited with CdS

nanoparticles using 12 SILAR cycles (NTO/CdS12 heterostructure) showed highest PEC performance, compared to the pristine NTO and other NTO/CdS<sub>x</sub> photoanodes. The photocurrent density of the NTO/CdS12 photoanode was 2.37 mA/cm<sup>2</sup> at 1 V vs. RHE which was 36 times higher than that of the pure NTO photoanode. Moreover, The IPCE value for NTO/CdS12 at 295 nm was around 36% that is 36 times higher than that of pure NTO. The NTO/CdS12 photoelectrode retained more than 95% of its initial photocurrent, even after 6,000 s of light irradiation. The noticeable improvement in PEC performance of NTO/CdS<sub>x</sub> photoanodes and their great stability can be attributed to the type II heterojunction between CdS and NTO, which promotes the generation and separation of charge carrier. The great PEC performance and stability are also due to the outstanding connection between CdS nanoparticles and NTO nanorods with multi-stage edges and Ti substrate that facilitate the transfer of photogenerated electrons to the surface of Ti substrate.

## Reference:

- [1] L. Wang, W. Si, X. Hou, M. Wang, X. Liu, Y. Ye, F. Hou, J. Liang, Novel integrated strategies toward efficient and stable unassisted photoelectrochemical water splitting, *Sustainable Materials and Technologies* (2020) e00209.
- [2] Š. Kment, K. Sivula, A. Naldoni, S. Sarmah, H. Kmentová, M. Kulkarni, Y. Rambabu, P. Schmuki, R. Zbořil, FeO-based nanostructures and nanohybrids for photoelectrochemical water splitting, *Progress in Materials Science*, 110 (2020) 100632.
- [3] M. Shahrezaei, A.A. Babaluo, S. Habibzadeh, M. Haghighi, Photocatalytic Properties of 1D TiO<sub>2</sub> Nanostructures Prepared from Polyacrylamide Gel–TiO<sub>2</sub> Nanopowders by Hydrothermal Synthesis, *European Journal of Inorganic Chemistry*, 2017 (2017) 694-703.
- [4] M. Shahrezaei, S. Habibzadeh, A.A. Babaluo, H. Hosseinkhani, M. Haghighi, A. Hasanzadeh, R. Tahmasebpour, Study of synthesis parameters and photocatalytic activity of TiO<sub>2</sub> nanostructures, *Journal of Experimental Nanoscience*, 12 (2017) 45-61.
- [5] M. Tayebi, M. Kolaei, A. Tayyebi, Z. Masoumi, Z. Belbasi, B.-K. Lee, Reduced graphene oxide (RGO) on TiO<sub>2</sub> for an improved photoelectrochemical (PEC) and photocatalytic activity, *Solar Energy*, 190 (2019) 185-194.
- [6] H.S. Han, W. Park, S.W. Hwang, H. Kim, Y. Sim, S. Surendran, U. Sim, I.Cho, (0 2 0)-Textured tungsten trioxide nanostructure with enhanced photoelectrochemical activity, *Journal of catalysis*, 389 (2020) 328-336.
- [7] M. Tayebi, A. Tayyebi, B.-K. Lee, Improved photoelectrochemical performance of molybdenum (Mo)-doped monoclinic bismuth vanadate with increasing donor concentration, *Catalysis Today*, 328 (2019) 35-42.
- [8] M. Tayebi, A. Tayyebi, B.-K. Lee, C.H. Lee, D.H. Lim, The effect of silver doping on photoelectrochemical (PEC) properties of bismuth vanadate for hydrogen production, *Solar Energy Materials and Solar Cells*, 200 (2019) 109943.
- [9] Z. Masoumi, M. Tayebi, B.-K. Lee, The role of doping molybdenum (Mo) and back-front side illumination in enhancing the charge separation of  $\alpha$ -Fe<sub>2</sub>O<sub>3</sub> nanorod photoanode for solar water splitting, *Solar Energy*, 205 (2020) 126-134.
- [10] K. Alam, Y. Sim, J.-H. Yu, J. Gnanaprakasam, H. Choi, Y. Chae, U. Sim, H. Cho, In-situ deposition of graphene oxide catalyst for efficient photoelectrochemical hydrogen evolution reaction using atmospheric plasma, *Materials*, 13 (2020) 12.
- [11] E. Samuel, B. Joshi, M.-W. Kim, M.T. Swihart, S. Yoon, Morphology engineering of photoelectrodes for efficient photoelectrochemical water splitting, *Nano Energy*, (2020) 104648.
- [12] M. Shahrezaei, S.M.H. Hejazi, Y. Rambabu, M. Vavrecka, A. Bakandritsos, S. Oezkan, R. Zboril, P. Schmuki, A. Naldoni, S. Kment, Multi-Leg TiO<sub>2</sub> Nanotube Photoelectrodes Modified by Platinized Cyanographene with Enhanced Photoelectrochemical Performance, *Catalysts*, 10 (2020) 717.
- [13] R. Tahmasebpour, A.A. Babaluo, J.R. Shahrouzi, M. Tahmasebpour, M. Shahrezaei, Theoretical and experimental studies on the anodic oxidation process for synthesis of self-ordering TiO<sub>2</sub> nanotubes: Effect of TiO<sub>2</sub> nanotube lengths on photocatalytic activity, *Journal of environmental chemical engineering*, 5 (2017) 1227-1237.
- [14] M. Tayebi, B.-K. Lee, Recent advances in BiVO<sub>4</sub> semiconductor materials for hydrogen production using photoelectrochemical water splitting, *Renewable and Sustainable Energy Reviews*, 111 (2019) 332-343.
- [15] M. Tayebi, A. Tayyebi, T. Soltani, B.-K. Lee, pH-Dependent photocatalytic performance of modified bismuth vanadate by bismuth ferrite, *New Journal of Chemistry*, 43 (2019) 9106-9115.
- [16] Y. Sim, J. John, S. Surendran, B. Moon, U. Sim, Efficient photoelectrochemical water splitting reaction using electrodeposited Co<sub>3</sub>Se<sub>4</sub> catalyst, *Applied Science*, 9 (2019) 16.

- [17] Y.-C. Chang, J.-C. Lin, S. Wu, Compounds, One-step growth of Na<sub>2</sub>Ti<sub>3</sub>O<sub>7</sub> nanorods for enhanced photocatalytic activities and recyclability, *Journal of Alloys and Compounds*, 749 (2018) 955-960.
- [18] C. Liu, J.-y. Liang, R.-r. Han, Y.-z. Wang, J. Zhao, Q.-j. Huang, J. Chen, W. Hou, S-doped Na<sub>2</sub>Ti<sub>6</sub>O<sub>13</sub>@TiO<sub>2</sub> core-shell nanorods with enhanced visible light photocatalytic performance, *Physical Chemistry Chemical Physics*, 17 (2015) 15165-15172.
- [19] A. Abdal-hay, K. Gulati, T. Fernandez-Medina, M. Qian, S. Ivanovski, In situ hydrothermal transformation of titanium surface into lithium-doped continuous nanowire network towards augmented bioactivity, *Applies Surface Science*, 505 (2020) 144604.
- [20] M. Kolaei, M. Tayebi, B. Lee, The synergistic effects of acid treatment and silver (Ag) loading for substantial improvement of photoelectrochemical and photocatalytic activity of Na<sub>2</sub>Ti<sub>3</sub>O<sub>7</sub>/TiO<sub>2</sub> nanocomposite, *Applied Surface Science*, 540 (2021) 148359.
- [21] Y. Tang, L. Hong, Q. Wu, J. Li, G. Hou, H. Cao, L. Wu, G. Zheng, TiO<sub>2</sub> (B) nanowire arrays on Ti foil substrate as three-dimensional anode for lithium-ion batteries, *Electrochimica Acta*, 195 (2016) 27-33.
- [22] R. Wang, L. Wang, Y. Zhou, Z. Zou, Al-ZnO/CdS photoanode modified with a triple functions conformal TiO<sub>2</sub> film for enhanced photoelectrochemical efficiency and stability, *Applied Catalysis B: Environmental*, 255 (2019) 117738.
- [23] P. Pathak, S. Gupta, K. Grosulak, H. Imahori, V. Subramanian, Nature-inspired tree-like TiO<sub>2</sub> architecture: a 3D platform for the assembly of CdS and reduced graphene oxide for photoelectrochemical processes, *The Journal of Physical Chemistry*, 119 (2015) 7543-7553.
- [24] H.S. Han, W. Park, A. Sivanantham, S.W. Hwang, S. Surendran, U. Sim, I. Cho, Facile fabrication of nanotubular heterostructure for enhanced photoelectrochemical performance, *Ceramics International*, 47 (2021) 3972-3977.
- [25] X. Zhu, A. Anzai, A. Yamamoto, H. Yoshida, Silver-loaded sodium titanate photocatalysts for selective reduction of carbon dioxide to carbon monoxide with water, *Applied catalysis B: Environmental*, 243 (2019) 47-56.
- [26] L.K. Dhandole, H.-S. Bae, H.-S. Chung, W.-S. Chae, M. Cho, J. Jang, E.C. Research, Dual CdS Nanoparticle-Deposited Vertically Aligned Titanate Nanotube Heterostructure Photoanode, *Industrial & Engineering Chemistry Research*, 59 (2020) 9488-9499.
- [27] B.S. Rao, B.R. Kumar, V.R. Reddy, T.S. Rao, G. Chalapathi, Preparation and characterization of CdS nanoparticles by chemical co-precipitation technique, *Chalcogenide letters*, 8 (2011) 177-185.
- [28] T. Gao, H. Fjellvåg, P. Norby, Crystal structures of titanate nanotubes: a Raman scattering study, *Inorganic Chemistry*, 48 (2009) 1423-1432.
- [29] J. Song, D. Zeng, Y. Xie, F. Zhang, S. Rao, F. Wang, J. Zhao, J. Zhang, L. Wang, Preparation of CdS Nanoparticles-TiO<sub>2</sub> Nanorod Heterojunction and Their High-Performance Photocatalytic Activity, *Catalysts*, 10 (2020) 441.
- [30] D. Chaudhary, N. Khare, V. Vankar, Ag nanoparticles loaded TiO<sub>2</sub>/MWCNT ternary nanocomposite: a visible-light-driven photocatalyst with enhanced photocatalytic performance and stability, *Ceramics International*, 42 (2016) 15861-15867.
- [31] A.G. Milekhin, L. Sveshnikova, T. Duda, N. Surovtsev, S. Adichtchev, D. Zahn, Surface enhanced Raman scattering by CdS quantum dots, 88 (2008) 799-801.
- [32] S. Wang, Y. Zhu, M. Jiang, J. Cui, Y. Zhang, W. He, Interconnected Na<sub>2</sub>Ti<sub>3</sub>O<sub>7</sub> nanotube/g-C<sub>3</sub>N<sub>4</sub>/graphene network as high performance anode materials for sodium storage, *International Journal of Hydrogen Energy*, (2020).
- [33] H. Li, X. Wang, X. Li, J. Xi, Z. Ji, Compounds, The promising photoanode of Pt coupled TiO<sub>2</sub> NFs/CdS QDs with enhanced photoelectrochemical performance, *Journal of Alloys and compounds*, 790 (2019) 900-908.

- [34] G. Yang, B. Yang, T. Xiao, Z. Yan, One-step solvothermal synthesis of hierarchically porous nanostructured CdS/TiO<sub>2</sub> heterojunction with higher visible light photocatalytic activity, *Applied Surface Science*, 283 (2013) 402-410.
- [35] S. Peng, P. Zhu, V. Thavasi, S.G. Mhaisalkar, S. Ramakrishna, Facile solution deposition of ZnIn<sub>2</sub>S<sub>4</sub> nanosheet films on FTO substrates for photoelectric application, *Nanoscale*, 3 (2011) 2602-2608.
- [36] Z. Chen, Y. Xu, interfaces, Ultrathin TiO<sub>2</sub> layer coated-CdS spheres core-shell nanocomposite with enhanced visible-light photoactivity, *Applied Materials and Interface*, 5 (2013) 13353-13363.
- [37] M. Tayebi, B.K. Lee, The effects of W/Mo-co-doped BiVO<sub>4</sub> photoanodes for improving photoelectrochemical water splitting performance, *Catalysis Today*, (2020).

## **Chapter 4: The effect of NaOH concentration on growth of sodium titanate nanoflower on TiO<sub>2</sub> thin film**

### **Abstract**

This study reports the effect of the Ti source (Ti foil or TiO<sub>2</sub> thin layer) and NaOH concentration on the growth of sodium titanate nanostructures via hydrothermal treatment to improve the photoelectrochemical (PEC) water splitting performance. An optimal condition to grow sodium titanate nanoflower composed of ultrathin nanosheets on the surface of the thin TiO<sub>2</sub> film led to the formation of a novel nanocomposite TiO<sub>2</sub>/Na<sub>2</sub>Ti<sub>3</sub>O<sub>7</sub> photoelectrode with great adhesion of the two phases. The Ti/TiO<sub>2</sub>/Na<sub>2</sub>Ti<sub>3</sub>O<sub>7</sub> photoanode demonstrated a significant enhancement in photocurrent density and shifted the onset potential to a more negative value compared to the pure Ti/TiO<sub>2</sub> and Ti/Na<sub>2</sub>Ti<sub>3</sub>O<sub>7</sub> samples. This noticeable improvement is attributed to the suitable band alignment between the TiO<sub>2</sub> and Na<sub>2</sub>Ti<sub>3</sub>O<sub>7</sub> phases and their direct contact with the Ti foil, as well as the large surface area of nanoflower sodium titanate, which significantly facilitate the generation, separation, and transfer of photogenerated electrons from the active phases to the substrate. More interestingly, the prepared photoanode retained its initial photocurrent density even after 16 h. An ion-exchange method and calcination treatment were used at different temperatures to convert the Na<sub>2</sub>Ti<sub>3</sub>O<sub>7</sub> phase in the Ti/TiO<sub>2</sub>/Na<sub>2</sub>Ti<sub>3</sub>O<sub>7</sub> photoanode to TiO<sub>2</sub> to investigate the role of type II heterojunction for efficient photogenerated charge carrier separation in this photoanode. It was concluded that converting Na<sub>2</sub>Ti<sub>3</sub>O<sub>7</sub> into TiO<sub>2</sub> in the Ti/TiO<sub>2</sub>/Na<sub>2</sub>Ti<sub>3</sub>O<sub>7</sub> system would reduce its PEC performance due to the formation of a pure phase of TiO<sub>2</sub> in the Ti/TiO<sub>2</sub>/TiO<sub>2</sub> photoanode.

**Keywords:** Photoelectrochemical (PEC), sodium titanate nanorod, TiO<sub>2</sub> seed layer, Ti/TiO<sub>2</sub>/Na<sub>2</sub>Ti<sub>3</sub>O<sub>7</sub> photoanode

## 4.1. Introduction

Population growth and industrialization have generated two major problems in recent decades: energy shortage and environmental pollution. The combustion of fossil fuels for energy generation has released a large amount of CO<sub>2</sub> and other greenhouse gases into the atmosphere, resulting in serious environmental issues such as global warming and climate change. Hydrogen, considered the cleanest solar chemical fuel without carbon emissions during its oxidation in a fuel cell, can solve environmental problems [1-6]. Photoelectrochemical (PEC) water splitting using semiconductors as a photoelectrode has received significant attention because it can utilize solar energy to clean hydrogen production [7-14].

Recently layered titanates as a TiO<sub>2</sub> based materials have attracted considerable attention due to their high chemical inertness, lack of toxicity, ion exchangeability, and low cost[15, 16]. Furthermore, layered titanates can be accessible in various structures such as nanowires, nanobelts, nanosheets, and nanotubes with high surface areas [17]. More interestingly, they can be converted into the TiO<sub>2</sub> phase while maintaining their original structure [18]. Sodium titanate (Na<sub>2</sub>Ti<sub>3</sub>O<sub>7</sub>:NTO) as a layered titanate has a proper band edge position for both the water oxidation and the hydrogen reduction reaction, which can be used as a suitable semiconductor for the PEC water splitting process [19]. However, its wide energy bandgap of around 3.4 eV is a serious drawback for efficient water splitting activity. In addition, a drawback of sodium titanate in powder form, having aggregation and separation of powder from the substrate, needs to be resolved. Consequently, developing a facile and green method to grow a thin sodium titanate film on the substrate is vital to improve its PEC performance[17, 18].

There have been two different approaches for growing sodium titanate directly on the surface of Ti foil to significantly improve these issues. The first implies hydrothermal treatment of Ti foil with low NaOH concentration leading to the formation of a pure titanate phase [21]. The second approach involves the hydrothermal treatment of the thin TiO<sub>2</sub> film as a Ti source that requires a high concentration of NaOH solution [19]. The amount of conversion of titania to titanate phase in the second approach can be controlled by adjusting the concentration of the NaOH solution.

Oxidizing Ti foil in the air atmosphere at a relatively low temperature (around 500°C) is a simple method for the preparation of a thin TiO<sub>2</sub> film on the surface of Ti foil that has more photocatalytic activity compared to pure NTO due to the higher crystallinity and smaller bandgap energy (around 3 eV)[20, 21]. However, the synthesis of the TiO<sub>2</sub> film by this method results in the formation of some defects on the surface of TiO<sub>2</sub>. Defect sites can act as recombination centers, decreasing the photocatalytic activity of semiconductors[20, 22]. The nucleation of Na<sub>2</sub>Ti<sub>3</sub>O<sub>7</sub> most likely occurred at the defect sites on the thin layer of TiO<sub>2</sub> during the hydrothermal reaction and can lead to a significant reduction in the number of defect sites [25]. Optimizing NaOH concentration in the second approach to sodium titanate preparation leads to the formation of a new TiO<sub>2</sub>/Na<sub>2</sub>Ti<sub>3</sub>O<sub>7</sub> photoanode that has both titania photocatalytic activity and a large surface area of sodium titanate with nanoflower morphology. Furthermore, a suitable alignment of the band edge between TiO<sub>2</sub> and Na<sub>2</sub>Ti<sub>3</sub>O<sub>7</sub> and their direct contacts with the Ti foil significantly facilitate the separation and transfer of photogenerated electrons from the active phases to the substrate. Consequently, the Ti/TiO<sub>2</sub>/Na<sub>2</sub>Ti<sub>3</sub>O<sub>7</sub> photoanode exhibited a considerable improvement in PEC performance compared to the Ti/TiO<sub>2</sub> (pure titania phase), Ti/Na<sub>2</sub>Ti<sub>3</sub>O<sub>7</sub> (pure titanate phase) and FTO/Na<sub>2</sub>Ti<sub>3</sub>O<sub>7</sub> (powder form) photoanodes in previous studies[18, 23].



In this study, the new Ti/TiO<sub>2</sub>/Na<sub>2</sub>Ti<sub>3</sub>O<sub>7</sub> photoanode, prepared by an in situ synthesis method, with heterojunction structure and direct contact with the substrate, could solve all the mentioned problems, including separation of Na<sub>2</sub>Ti<sub>3</sub>O<sub>7</sub> from the substrate in powder form, presence of defect sites on the thin film TiO<sub>2</sub> and low PEC activity of Na<sub>2</sub>Ti<sub>3</sub>O<sub>7</sub>. Two processes, including thermal oxidation and alkaline hydrothermal treatment on Ti foil, were employed to prepare the samples. The effects of time oxidation, NaOH concentration, and choosing Ti foil or TiO<sub>2</sub> thin film as a Ti source to grow Na<sub>2</sub>Ti<sub>3</sub>O<sub>7</sub> in hydrothermal treatment were investigated. Furthermore, an ion-exchange method and calcination treatment were applied at different temperatures to convert the Na<sub>2</sub>Ti<sub>3</sub>O<sub>7</sub> phase in the Ti/TiO/Na<sub>2</sub>Ti<sub>3</sub>O<sub>7</sub> photoanode to TiO<sub>2</sub> to analyze the effect of both phase transition and morphological changes on the PEC performance of the original photoanode. Finally, this study discussed the effect of electrolyte pH on PEC performance.

## **4.2. Experimental procedure**

### **4.2.1. Preparation of Photoelectrodes**

#### **4.2.1.1. Fabrication of TiO<sub>2</sub> thin film**

We used high purity of titanium foils (99.9%) and the thickness of the foils is 0.127mm. The titanium foils (1x2 cm) were cleaned in a solution of distilled water, methanol, and acetone and dried in an oven at 80°C. Dried Ti foils were used as a substrate to prepare a thin TiO<sub>2</sub> film by oxidation in the air furnace at 500°C for 1,3, and 6 h with a ramp rate of 5 °C/min. These samples were named 500°C-1h, 500°C-3h, and 500°C-6h based on their different calcination times.

#### **4.2.1.2. Fabrication of Na<sub>2</sub>Ti<sub>3</sub>O<sub>7</sub> and TiO<sub>2</sub>/ Na<sub>2</sub>Ti<sub>3</sub>O<sub>7</sub> nanocomposite**

An alkali hydrothermal treatment was performed to grow sodium titanate on the surface of a thin TiO<sub>2</sub> film. To do this, 500°C-6h sample was placed in a 50 ml Teflon-lined stainless-steel autoclave

containing 20 ml of NaOH aqueous solution with 0.25, 2 and 4 M for 20 h at 200°C. These samples were denoted 500°C-6h+H0.25M, 500°C-6h+H2M and 500°C-6h+H4M according to the different concentrations of NaOH, respectively. A pure Ti foil as substrate was employed to grow the sodium titanate via the hydrothermal treatment in 0.25 M NaOH solution for 20h at 200°C, indicated as Ti+H0.25M.

#### **4.2.1.3. Replacement of Na<sup>+</sup> with H<sup>+</sup> and calcination in TiO<sub>2</sub> / Na<sub>2</sub>Ti<sub>3</sub>O<sub>7</sub> nanocomposite**

The as-prepared, 500°C-6h+H2M photoanode was vertically immersed in 100 ml of the aqueous solution of 0.1 M HCl and stirred for 5 h to replace Na<sup>+</sup> in the Na<sub>2</sub>Ti<sub>3</sub>O<sub>7</sub> phase with H<sup>+</sup> in the TiO<sub>2</sub> / Na<sub>2</sub>Ti<sub>3</sub>O<sub>7</sub> nanocomposite. Calcination at higher temperatures brought about the decomposition of the H<sub>2</sub>Ti<sub>3</sub>O<sub>7</sub> structure by converting to the TiO<sub>2</sub> phase by losing hydrate. After acid treatment, samples were transferred to an air furnace for calcination of them at different temperatures (500°C, 600°C and 700°C) for 2 h denoted as 500°C-6h+H2M+500°C, 500°C-6h+H2M+600°C and 500°C-6h+H2M+700°C, respectively.

#### **4.2.2. PEC measurement**

The PEC performance of the different photoelectrodes was carried out in a single-component three-electrode system cell with as-prepared photoelectrodes as working electrode, Pt wire as the counter electrode, and the saturated Ag/AgCl electrode as a reference electrode. The maximum electrolyte volume is 50 ml, and all electrodes are at an equal distance (1.5 cm). The reference electrode is placed closer to the measured sample to limit the effect of the resistance of the electrolyte. All measurements were made in a 0.5 M Na<sub>2</sub>SO<sub>3</sub> electrolyte solution at pH=10. PEC measurements were carried out under illumination of a 300 W Xe lamp calibrated at 100 mW/cm<sup>2</sup> from the front side in the scan range from -1 to 1.5 V (versus Ag / AgCl).

## 4.3. Results and discussion

### 4.3.1. Characterization results

#### 4.3.1.1. XRD

Figure 1 shows the X-ray diffraction patterns of Ti foil and TiO<sub>2</sub> thin layer treated in a hydrothermal process with different concentrations of NaOH aqueous solution. Ti+H0.25M exhibits seven diffraction peaks at  $2\theta = 9^\circ, 10.0^\circ, 24.1^\circ, 28.4^\circ, 29.3^\circ, 48.1^\circ$  and  $49.3^\circ$ , which can be indexed to the single-phase monoclinic sodium titanate with additional peaks at  $2\theta = 35.2^\circ, 38.4^\circ$  and  $40.2^\circ$  indicated to the Ti substrate[23-26]. The sample 500°C-6h shows four peaks located at  $2\theta = 27.4^\circ, 41.2^\circ, 44^\circ$  and  $54.4^\circ$ , corresponding to the existence of pure TiO<sub>2</sub> phase in this sample[27-29]. Two peaks at  $2\theta = 41.2^\circ$  and  $54.4^\circ$  are related to the presence of anatase structure, and two other peaks located at  $27.4^\circ$  and  $44^\circ$  are attributed to the rutile and brookite phases, respectively. However, the profile of the 500°C-6h+H0.25M had no additional peaks, which is attributed to the lack of sodium titanate formation or a negligible amount of that during hydrothermal reaction in NaOH with 0.25M concentration. 500°C-6h+H2M obtained by increasing the NaOH concentration to 2M shows disappearance of the XRD peak at  $44^\circ$  and appearance of two new peaks at  $2\theta = 9^\circ$  and  $47.8^\circ$ , confirming the coexistence of titania and sodium titanate phases [29]. A further increase in NaOH concentration to 4M caused the transformation of most of the thin layer of TiO<sub>2</sub> into a titanate phase. The XRD patterns of the 500°C-6h+H4M demonstrates six peaks at  $9.17^\circ, 24.3^\circ, 28.1^\circ, 43.8^\circ, 47.8^\circ$  and  $61.9^\circ$ . Except for the peak at  $43.8^\circ$ , all confirm titanate formation in the dominant phase of the photoelectrode[24, 25].

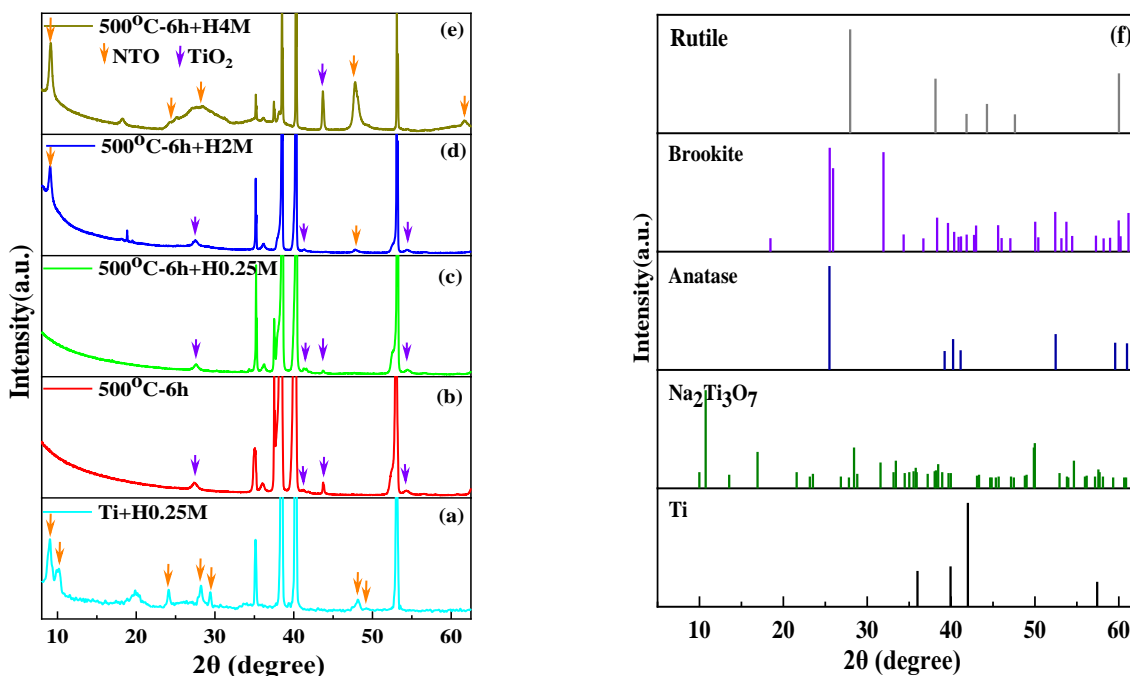


Figure 4. 1. XRD patterns of (a) Ti+H0.25M, (b) 500oC-6h, (c) 500oC-6h+H0.25M, (d) 500oC-6h+H2M and (e) 500oC-6h+H4M (f) JCPDS Card.no of TiO<sub>2</sub> Anatase (JCPDS Card no.21-1272), TiO<sub>2</sub> Rutile (JCPDS Card no.21-1276), TiO<sub>2</sub> Brookite (JCPDS Card no.29-1360), Sodium titanate (JCPDS Card no.31-1329) and Ti (JCPDS Card no.65-3362)

#### 4.3.1.2. Optical absorption by UV-Vis

Figure 2a shows the optical properties of Ti foil and TiO<sub>2</sub> thin film after hydrothermal treatment with different concentrations of NaOH aqueous solution. The 500°C-6h sample exhibits a light absorption peak near 400 nm, marked by a circle in Fig. 2b. This phenomenon may be related to the defects in the TiO<sub>2</sub> film during long-term heat treatment at 500°C. Nucleation of unstable sodium titanate is likely to occur in defects in the thin film of TiO<sub>2</sub>, along with the gradual growth and the formation of the titanate nanostructure [25]. Hydrothermal treatment of the TiO<sub>2</sub> thin film with a relatively low concentration of NaOH exhibits a negligible reduction in absorption peak related to these defects. When the NaOH concentration increases from 0.25M to 2M, most part of the aforementioned peak disappears during hydrothermal treatment. This process is related to the transformation of defects in the thin TiO<sub>2</sub> film to the sodium titanate phase that corresponds to the

presence of both the titania and sodium titanate phases in the 500°C-6h+H2M photoanode. When NaOH concentration increases from 2M to 4M, the UV-Vis spectra of the 500°C-6h+H4M shows a tendency of becoming like the Ti+H0.25M sample corresponds to the formation of dominant sodium titanate phase in the 500°C-6h+H4M photoanode.

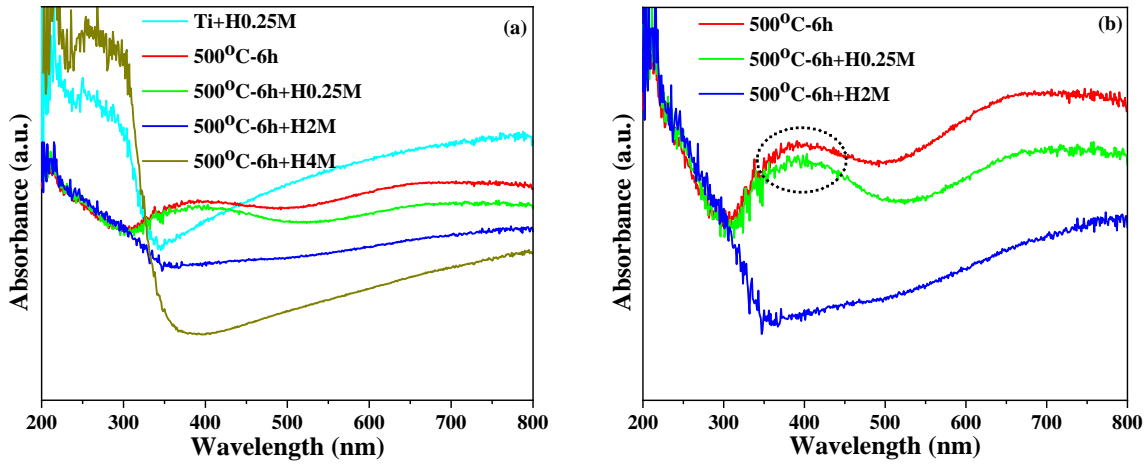


Figure 4. 2 UV-Vis diffuse reflectance spectra of (a) Ti+H0.25M, 500°C-6h, 500°C-6h+H0.25M, 500°C-6h+H2M and 500°C-6h+H4M (b) High resolution UV-Vis diffuse reflectance spectra of 500°C-6h, 500°C-6h+H0.25M and 500°C-6h+H2M samples

Figures 3a and b demonstrate the optical bandgap 3.4 and 3.0 eV of the pure sodium titanate (Ti+H0.25M) and TiO<sub>2</sub> thin film (500°C-6h), respectively calculated by Tauc equation from DRS data.

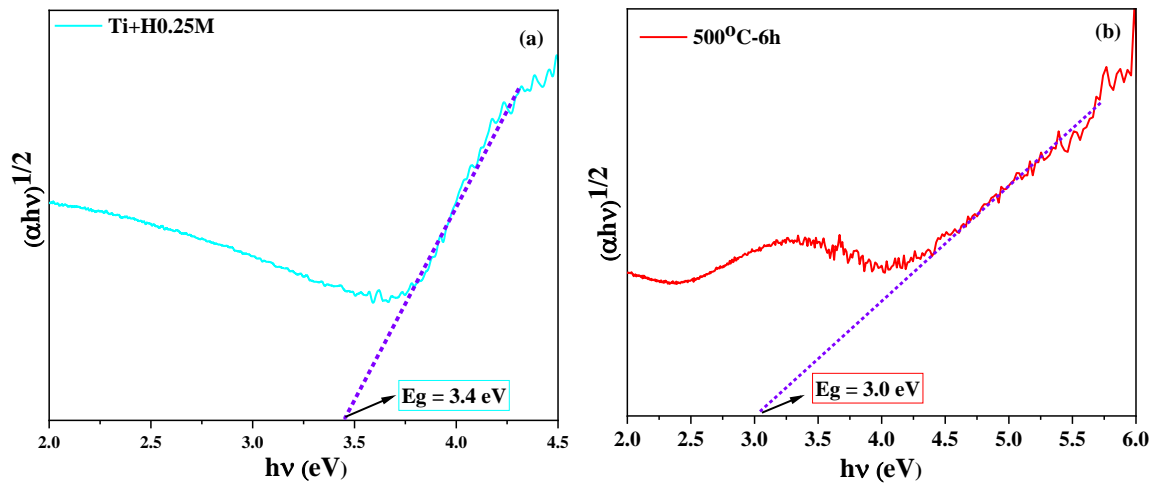
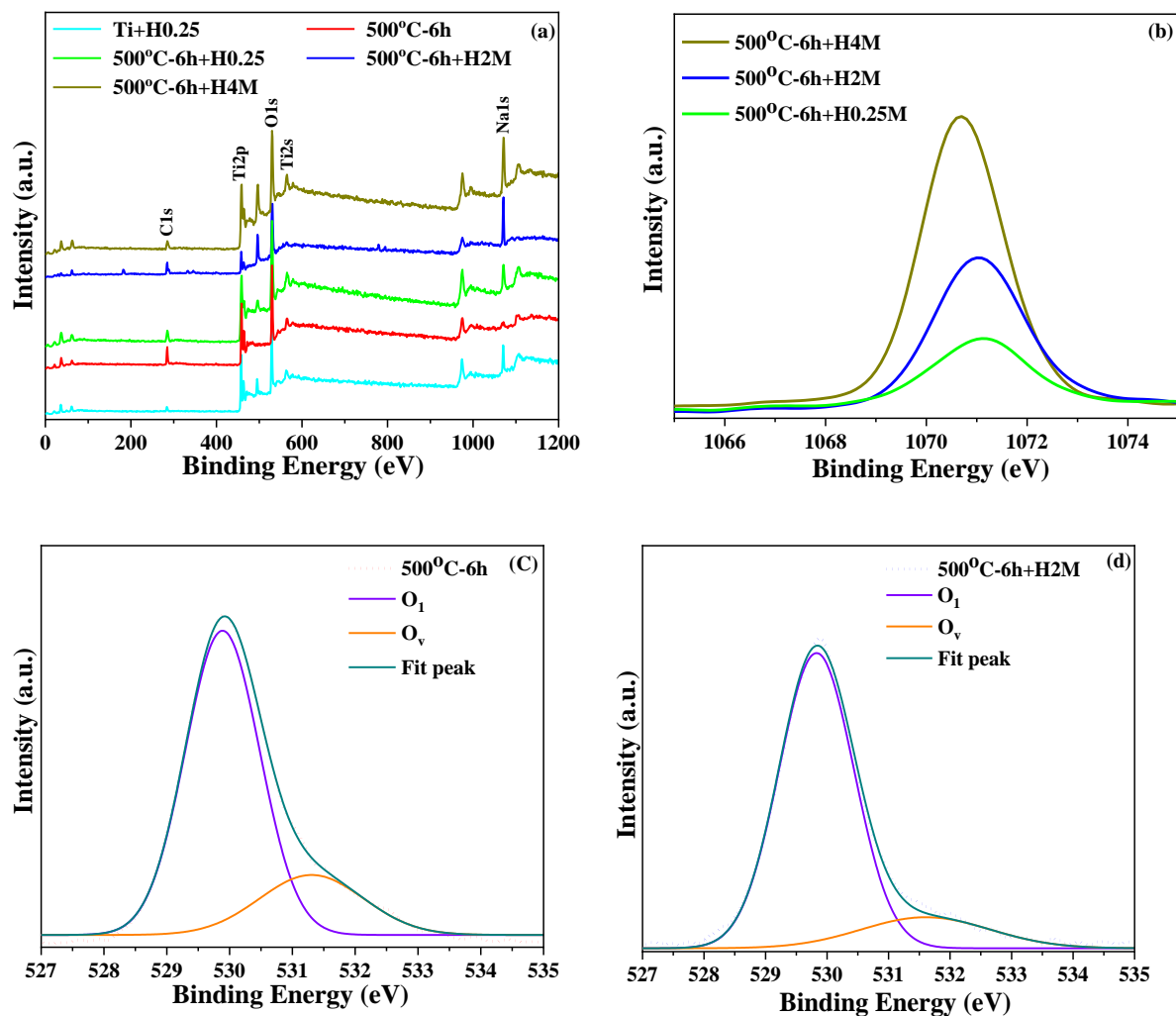


Figure 4. 3. Estimated bandgap energy of (a) Ti+H0.25M and (b) 500oC-6h

#### 4.3.1.3. X-ray photoelectron spectroscopy (XPS)

The XPS analysis was employed to provide information about the chemical state on the surface of as-prepared photoanodes. The XPS survey spectra of the samples consist of three binding energy values at 457.7, 531.6, and 1071.4 eV, which are assignable to Ti 2p, O 1s, and Na 1s, respectively (Fig. 4a). The characteristic peaks mentioned above were detected in all samples except Na 1s in the 500°C-6h sample (due to the absence of alkaline heat treatment on this sample), confirming the presence of all the appropriate elements on the surface layer of each sample. The high-resolution XPS spectra of Na 1s indicate that the increase in the NaOH concentration from 0.25 to 4M in hydrothermal treatment of the thin TiO<sub>2</sub> layer caused the gradual growth of the peak area (larger amount of Na content) for the 500°C-6h+H0.25M, 500°C-6h+H2M and 500°C-6h+H4M samples, respectively (Fig. 4b). The O 1s spectrum of the 500°C-6h and 500°C-6h+H2M samples consists of two separate peaks positioned at binding energies of 529.9 and 531.3 eV, assigned to crystal lattice oxygen (O-Ti<sup>4+</sup>), and the sites of oxygen vacancy defects in the lattice, respectively. Hydrothermal treatment in the 500°C-6h sample with NaOH 2M exhibits a decrease in the area of the oxygen vacancies peak (Figs. 4c and d), resulting from the reaction of these oxygens in the process of sodium titanate nanostructure formation. Figs. 4e and f illustrate that the Ti 2p spectrum of both samples comprises two main peaks at 458.5 (Ti 2p<sub>3/2</sub>) and 464.2 eV (Ti 2p<sub>1/2</sub>). The former consists of two small peaks located around 457.8 and 458.7 eV, and the latter divides into two small peaks around 463.4 and 464.6 eV. The peaks at the binding energy 457.8 and 463.4 eV are attributed to Ti<sup>3+</sup> due to oxygen vacancies, while the binding energy values at 458.7 and 464.6 eV are assigned to the chemical state of Ti<sup>4+</sup> in the crystal lattice [30, 31]. The decrease in the peak

area of  $Ti^{3+}$  after hydrothermal treatment in the thin film of  $TiO_2$  indicates the consumption of  $Ti^{3+}$  in the sodium titanate formation process. These results are consistent with the optical properties of  $500^\circ C-6$  and  $500^\circ C-6h+H2M$  in Fig. 2b. The valence band of the  $500^\circ C-6$  and  $Ti+H0.25M$  photoanodes is obtained based on the results of the valence band XPS. The valence band maximum energy ( $V_B$ ) of these samples were estimated to be 2.4 and 2.15 eV, respectively (Fig. 4g).



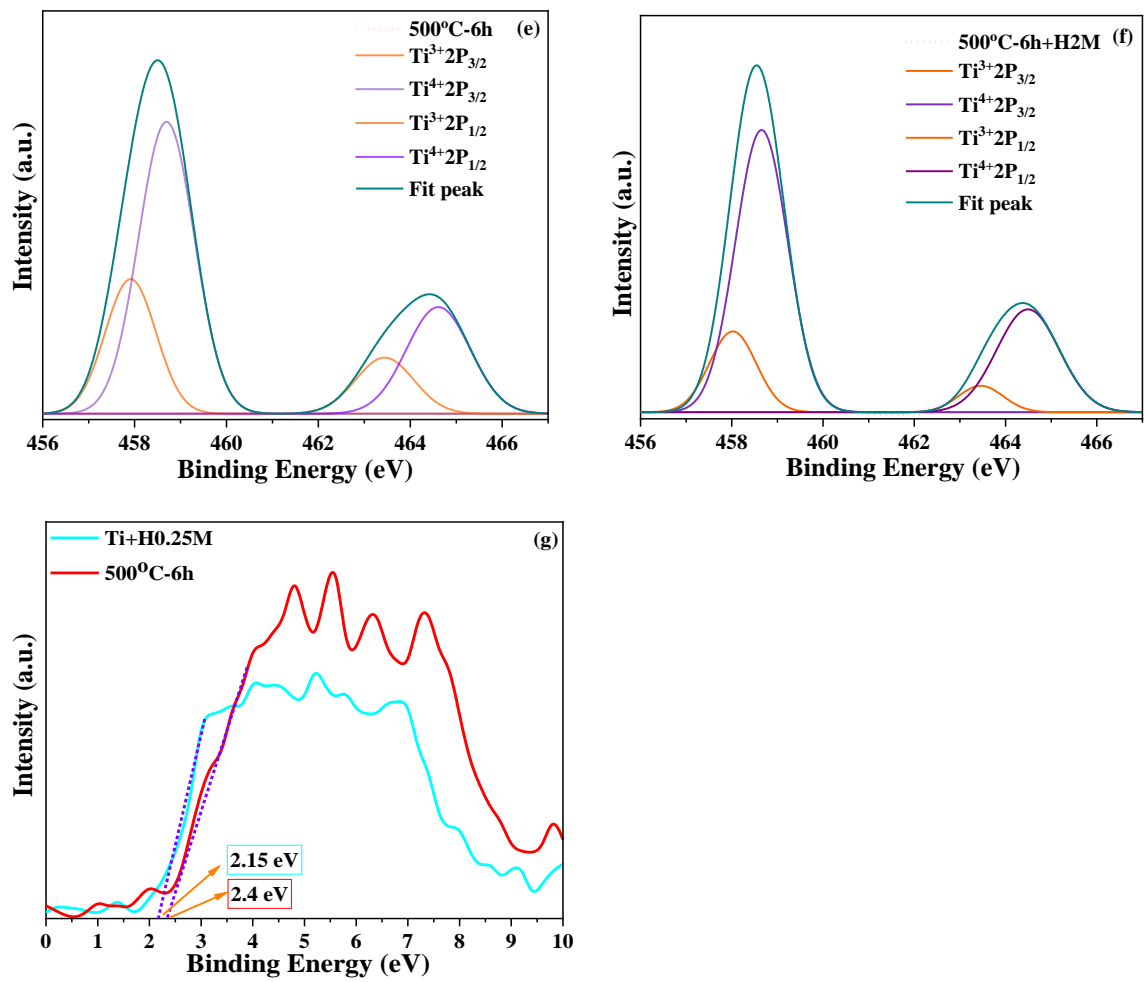


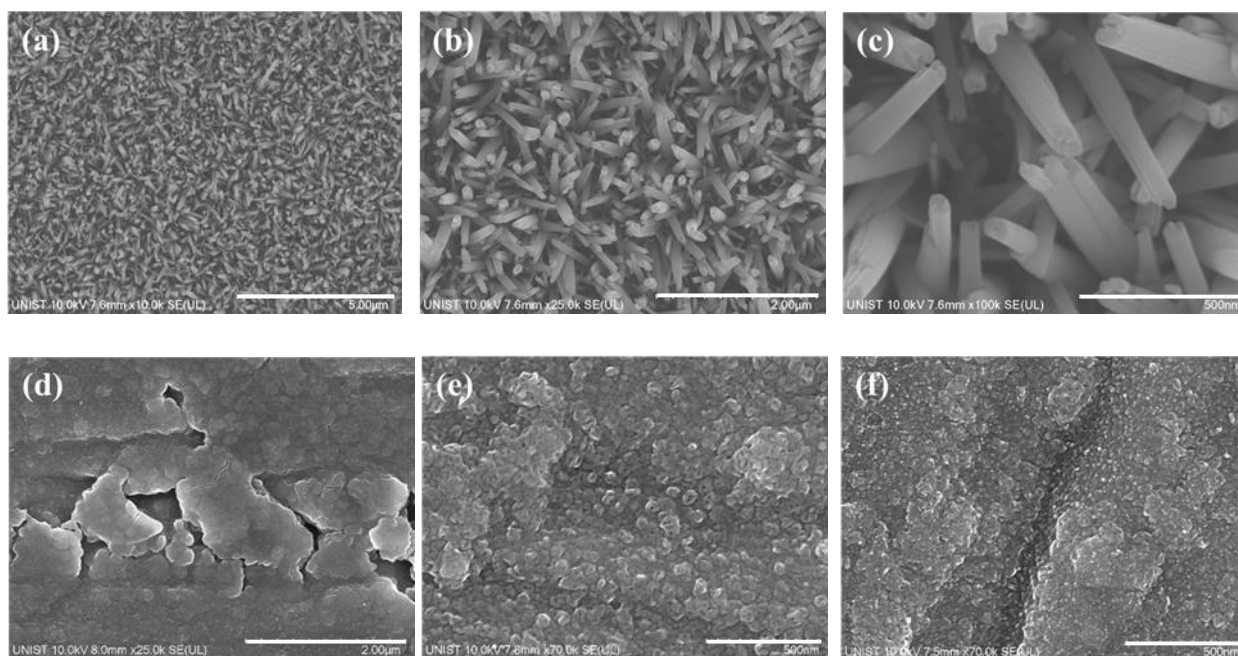
Figure 4. 4. XPS spectra of (a) all samples, high-resolution XPS spectra of (b) Na, (c) O for 500oC-6h, (d) O for 500oC-6h+H2M, (e) Ti for 500oC-6h, (f) Ti for 500oC-6h+H2M and (g) XPS valence band

#### 4.3.1.4. SEM

The SEM images in Fig. 5 show the surface morphology of the Ti foil and the thin TiO<sub>2</sub> film that were treated under a hydrothermal process with different concentrations of NaOH solution. Figs. 5a and b show that the surface of the Ti foil was completely covered with non-uniformed sodium titanate nanorods, which were grown vertically or obliquely in the Ti+H0.25M photoanode after hydrothermal treatment. The average length of the nanorods reached up to 600 nm, and their diameter ranged from 80 to 160 nm (Fig. 5c). The SEM images of the 500°C-6h sample show the



formation of a layer of  $\text{TiO}_2$  consisting of discrete islands of  $\text{TiO}_2$  seeds on the surface of Ti foil (Figs. 5d and e). After the  $\text{TiO}_2$  seed layer is treated with 0.25M NaOH solution in the hydrothermal process, the morphology of the 500°C-6h+H0.25M sample is almost identical to that of the 500°C-6h photoanode, except for the nucleation of the unstable sodium titanate (presented with small white points in Fig. 5f). Increasing NaOH concentration from 0.25M to 2M results in a moderate phase transition of the  $\text{TiO}_2$  seed layer to the flower-like sodium titanate nanostructure phase (Figs. 5g and h). This phenomenon leads to the coexistence of connecting phases, which have both the photocatalytic properties of  $\text{TiO}_2$  and the high surface area of titanate nanoflowers. Furthermore, the formation of the  $\text{TiO}_2/\text{Na}_2\text{Ti}_3\text{O}_7$  photoanode with direct contact to the Ti substrate can facilitate the transfer of photogenerated charge carriers. The magnified SEM image of the nanoflowers is shown in Figs. 5i and j indicate that the flowers are made up of nanosheets grown perpendicularly to the surface of the  $\text{TiO}_2$  seed layer. By increasing the concentration of NaOH to 4M, the Ti substrate was completely covered with a layer of sodium titanate with a structure of nanosheets and nanorods (Figs. 5k, l, m and n).



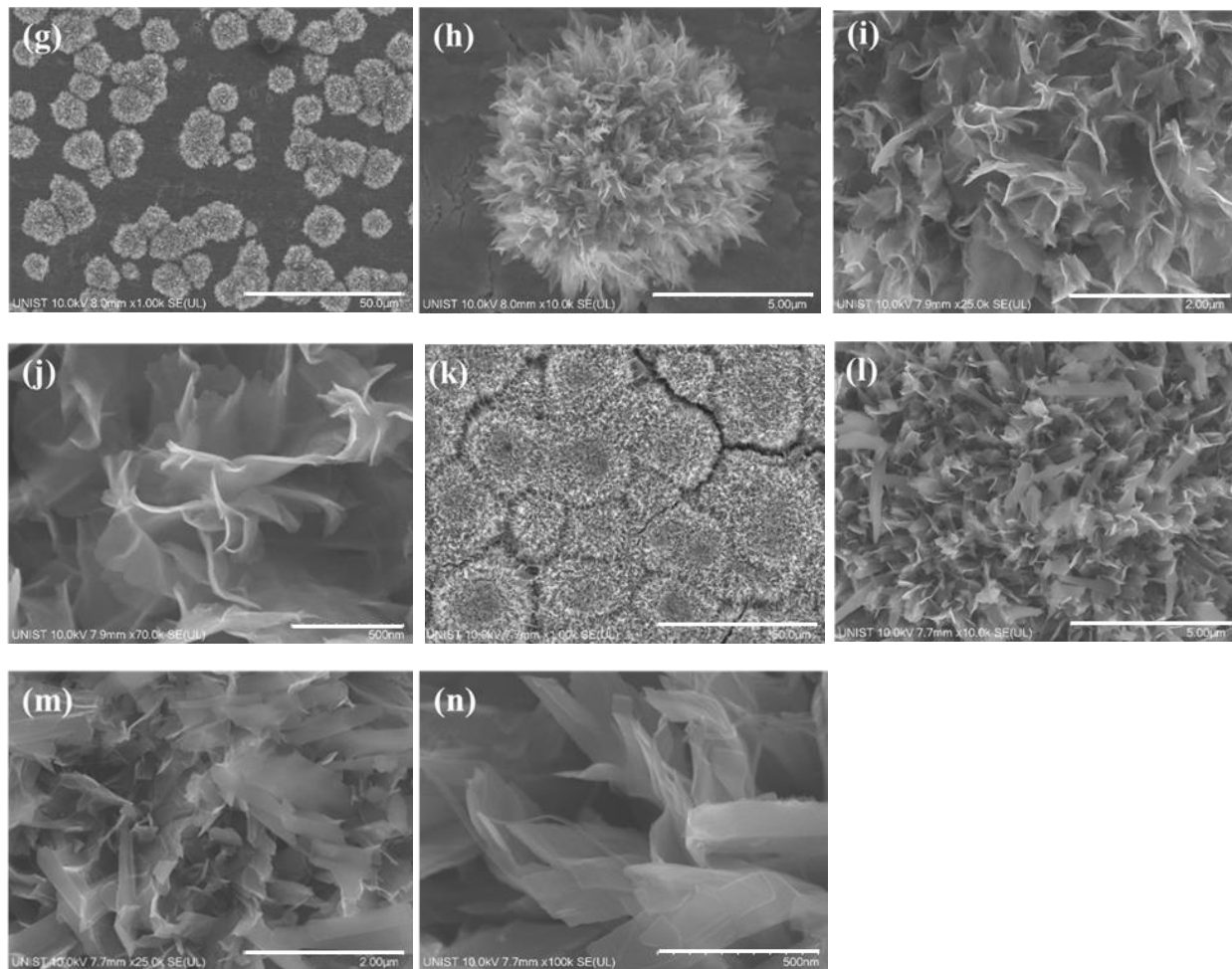


Figure 4. 5. SEM image of (a), (b) and (c) Ti+H0.25M, (d) and (e) 500oC-6h, (f) 500oC-6h+H0.25M, (g), (h), (i) and (j) 500oC-6h+H2M and (k), (l), (m) and (n) 500oC-6h+H4M

The elemental composition of 500°C-6h+H2M and 500°C-6h+H4M, obtained from the EDX spectrum, shows the presence of Na, Ti, and O in both samples (Figs. 6a and c). Increasing the concentration of NaOH from 2 to 4M leads to an increase in the atomic percentage of Na from 2.6 to 9.5 in 500°C-6h+H2M and 500°C-6h+H4M, respectively. Elemental mapping images of these samples indicate that sodium is densely distributed in the places where sodium titanate nanoflowers are located (Figs. 6b and d). In particular, in the 500°C-6h+H2M sample with the TiO<sub>2</sub> and Na<sub>2</sub>Ti<sub>3</sub>O<sub>7</sub> phases, the presence of a dense sodium distribution in the sodium titanate

nanoflower and a negligible distribution in the area of the TiO<sub>2</sub> seed layer confirmed the presence of both phases in this photoanode, which is consistent with our XRD results.

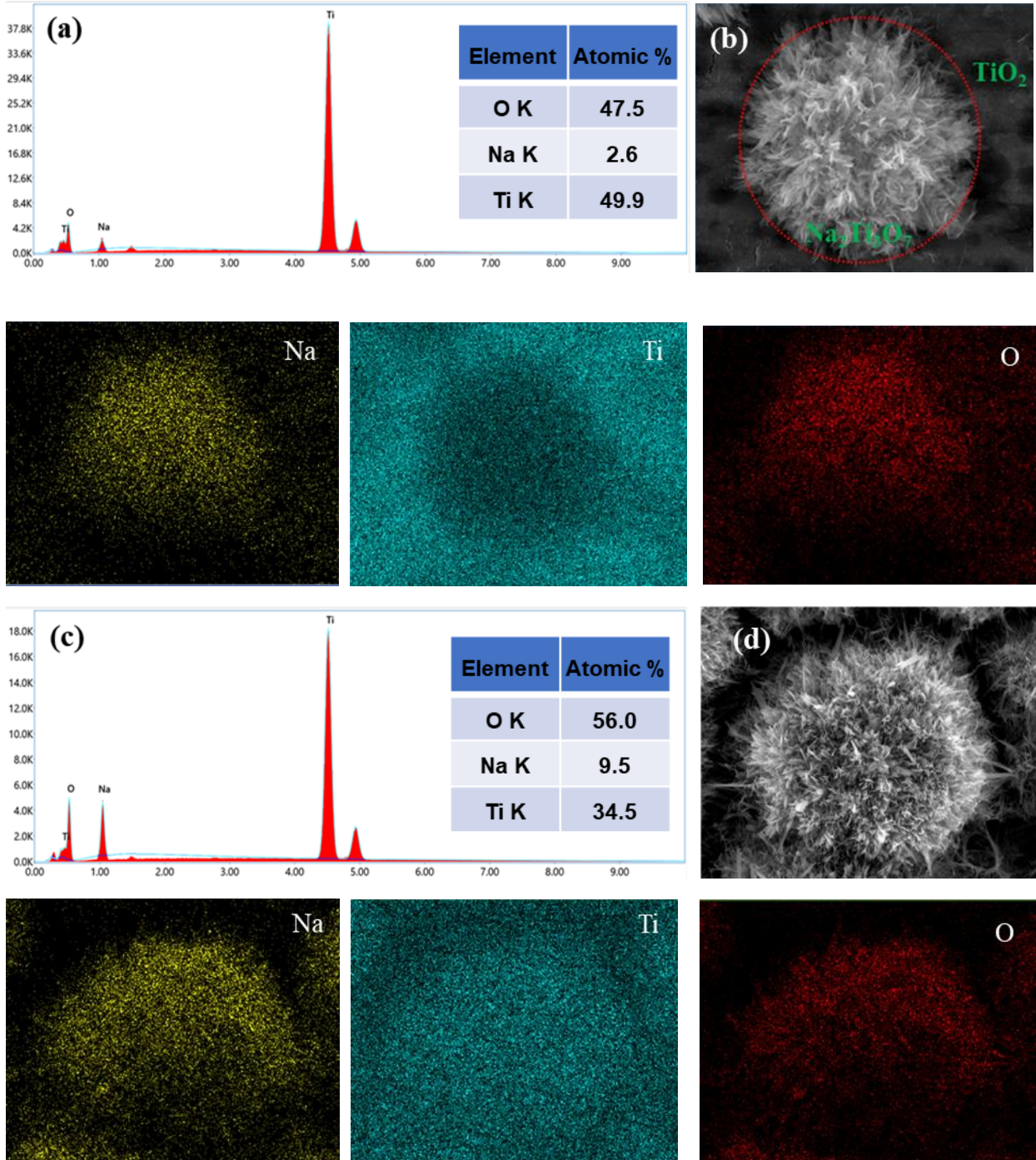


Figure 4. 6. (a) 500oC-6h + H2M EDX analysis, (b) elemental mapping of 500oC-6h+H2M, (c) EDX analysis of 500oC-6h+H4M, (d) elemental mapping of 500oC-6h+H4M

#### 4.3.1.5. PL spectra

Photoluminescence spectra (PL) were employed to investigate the recombination probability of photogenerated carriers in 500°C-6h and 500°C-6h+H2M photoanodes (Fig. 7). Three narrow emission peaks in the visible region (425, 486 and 495 nm) are related to surface defects; particularly, the PL peak at 495 nm is directly attributed to the formation of defects along with oxygen vacancy, as shown by the XPS analysis[32, 33]. Hydrothermal treatment of the TiO<sub>2</sub> seed layer by NaOH 2M causes a reduction in the PL spectra peaks of the 500°C-6h+H2M photoanode compared to the 500°C-6h. This observation implied nucleation of sodium titanate nanostructures at defect sites in the TiO<sub>2</sub> thin film that consume many defects as recombination sites. Moreover, it can be attributed to the electric field associated with the TiO<sub>2</sub> /Na<sub>2</sub>Ti<sub>3</sub>O<sub>7</sub> nanostructure, facilitating the separation of photogenerated electron holes.

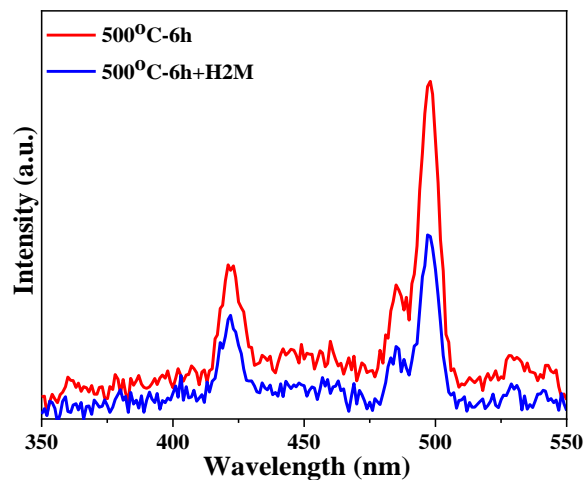


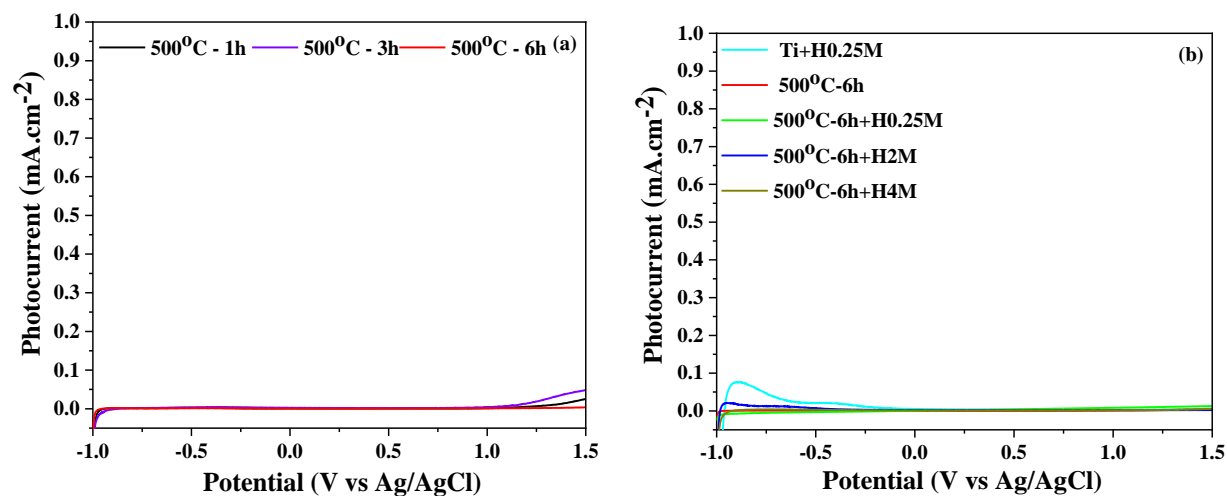
Figure 4. 7. PL spectra of 500oC-6h and 500oC-6h+H2M

## 4.3.2. Photoelectrochemical (PEC) Properties

### 4.3.2.1 PEC performance of photoanodes

The PEC performance of all photoanodes was investigated by linear sweep voltammetry (LSV) between -1 ~ 1.5 V vs Ag / AgCl in 0.5 M Na<sub>2</sub>SO<sub>3</sub> aqueous solution under continuous and periodic illumination with 100 mW.cm<sup>-2</sup> intensity (Fig. 8). 500°C-1h, 500°C-3h, and 500°C-6h samples with the pure TiO<sub>2</sub> phase exhibit photocurrent in approximately 0.11, 0.17, and 0.19 mA/cm<sup>2</sup> at 0.3 V vs Ag / AgCl, respectively. Enhancement of photocurrent density in longer-term calcination indicates that oxidation for 6 h can improve the crystalline quality of the TiO<sub>2</sub> film and reduce the number of defects [34]. All three samples exhibited the same dark current potential behavior from -1 to 1.2 V. As the applied potential increases further, the dark current density for the 500°C-1h and 500°C-3h samples increases slowly. On the contrary, the 500°C-6h sample does not show any dark current at an applied potential higher than 1.2 V (Fig. 8a). The larger photocurrent for the 500°C-3h sample compared to the 500°C-6h sample at a potential higher than 1.2 V in Fig. 8c arises from the larger current of the 500°C-3h sample under dark conditions. The Ti+H0.25M sample composed of pure sodium titanate nanorods (Na<sub>2</sub>Ti<sub>3</sub>O<sub>7</sub>) shows a photocurrent around 0.05 mA/cm<sup>2</sup> at 0.3 V vs Ag / AgCl. This insignificant amount of photocurrent is related to the small concentration of photogenerated electron-hole pairs due to the large bandgap energy of sodium titanate (~ 3.4 eV). The 500°C -6h sample was chosen to investigate the influence of NaOH concentration in the hydrothermal process on the morphology, phase transition, and final PEC performance of the TiO<sub>2</sub> seed layer. Hydrothermal treatment of the TiO<sub>2</sub> seed layer with NaOH 0.25M exhibits an insignificant improvement in photocurrent density due to the same phase and morphology as TiO<sub>2</sub>. While increasing the NaOH concentration to 2M in the 500°C-6h+H2M sample (having both TiO<sub>2</sub> and Na<sub>2</sub>Ti<sub>3</sub>O<sub>7</sub> phases) leads to a noticeable enhancement of the

photocurrent to  $0.46 \text{ mA/cm}^2$  at  $0.3 \text{ V}$  versus  $\text{Ag} / \text{AgCl}$ , which is 9.2 and 2.4 times higher than that of the pure  $\text{Na}_2\text{Ti}_3\text{O}_7$  (Ti+H0.25M) and  $\text{TiO}_2$  ( $500^\circ\text{C}$ -6h) photoanodes, respectively. The improved photocurrent density of the  $500^\circ\text{C}$ -6h+H2M sample can be attributed to the synergistic effect of the large surface area of flower-like sodium titanate and the heterojunction between the  $\text{TiO}_2$  and  $\text{Na}_2\text{Ti}_3\text{O}_7$  phases, as well as the elimination of surface defects in  $\text{TiO}_2$  as recombination centers. The onset potential of  $500^\circ\text{C}$ -6h and Ti + H0.25M was found to be around  $-0.3\text{V}$  vs  $\text{Ag}/\text{AgCl}$ . The  $500^\circ\text{C}$ -6h + H2M photoanode shows a notable negative shift of the onset potential around  $-0.6 \text{ V}$  versus  $\text{Ag} / \text{AgCl}$ . However, an additional increase in  $\text{NaOH}$  concentration from 2 to 4M results in the formation of pure sodium titanate, which suppresses the photocurrent density from  $0.46$  to  $0.08 \text{ mA}$ . Interestingly, Ti + H0.25M and  $500^\circ\text{C}$ -6h+H4M photoanodes showed the same photocurrent density with an identical phase (pure sodium titanate). The dark and chopped LSV curves displayed the current density around zero in the dark condition for all samples, indicating that the current under light illumination is generated by the interplay of the light and photoelectrodes. Furthermore, the quantitative amounts of photocurrent density of different photoanodes in chopped LSV curves are identical with LSV results in continuous light illumination (Figs. 8d and f).





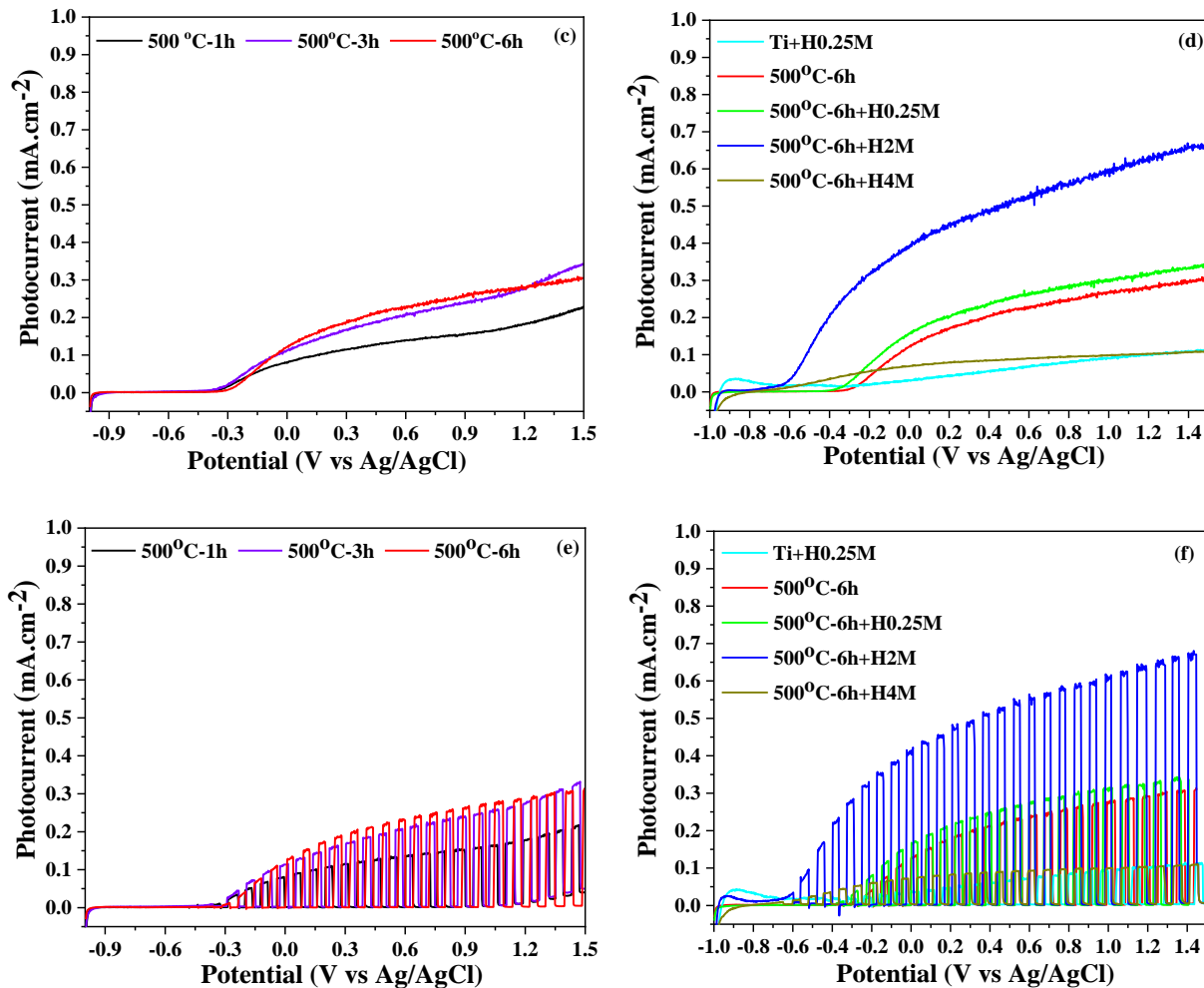


Figure 4. 8. (a) and (b) LSV dark illumination, LSV of (c) 500°C-1h, 500°C-3h and 500°C-6h samples and (d) Ti+H0.25M, 500°C-6h, 500°C-6h+H0.25M, 500°C-6h+H2M, 500°C-6h+H4M samples, (e) and (f) LSV chopped illumination of different photoanodes.

Chronoamperometric measurements have been conducted to investigate the photocurrent response under chopped illumination and photocurrent stability for all photoelectrodes at 0.3 V vs Ag/AgCl (Figs. 9a and b). A spike response and recovery of the photocurrent upon each on/off cycle reveal an effective charge separation at the interface and a fast transfer of photogenerated electrons through the nanocomposite to the substrate. The order of enhancement in the photocurrent density of all photoelectrodes is consistent with the LSV results. The highest photocurrent density was obtained by the 500°C-6h+H2M sample, which retained its initial photocurrent even after 16 h.

We applied SEM analysis for the 500°C-6h+H2M sample to investigate the structural stability of the surface morphology after chronoamperometric measurement (Fig. 10). It is clearly seen that there is no change in the morphology of the photoanode after 4 h of working, and the structure of sodium titanate nanoflowers remains intact.

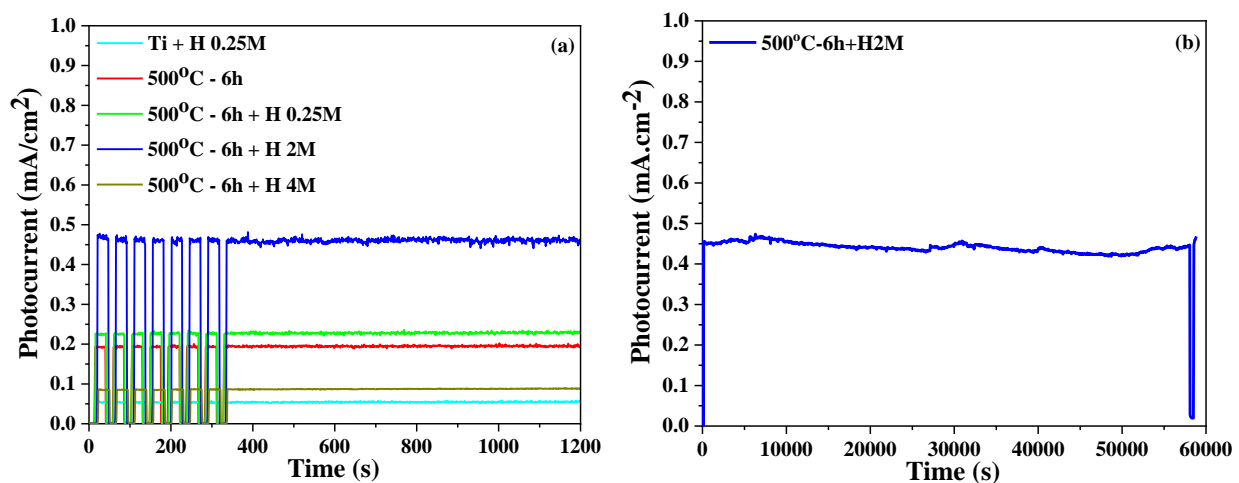
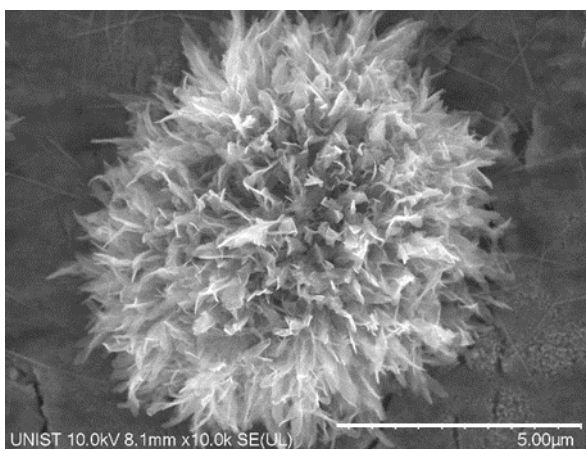
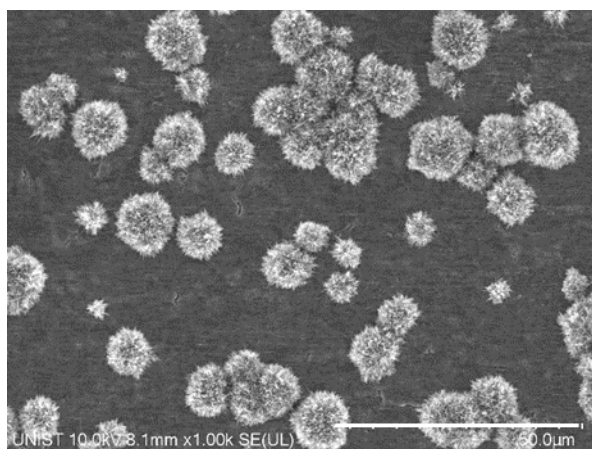


Figure 4. 9. (a) Photocurrent response at the potential of 0.3 V versus Ag/AgCl and (b) long time stability of 500oC-6h+H2M





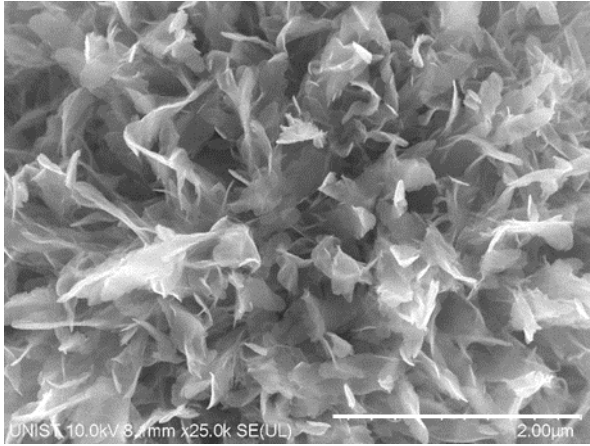


Figure 4. 10. SEM image of 500oC-6h + H2M after 4 h chronoamperometric measurement.

The open-circuit potential (OCP) measurement was performed to evaluate the conductivity type of all photoelectrodes from the OCP shift direction under light illumination and further discuss the discrepancy of their PEC activity from OCP. Fig. 11a shows that all photoelectrodes showed a negative enhancement in voltage under light irradiation, suggesting that photoinduced electrons were injected from the surface of the semiconductors into the Ti substrates, which results in the generation of anodic photocurrent in LSV and chronoamperometry analyzes. This anodic photocurrent confirmed that all as-synthesized photoanodes act as n-type semiconductors. The difference between the voltage in the dark and under light irradiation (OCP) reflects the density of the photoinduced charge carrier. The 500°C-6h+H2M sample with heterojunction structure showed a larger  $\Delta\text{OCP}$  (0.56 V) compared to pristine sodium titanate (0.07 V) and titania (0.46 V), which is more noticeable photoelectric response in this photoanode.

To investigate the photogenerated charge separation and transferability of all as-prepared photoelectrodes, electrochemical impedance spectroscopy (EIS) was performed under 100  $\text{mW}\cdot\text{cm}^{-2}$  irradiation and frequency range from 0.1 to 100 KHz at bias voltage 0.2 V vs Ag/AgCl. Fig. 11b demonstrates the Nyquist plots of the prepared photoanodes and their fitting results using

the Randles circuit model. There are two types of resistance against the transference of charge carriers, while the electrochemical reaction occurs in a PEC cell, including series resistance ( $R_s$ ) and charge transfer resistance across the photoelectrode and solution ( $R_{ct}$ )[35]. The estimated  $R_s$  values from the X-intercept of Nyquist plots in Table 1 do not show noticeable differences between different samples. However, the  $R_{ct}$  value of the 500°C-6h+H2M sample is much lower than that of the Ti+H0.25M and 500°C-6h samples. The smallest  $R_{ct}$  in the Nyquist plot of the 500°C-6h+H2M photoanode can promote the separation of photogenerated charge carriers and improve the interfacial transfer of the hole from the photoelectrode to the electrolyte in this sample.

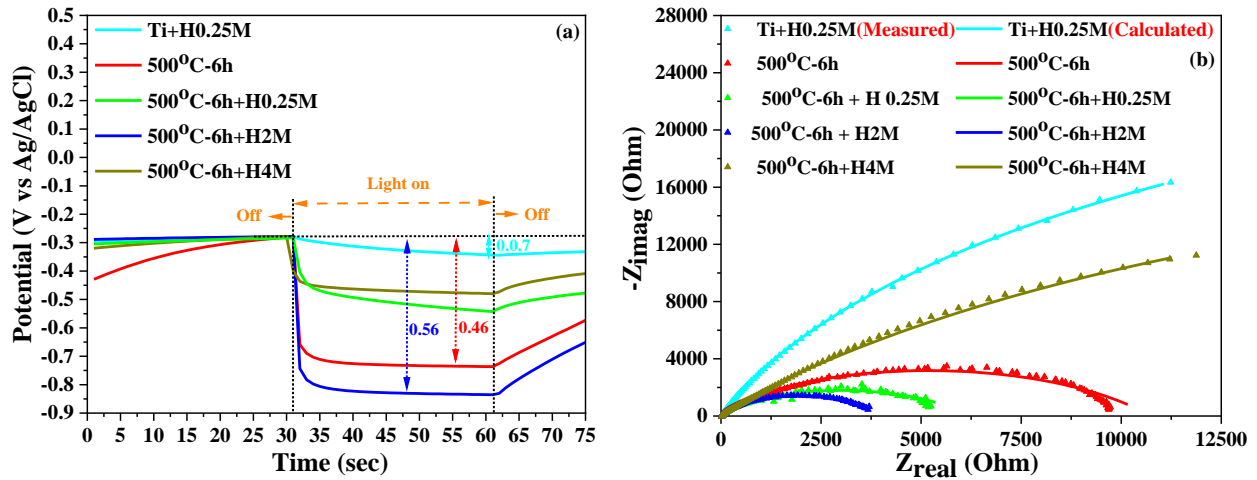


Figure 4. 11. (a) Transient OCP and (b) EIS Nyquist plot of Ti+H0.25M, 500oC-6h, 500oC-6h+H0.25M, 500oC-6h+H2M, 500oC-6h+H4M samples.

Table 4. 1. Calculated  $R_s$  and  $R_{ct}$  for different photoanodes using the Randles circuit model

Samples	$R_s$ ( $\Omega$ )	$R_{ct}$ ( $\Omega$ )
Ti+H0.25M	20.47	58260
500°C-6h	19.23	10720
500°C-6h+H0.25M	21.38	6230
500°C-6h+H2M	22.58	3989
500°C-6h+H4M	26.81	57620

To evaluate the effect of NaOH concentration during the hydrothermal process on the PEC performance of the TiO<sub>2</sub> seed layer, the Mott-Schottky analysis of 500°C-6h, 500°C-6h+H0.25M, 500°C-6h+H2M and 500°C-6h+H4M photoanodes was carried out at different frequencies (f = 1000, 500 and 100 HZ). Mott-Schottky results at f = 100 HZ were used to determine the carrier concentration (N<sub>D</sub>) and the flat band potential (V<sub>fb</sub>) of the photoanodes. The Mott-Schottky equation correlates the capacitance (C) vs the applied voltage (V) at the interface of semiconductor/electrolyte under depletion conditions. Thus, the density of donors can be calculated from the slope of 1 / C<sup>2</sup> vs applied voltage in the linear region, and the flat band potential can be estimated from the value of the X-intercept of the Mott-Schottky curves by using the following equation [36-38]:

$$\frac{1}{C^2} = \frac{2}{\epsilon\epsilon_0 A^2 e N_D} \left( V - V_{fb} - \frac{k_B T}{e} \right) \quad (1)$$

Figure 12 illustrates that all samples have a positive slope at all frequencies, indicating that all prepared electrodes act as an n-type semiconductor, consistent with the OCP results. However, after hydrothermal treatment, the slope in the linear part of the 500°C-6h sample is declined by increasing the concentration of NaOH up to 2M in all frequencies, indicating the highest density of donors was obtained in 500°C-6h+H2M photoanode. Furthermore, hydrothermal treatment of the 500°C-6h sample decreased the flat band potential of the TiO<sub>2</sub> seed layer from -0.14 to -0.68 V versus Ag / AgCl for the 500°C-6h + H2M photoelectrode, which is attributed to the noticeable reduction in the recombination of photogenerated charge carriers. Table 2 shows the estimated amount of N<sub>D</sub> and V<sub>fb</sub> of all photoanodes using the Mott-Schottky equation.

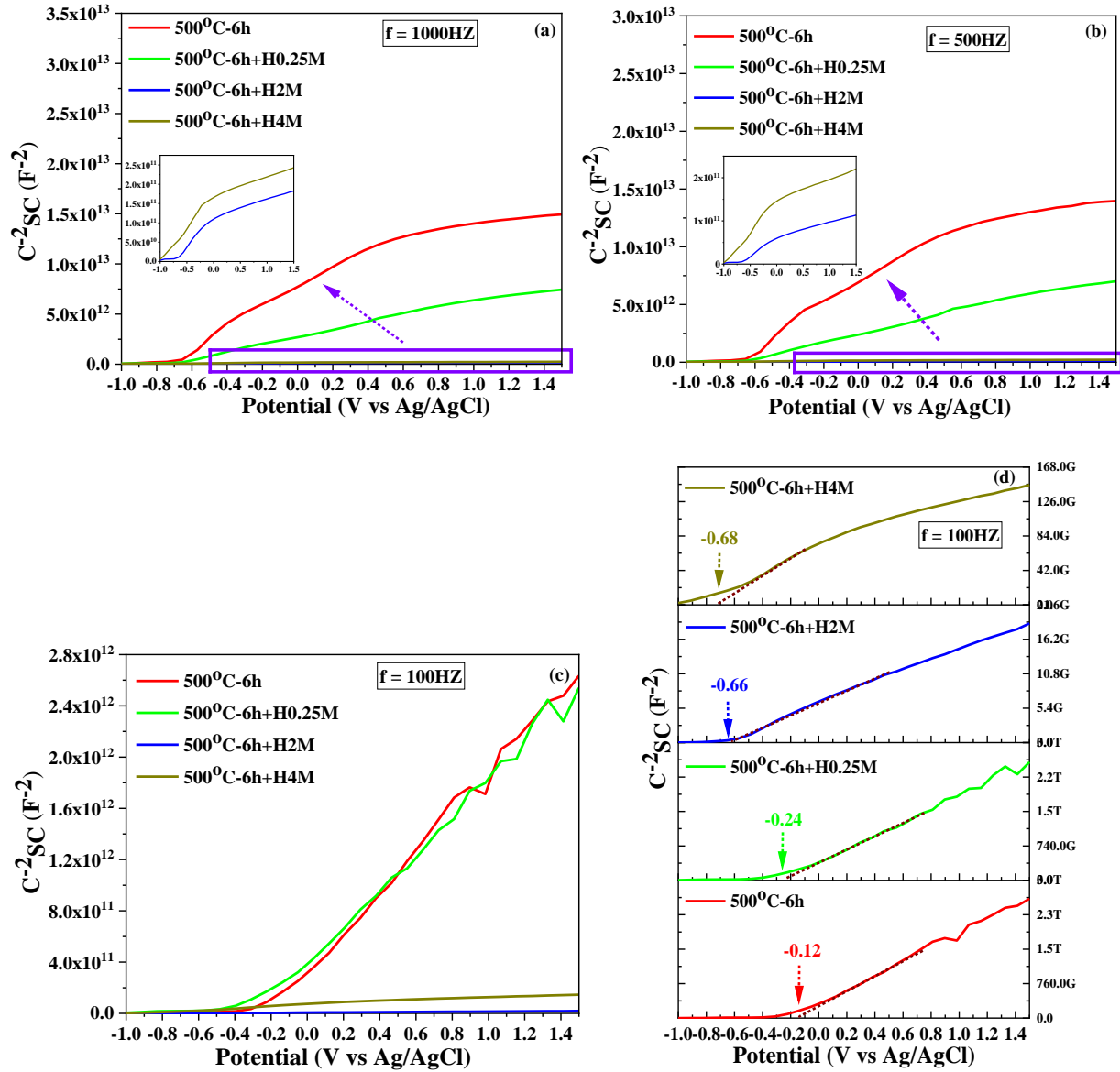


Figure 4. 12. Mott-Schottky plot of 500oC-6h, 500oC-6h+H0.25M, 500oC-6h+H2M and 500oC-6h+H4M at different frequencies (a) 1000HZ, (b) 500 HZ, (C) and (d) 100 HZ (a).

Table 4. 2. Summarized  $V_{fb}$  and  $N_D$  values obtained from the X intercept and the slope in the Mott-Schottky plots

Samples	slope	intercept	$N_D$ ( $m^{-3}$ )	$V_{fb}$ (V)
500°C-6h	1.62E+12	-0.12	3.92E+26	-0.14
500°C-6h+H0.25M	1.32E+12	-0.24	4.64E+26	-0.26
500°C-6h+H2M	9.7E+09	-0.66	6.55E+28	-0.68
500°C-6h+H4M	9.6E+10	-0.69	6.62E+27	-0.71

The applied bias photon-to-current conversion efficiency (ABPE) for PEC water splitting of different samples was estimated based on the LSV results and the following equation:

$$ABPE\% = I \frac{(1.23 - V_{app})}{P_{light}} \quad (2)$$

where I is the measured photocurrent density at different applied potentials ( $V_{app}$ ), and P is the power density of the incident light. As shown in Fig. 13a, the maximum ABPE% was 0.48% for the 500°C-6h+H2M photoanode, which is 12 and 2.8 times higher than those of pure  $Na_2Ti_3O_7$  (Ti+H0.25M) and pure  $TiO_2$  (500°C-6h), respectively. Thus, the electrochemical results presented above clearly concluded that the synergistic effects of the initial oxidation of the Ti foil and hydrothermal treatment played a positive role in enhancing the PEC performance of both pure phases.

Incident photon-to-current-efficiencies (IPCE) analysis was utilized for all photoanodes to understand their specific PEC active spectra (Fig. 13b). IPCE values for different samples were calculated using the following equation[38]:

$$IPCE, \% = \left( \frac{1240}{\lambda} * \frac{J_{light} - J_{dark}}{P_{light}} \right) * 100 \quad (3)$$

where  $J_{light}$  is the photocurrent density at  $\lambda$  (wavelength of incident light),  $J_{dark}$  is the dark current density, and  $P_{light}$  represents the light power at specific wavelengths. The maximum IPCE is around 6.25% at a wavelength of 300 nm for the 500°C-6h+H2M photoanode, composed of both titania and sodium titanate phases, which is much higher than 0.5 and 3.5% for pure sodium titanate and titania, respectively. The IPCE values of the Ti+H0.25 and 500°C-6h samples decrease to zero for wavelengths larger than 375 and 410 nm, respectively, which are consistent with their estimated bandgap energy results.

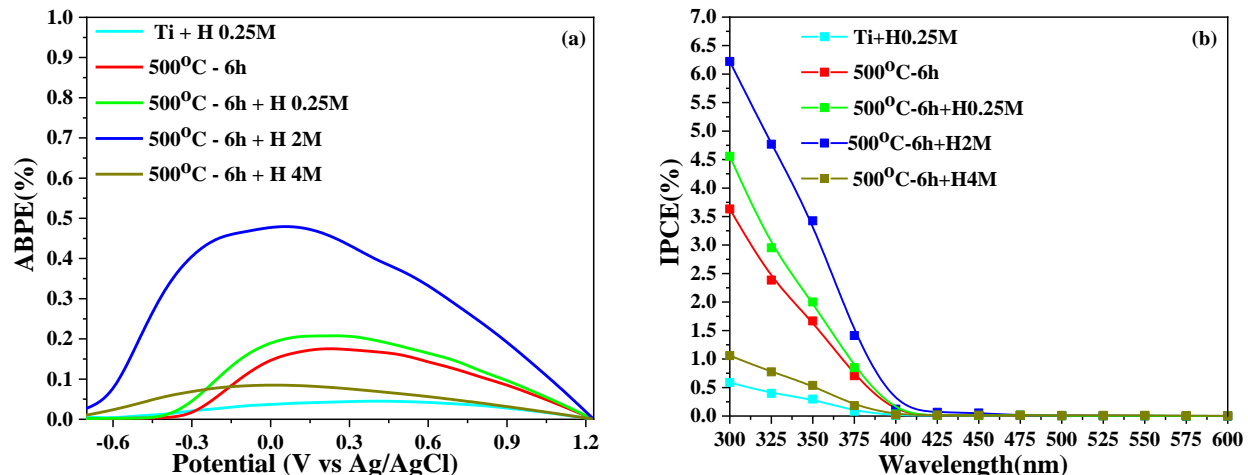


Figure 4. 13. (a) Photoconversion efficiency as a function of applied voltage versus Ag / AgCl and (b) IPCE spectra of different photoanodes at 0.3 V versus Ag / AgCl.

#### 4.3.2.2. PEC performance of the 500°C-6h+H2M photoanode after acid treatment and calcination at different temperatures

The alkali titanate family and  $\text{TiO}_2$  have a similar crystal structure with  $\text{TiO}_6$  octahedral connectivity and configuration. Therefore, the sodium titanate phase can be converted to the  $\text{TiO}_2$  phase while preserving its original morphology. The reaction between  $\text{Na}_2\text{Ti}_3\text{O}_7$  and  $\text{HCl}$  will replace  $\text{Na}^+$  with  $\text{H}^+$  to form metastable  $\text{H}_2\text{Ti}_3\text{O}_7$ . Calcination at higher temperatures caused decomposition of the  $\text{H}_2\text{Ti}_3\text{O}_7$  structure by converting to the  $\text{TiO}_2$  phase by losing hydrate. The 500°C-6h+H2M photoanode was chosen to evaluate the effect of the calcination temperature on the phase and structural transition and the final performance of the PEC. Fig. 14 demonstrates the XRD patterns of the 500°C-6h+H2M sample after acid treatment and calcination at temperatures of 500°C, 600°C and 700°C. The XRD peaks at  $2\theta = 9^\circ$  and  $47.8^\circ$  corresponding to  $\text{Na}_2\text{Ti}_3\text{O}_7$  at 500°C-6h+H2M disappeared after the acid treatment and calcination processes. The disappearance of the diffraction peak at  $9^\circ$  is attributed to substituting  $\text{Na}^+$  with  $\text{H}^+$  during treatment with  $\text{HCl}$  solution [39]. Furthermore, survival of diffraction peaks at  $2\theta = 27.4^\circ$ ,  $41.2^\circ$  and  $54.4^\circ$  and

appearance of two new peaks at  $56.6^\circ$  and  $64^\circ$  are attributed to the  $\text{TiO}_2$  phase, confirming the transition phase from titanate to titania which leads to the formation of pure  $\text{TiO}_2$  phase in all samples after annealing treatment.

The SEM images in Fig. 15 show the surface morphology of  $\text{TiO}_2$  nanoflower in  $500^\circ\text{C}$ -6h+H2M+ $500^\circ\text{C}$ ,  $500^\circ\text{C}$ -6h+H2M+ $600^\circ\text{C}$  and  $500^\circ\text{C}$ -6h+H2M+ $700^\circ\text{C}$  photoelectrodes. After calcination at  $500^\circ\text{C}$  the shape of nanosheets in  $\text{TiO}_2$  nanoflower remained intact. Increasing the calcination temperature to  $600^\circ\text{C}$  leads to the conversion of nanosheets into nanoparticles in some areas of the nanoflower, which interrupts the surface of the nanosheets to be in continuous form some areas (these areas are marked with red circles). Further increasing the temperature to  $700^\circ\text{C}$  shows a huge change in the structure of the  $\text{TiO}_2$  nanoflower. The higher magnification image of this sample illustrates the complete collapse of nanosheets into nanoparticles that are aggregated in some areas and short contact in other parts.

Figure 16a shows the PEC performance of synthesized photoanodes with a pure  $\text{TiO}_2$  phase. It can be clearly seen after the conversion of titanate nanoflowers into titania phase on the surface of the  $500^\circ\text{C}$ -6h+H2M sample, the photocurrent density of all photoanodes decreased significantly with increasing calcination temperature. The photocurrent density of the  $500^\circ\text{C}$ -6h+H2M sample decreased from  $0.46 \text{ mA/cm}^2$  at  $0.3 \text{ V vs. Ag/AgCl}$  to  $0.27$ ,  $0.17$  and  $0.06 \text{ mA}$  in  $500^\circ\text{C}$ -6h+H2M+ $500^\circ\text{C}$ ,  $500^\circ\text{C}$ -6h+H2M+ $600^\circ\text{C}$  and  $500^\circ\text{C}$ -6h+H2M+ $700^\circ\text{C}$  photoanodes, respectively. Furthermore, the onset potential of the  $500^\circ\text{C}$ -6h+H2M sample showed a positive shift from  $-0.6$  to  $-0.45 \text{ V vs Ag / AgCl}$  after acid treatment and calcination at  $700^\circ\text{C}$ . These results confirmed that the type II heterojunction between  $\text{TiO}_2$  and  $\text{Na}_2\text{Ti}_3\text{O}_7$  in the  $\text{Ti/TiO}_2/\text{Na}_2\text{Ti}_3\text{O}_7$  sample significantly improved the separation and transfer of charge carriers compared to the photoanode with pure  $\text{TiO}_2$  phase and the same morphology ( $500^\circ\text{C}$ -6h+H2M+ $500^\circ\text{C}$ ). The huge reduction in

photocurrent density after calcination at 700°C can be attributed to the structure of TiO<sub>2</sub> in this sample, which provides an unfavorable path for the transfer of photogenerated carriers through nanoparticles with inadequate contact.

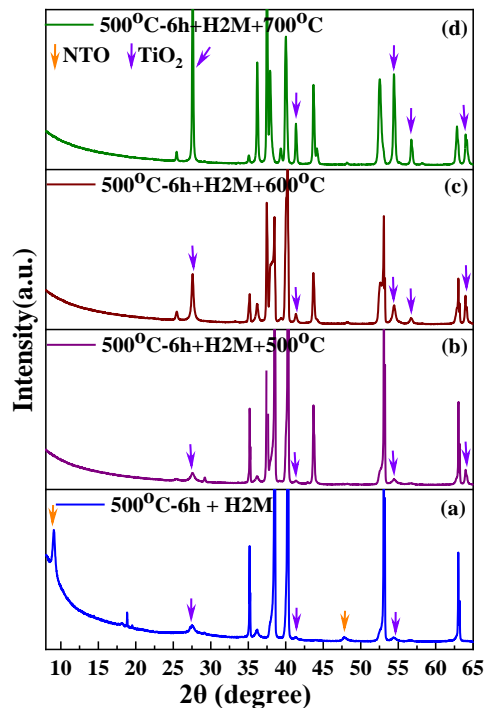


Figure 4. 14. XRD patterns of (a) 500oC-6h+H2M, (b) 500oC-6h+H2M+500oC (c) 500oC-6h+H2M+600oC, (d) 500oC-6h+H2M+700oC



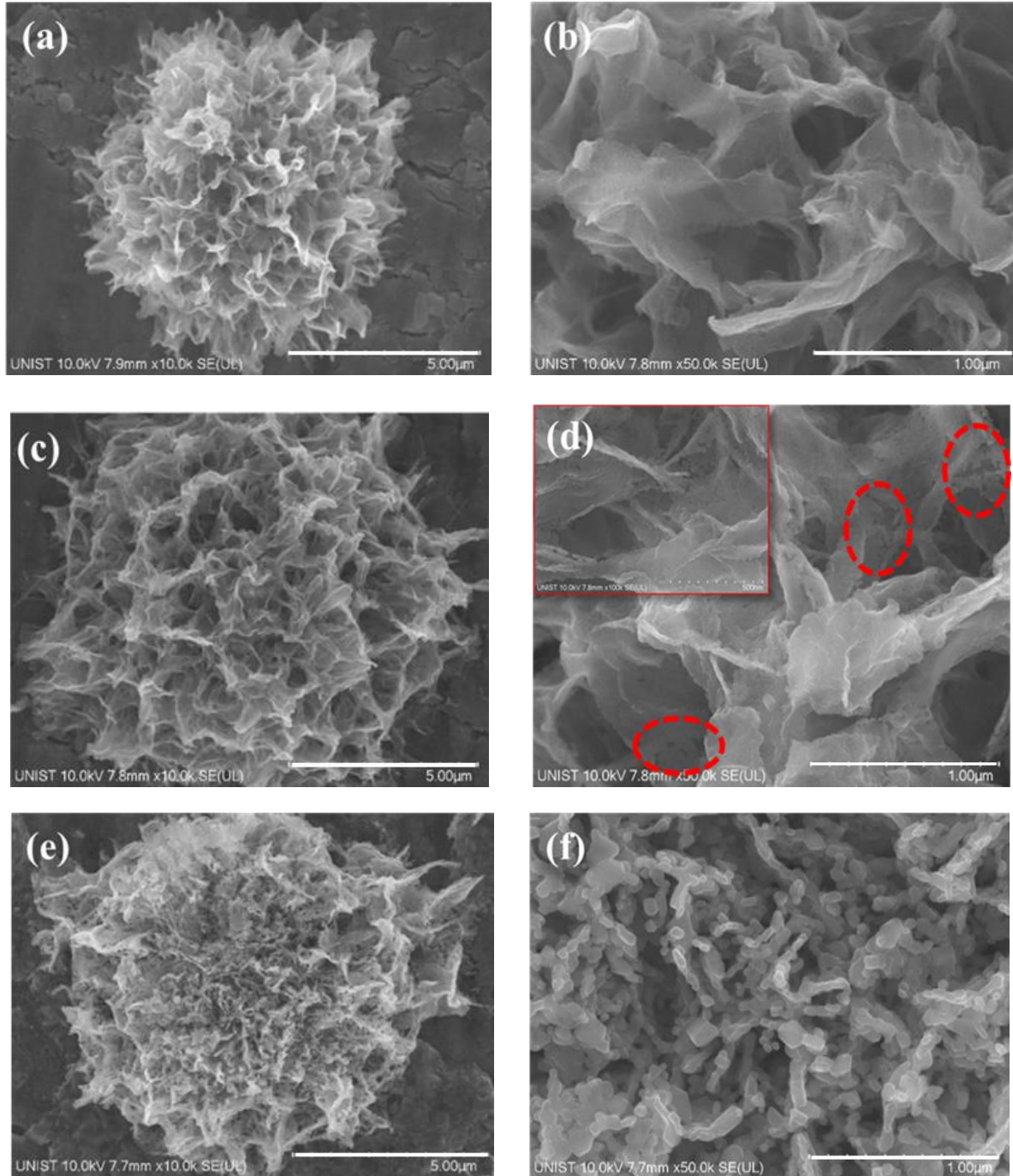


Figure 4. 15. SEM images of (a) and (b) 500oC-6h+H2M+500oC, (c) and (d)500oC-6h+H2M+600oC, (d) and (f) 500oC-6h+H2M+700oC

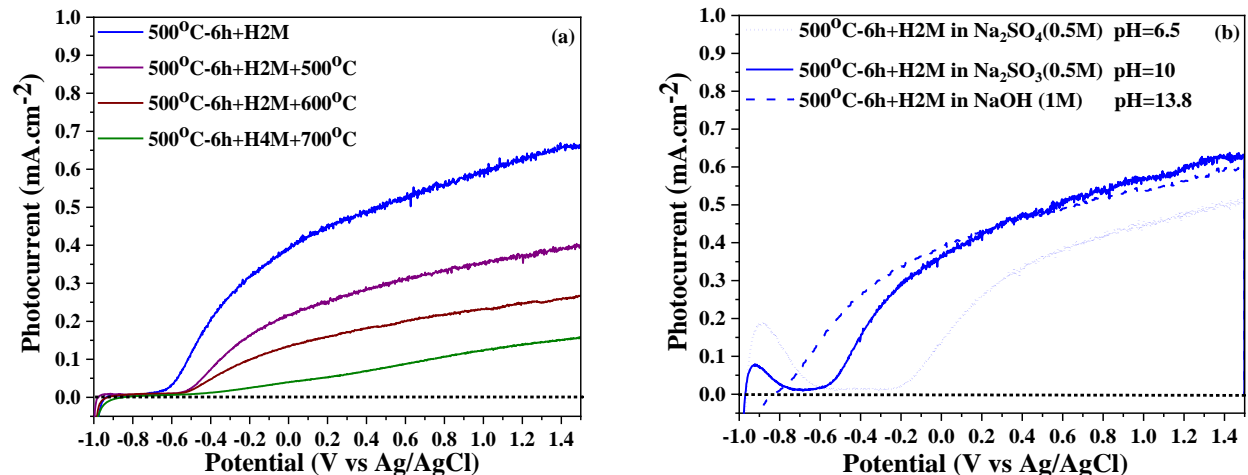


Figure 4. 16. (a)Linear sweep voltammetry of the 500oC-6h+H2M, 500oC-6h+H2M+500oC, 500oC-6h+H2M+600oC and 500oC-6h+H2M+700oC photoanodes and (b) Linear sweep voltammetry of the 500oC-6h+H2M photoanode in different electrolyte solutions

#### 4.3.2.3. Effect of electrolyte on the PEC performance of the 500°C-6h+H2M photoanode

To investigate the impact of electrolyte on the PEC performance of the 500°C-6h+H2M photoanode, its photocurrent density was measured in a Na<sub>2</sub>SO<sub>4</sub> 0.5M, Na<sub>2</sub>SO<sub>3</sub> 0.5M and NaOH 1M solution with pH=6.5, pH=10 and pH=13.8, respectively (Fig. 16b). The photocurrent density in Na<sub>2</sub>SO<sub>3</sub> 0.5M solution is noticeably higher than that of Na<sub>2</sub>SO<sub>4</sub> 0.5M with lower pH. Furthermore, the onset potential shifted from -0.2V to -0.6V. This enhancement in photocurrent density and a negative shift in onset potential in Na<sub>2</sub>SO<sub>3</sub> 0.5M solution can be attributed to its higher pH value and the presence of SO<sub>3</sub><sup>2-</sup> as a hole scavenger, which can facilitate the separation of charge carriers. On the other hand, using the NaOH 1M solution with a higher pH changed the onset potential to a more negative value around -0.8 V, suggesting a decrease in the overpotential of water oxidation.

### 4.3.3. Measurement of evolved H<sub>2</sub> and O<sub>2</sub>

Figs. 13a and b show the amount of hydrogen and oxygen generated as a function of the reaction time for Ti + H0.25M, 500°C-6h, and 500°C-6h+H2M photoanodes. The total H<sub>2</sub> generated after 2 h of irradiation for Ti+H0.25M, 500°C-6h and 500°C-6h+H2M is 1.4, 5.6 and 13.6 μmol.cm<sup>-2</sup>, respectively, and the total O<sub>2</sub> generated is 0.68, 2.8 and 7.1 μmol.cm<sup>-2</sup>, respectively. These identified values provide clear evidence of the split of water into H<sub>2</sub> and O<sub>2</sub> gases.

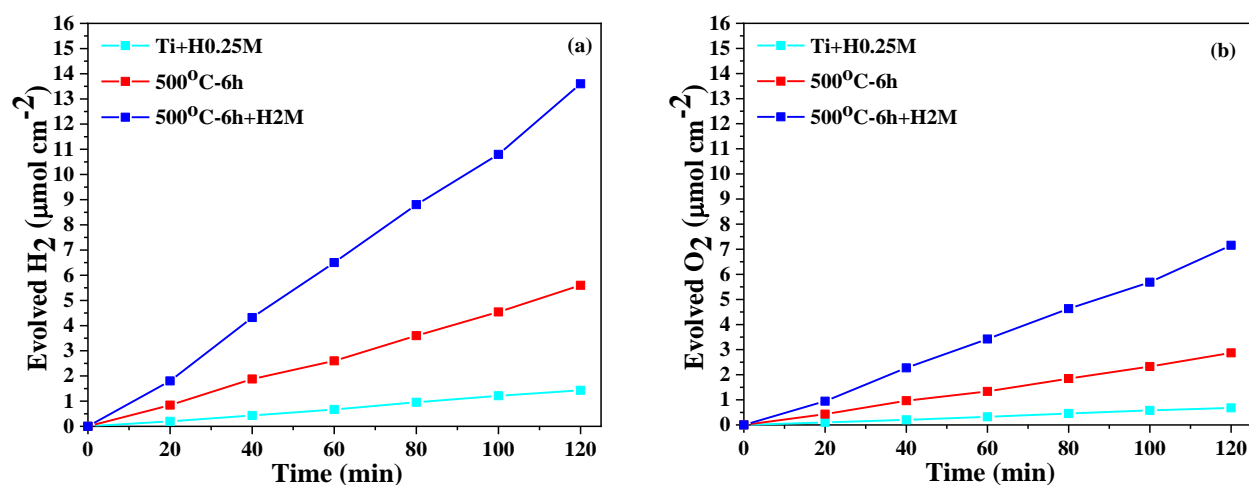


Figure 4. 17. (a) Evolution of H<sub>2</sub> and (b) O<sub>2</sub> versus reaction time per illuminated area (1cm<sup>2</sup>) for Ti+H0.25M, 500oC-6h and 500oC-6h+H2M electrodes at a potential of 0.3V (versus Ag / AgCl). Under 100 mW.cm<sup>-2</sup> irradiations, the electrolyte was an aqueous solution of Na<sub>2</sub>SO<sub>3</sub> 0.5M (PH = 10).

### 4.3.4. Mechanism of PEC performance enhancement

Figure 18 shows a schematic of the relative positions of the band structure for the 500°C-6h+H2M photoanode with the highest photocurrent density to show the possible transfer mechanism of photogenerated charge carriers. The energy band gap value from UV-Vis spectra and the relative valence band from valence band XPS illustrate that the TiO<sub>2</sub> bands are lower than the Na<sub>2</sub>Ti<sub>3</sub>O<sub>7</sub> ones. These proper band edges confirm the formation of a type II heterojunction between the TiO<sub>2</sub> seed layer and Na<sub>2</sub>Ti<sub>3</sub>O<sub>7</sub> nanoflowers. The conduction band potential (C<sub>B</sub>) of Na<sub>2</sub>Ti<sub>3</sub>O<sub>7</sub> in this

heterostructure (-1.25 V) is high enough compared to the corresponding  $C_B$  of  $\text{TiO}_2$  (-0.6 V), which causes photogenerated electrons to thermodynamically transfer from the titanate phase to the titania. Also, photogenerated holes tend to migrate from the  $V_B$  of titania to the titanate phase to participate in the oxygen evolution reaction (OER) on the surface of titanate nanoflowers. Simultaneously, photogenerated electrons can easily pass through the titanate and titania layer to reach the surface of the Ti substrate due to the suitable thermodynamic process and the great contact in the  $\text{Ti}/\text{TiO}_2/\text{Na}_2\text{Ti}_3\text{O}_7$  junctions. Finally, electrons can migrate to the surface of Pt as a counter electrode to participate in the hydrogen evolution reaction (HER).

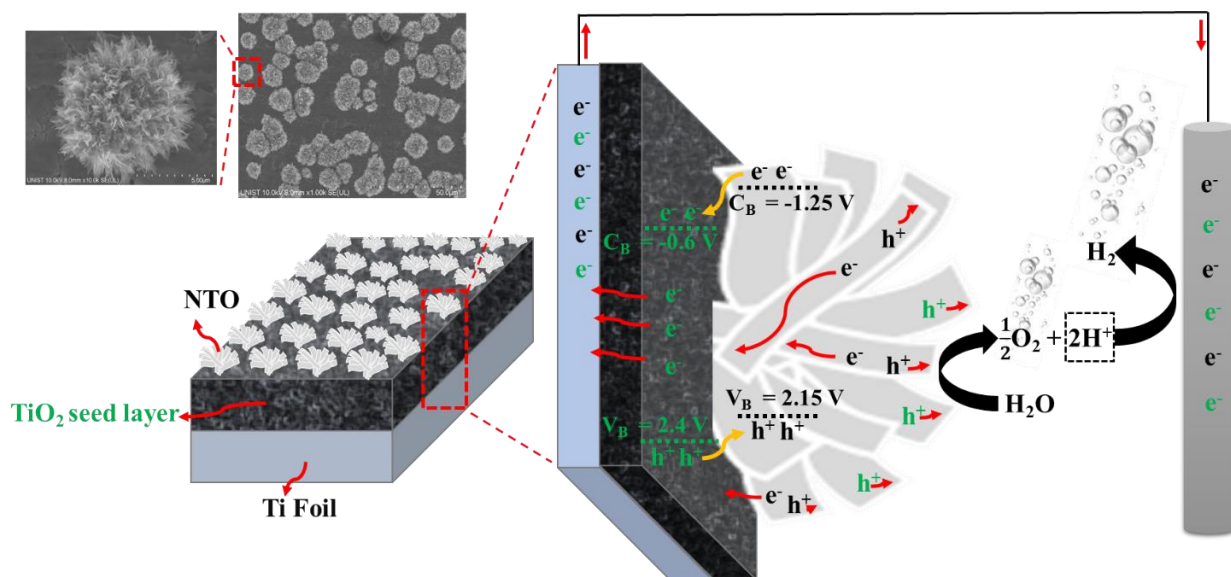


Figure 4. 18. Possible transfer mechanism of photogenerated charge carriers in 500°C-6h+H2M photoanode

#### 4.4. Conclusions

This study optimized growth parameters including Ti source (Ti foil or  $\text{TiO}_2$  thin layer) and NaOH concentration during the hydrothermal process to synthesize a new  $\text{Ti}/\text{TiO}_2/\text{Na}_2\text{Ti}_3\text{O}_7$  photoelectrode (500°C-6h+H2M) with great adhesion of two phases and their direct contact with

the Ti foil. As a result, the synthesized photoelectrode showed a photocurrent density of around 0.46 mA/cm<sup>2</sup> V versus Ag / AgCl, which was 9.2 and 2.4 times higher than the pure Ti/Na<sub>2</sub>Ti<sub>3</sub>O<sub>7</sub> (Ti+H0.25M) and Ti/TiO<sub>2</sub> (500°C-6h) samples, respectively. More interestingly, this photoanode retained its initial photocurrent density even after 16 h, which was a great improvement compared to the FTO/Na<sub>2</sub>Ti<sub>3</sub>O<sub>7</sub> (powder form) photoanode reported in previous studies. Furthermore, the onset potential was shifted to a more negative voltage around -0.6 V vs Ag/AgCl for the 500°C-6h+H2M sample compared to -0.3 V for 500°C-6h and Ti+H0.25M. This significant improvement in photocurrent density corresponds to the type II heterojunction between Na<sub>2</sub>Ti<sub>3</sub>O<sub>7</sub> and TiO<sub>2</sub> and their great contact with the Ti foil, facilitating the separation and transfer of photogenerated electrons and holes. In further investigation, to confirm the role of type II heterojunction for efficient photogenerated charge carrier separation in the Ti/TiO<sub>2</sub>/Na<sub>2</sub>Ti<sub>3</sub>O<sub>7</sub> photoanode system, we applied an acid treatment (ion exchange) and then calcination treatment at different temperatures. The combined treatments converted the Na<sub>2</sub>Ti<sub>3</sub>O<sub>7</sub> phase in the Ti/TiO<sub>2</sub>/Na<sub>2</sub>Ti<sub>3</sub>O<sub>7</sub> photoanode to TiO<sub>2</sub>, which decreased its PEC performance. This performance reduction is attributed to forming a pure TiO<sub>2</sub> phase in the Ti/ TiO<sub>2</sub>/TiO<sub>2</sub> photoanode.

## Reference:

- [1] M. Tayebi, A. Tayyebi, Z. Masoumi, B.-K. Lee, Photocorrosion suppression and photoelectrochemical (PEC) enhancement of ZnO via hybridization with graphene nanosheets, *Applied Surface Science*, 502 (2020) 144189.
- [2] Z. Masoumi, M. Tayebi, B.-K. Lee, The role of doping molybdenum (Mo) and back-front side illumination in enhancing the charge separation of  $\alpha$ -Fe<sub>2</sub>O<sub>3</sub> nanorod photoanode for solar water splitting, *Solar Energy*, 205 (2020) 126-134.
- [3] Z. Masoumi, M. Tayebi, B.-K. Lee, Ultrasonication-assisted liquid-phase exfoliation enhances photoelectrochemical performance in  $\alpha$ -Fe<sub>2</sub>O<sub>3</sub>/MoS<sub>2</sub> photoanode, *Ultrasonics sonochemistry*, 72 (2021) 105403.
- [4] M. Tayebi, B.-K. Lee, Recent advances in BiVO<sub>4</sub> semiconductor materials for hydrogen production using photoelectrochemical water splitting, *Renewable and Sustainable Energy Reviews*, 111 (2019) 332-343.
- [5] J. Gao, Q. Shen, R. Guan, J. Xue, X. Liu, H. Jia, Q. Li, Y.J.J.o.C.U. Wu, Oxygen vacancy self-doped black TiO<sub>2</sub> nanotube arrays by aluminothermic reduction for photocatalytic CO<sub>2</sub> reduction under visible light illumination, 35 (2020) 205-215.
- [6] Q. Shen, J. Xue, Y. Li, G. Gao, Q. Li, X. Liu, H. Jia, B. Xu, Y. Wu, S.J.J.A.C.B.E. Dillon, Construction of CdSe polymorphic junctions with coherent interface for enhanced photoelectrocatalytic hydrogen generation, 282 (2021) 119552.
- [7] L. Wang, W. Si, X. Hou, M. Wang, X. Liu, Y. Ye, F. Hou, J.J.S.M. Liang, Technologies, Novel integrated strategies toward efficient and stable unassisted photoelectrochemical water splitting, (2020) e00209.
- [8] H. Fattahimoghaddam, T. Mahvelati-Shamsabadi, B.-K.J.J.o.H.M. Lee, Efficient photodegradation of rhodamine B and tetracycline over robust and green g-C<sub>3</sub>N<sub>4</sub> nanostructures: supramolecular design, 403 (2021) 123703.
- [9] M. Razavi-Esfali, T. Mahvelati-Shamsabadi, H. Fattahimoghaddam, B.-K.J.C.E.J. Lee, Highly efficient photocatalytic degradation of organic pollutants by mesoporous graphitic carbon nitride bonded with cyano groups, 419 (2021) 129503.
- [10] M. Shahrezaei, A.A. Babaluo, S. Habibzadeh, M.J.E.J.o.I.C. Haghighi, Photocatalytic properties of 1D TiO<sub>2</sub> nanostructures prepared from polyacrylamide gel–TiO<sub>2</sub> nanopowders by hydrothermal synthesis, 2017 (2017) 694-703.
- [11] M. Shahrezaei, S. Habibzadeh, A.A. Babaluo, H. Hosseinkhani, M. Haghighi, A. Hasanzadeh, R.J.J.o.E.N. Tahmasebpour, Study of synthesis parameters and photocatalytic activity of TiO<sub>2</sub> nanostructures, 12 (2017) 45-61.
- [12] M. Tayebi, Z. Masoumi, B.-K. Lee, Ultrasonically prepared photocatalyst of W/WO<sub>3</sub> nanoplates with WS<sub>2</sub> nanosheets as 2D material for improving photoelectrochemical water splitting, *Ultrasonics sonochemistry*, 70 (2021) 105339.
- [13] M. Tayebi, B.-K. Lee, The effects of W/Mo-co-doped BiVO<sub>4</sub> photoanodes for improving photoelectrochemical water splitting performance, *Catalysis Today*, 361 (2021) 183-190.
- [14] M. Tayebi, A. Tayyebi, B.-K. Lee, C.-H. Lee, D.-H. Lim, The effect of silver doping on photoelectrochemical (PEC) properties of bismuth vanadate for hydrogen production, *Solar Energy Materials and Solar Cells*, 200 (2019) 109943.
- [15] M. Tayebi, M. Kolaei, A. Tayyebi, Z. Masoumi, Z. Belbasi, B.-K.J.S.E. Lee, Reduced graphene oxide (RGO) on TiO<sub>2</sub> for an improved photoelectrochemical (PEC) and photocatalytic activity, 190 (2019) 185-194.
- [16] J. Gao, J. Xue, S. Jia, Q. Shen, X. Zhang, H. Jia, X. Liu, Q. Li, Y.J.A.A.M. Wu, Interfaces, Self-Doping Surface Oxygen Vacancy-Induced Lattice Strains for Enhancing Visible Light-Driven Photocatalytic H<sub>2</sub> Evolution over Black TiO<sub>2</sub>, 13 (2021) 18758-18771.

- [17] S.P. Vattikuti, P.A.K. Reddy, P. Nagajyothi, J. Shim, C.J.J.o.A. Byon, Compounds, Hydrothermally synthesized Na<sub>2</sub>Ti<sub>3</sub>O<sub>7</sub> nanotube–V<sub>2</sub>O<sub>5</sub> heterostructures with improved visible photocatalytic degradation and hydrogen evolution-Its photocorrosion suppression, 740 (2018) 574-586.
- [18] M. Kolaei, M. Tayebi, B.-K.J.A.S.S. Lee, The synergistic effects of acid treatment and silver (Ag) loading for substantial improvement of photoelectrochemical and photocatalytic activity of Na<sub>2</sub>Ti<sub>3</sub>O<sub>7</sub>/TiO<sub>2</sub> nanocomposite, 540 (2021) 148359.
- [19] H. Zhang, P. Liu, H. Wang, H. Yu, S. Zhang, H. Zhu, F. Peng, H.J.L. Zhao, Facile formation of branched titanate nanotubes to grow a three-dimensional nanotubular network directly on a solid substrate, 26 (2010) 1574-1578.
- [20] H. Pan, X. Qiu, I.N. Ivanov, H.M. Meyer, W. Wang, W. Zhu, M.P. Paranthaman, Z. Zhang, G. Eres, B.J.A.C.B.E. Gu, Fabrication and characterization of brookite-rich, visible light-active TiO<sub>2</sub> films for water splitting, 93 (2009) 90-95.
- [21] M. Shahrezaei, S.M.H. Hejazi, Y. Rambabu, M. Vavrecka, A. Bakandritsos, S. Oezkan, R. Zboril, P. Schmuki, A. Naldoni, S.J.C. Kment, Multi-Leg TiO<sub>2</sub> Nanotube Photoelectrodes Modified by Platinized Cyanographene with Enhanced Photoelectrochemical Performance, 10 (2020) 717.
- [22] G. Liu, G. Zhao, W. Zhou, Y. Liu, H. Pang, H. Zhang, D. Hao, X. Meng, P. Li, T.J.A.F.M. Kako, In situ bond modulation of graphitic carbon nitride to construct p–n homojunctions for enhanced photocatalytic hydrogen production, 26 (2016) 6822-6829.
- [23] M. Kolaei, M. Tayebi, Z. Masoumi, A. Tayyebi, B.-K.J.E.S.N. Lee, Decoration of CdS nanoparticles on dense and multi-edge sodium titanate nanorods to form a highly efficient and stable photoanode with great enhancement in PEC performance, (2021).
- [24] A. Turki, H. Kochkar, C. Guillard, G. Berhault, A.J.A.C.B.E. Ghorbel, Effect of Na content and thermal treatment of titanate nanotubes on the photocatalytic degradation of formic acid, 138 (2013) 401-415.
- [25] X. Zhu, A. Anzai, A. Yamamoto, H.J.A.C.B.E. Yoshida, Silver-loaded sodium titanate photocatalysts for selective reduction of carbon dioxide to carbon monoxide with water, 243 (2019) 47-56.
- [26] L.K. Dhandole, H.-S. Bae, H.-S. Chung, W.-S. Chae, M. Cho, J.S.J.I. Jang, E.C. Research, Dual CdS Nanoparticle-Deposited Vertically Aligned Titanate Nanotube Heterostructure Photoanode, 59 (2020) 9488-9499.
- [27] S. Phomma, T. Wutikhun, P. Kasamechonchung, T. Eksangsri, C.J.A.S. Sapcharoenkun, Effect of calcination temperature on photocatalytic activity of synthesized TiO<sub>2</sub> nanoparticles via wet ball milling sol-gel method, 10 (2020) 993.
- [28] F. Scarpelli, T.F. Mastropietro, T. Poerio, N.J.T.D.-M.f.a.S.E. Godbert, Mesoporous TiO<sub>2</sub> thin films: State of the art, 508 (2018).
- [29] T. Theivasanthi, M.J.a.p.a. Alagar, Titanium dioxide (TiO<sub>2</sub>) nanoparticles XRD analyses: an insight, (2013).
- [30] W.-C. Peng, Y.-C. Chen, J.-L. He, S.-L. Ou, R.-H. Horng, D.-S.J.S.r. Wu, Tunability of p-and n-channel TiO<sub>x</sub> thin film transistors, 8 (2018) 1-11.
- [31] C. Liu, J.-y. Liang, R.-r. Han, Y.-z. Wang, J. Zhao, Q.-j. Huang, J. Chen, W.-h.J.P.C.C.P. Hou, S-doped Na<sub>2</sub>Ti<sub>6</sub>O<sub>13</sub>@TiO<sub>2</sub> core–shell nanorods with enhanced visible light photocatalytic performance, 17 (2015) 15165-15172.
- [32] S.G. Babu, R. Vinoth, D.P. Kumar, M.V. Shankar, H.-L. Chou, K. Vinodgopal, B.J.N. Neppolian, Influence of electron storing, transferring and shuttling assets of reduced graphene oxide at the interfacial copper doped TiO<sub>2</sub> p–n heterojunction for increased hydrogen production, 7 (2015) 7849-7857.
- [33] V. Jokanović, N. Bundaleski, B. Čolović, M. Ferrara, B. Jokanović, I.J.Z.m. Nasov, Detailed characterization of the Ti-O based thin films obtained by cathodic arc evaporation, 62 (2021) 41-50.
- [34] K. Wang, B. Liu, J. Li, X. Liu, Y. Zhou, X. Zhang, X. Bi, X.J.J.o.m.s. Jiang, technology, In-situ synthesis of TiO<sub>2</sub> nanostructures on Ti foil for enhanced and stable photocatalytic performance, 35 (2019) 615-622.

- [35] R. Wang, L. Wang, Y. Zhou, Z.J.A.C.B.E. Zou, Al-ZnO/CdS photoanode modified with a triple functions conformal TiO<sub>2</sub> film for enhanced photoelectrochemical efficiency and stability, 255 (2019) 117738.
- [36] M. Tayebi, A. Tayyebi, B.-K. Lee, Photocharged molybdenum-doped BiVO<sub>4</sub> photoanodes for simultaneous enhancements in charge transport and surface passivation, Solar Energy, 191 (2019) 427-434.
- [37] M. Tayebi, A. Tayyebi, T. Soltani, B.-K. Lee, pH-Dependent photocatalytic performance of modified bismuth vanadate by bismuth ferrite, New Journal of Chemistry, 43 (2019) 9106-9115.
- [38] Z. Masoumi, M. Tayebi, M. Kolaei, A. Tayyebi, H. Ryu, J.I. Jang, B.-K.J.A.A.M. Lee, Interfaces, Simultaneous Enhancement of Charge Separation and Hole Transportation in a W:  $\alpha$ -Fe<sub>2</sub>O<sub>3</sub>/MoS<sub>2</sub> Photoanode: A Collaborative Approach of MoS<sub>2</sub> as a Heterojunction and W as a Metal Dopant, 13 (2021) 39215-39229.
- [39] M. Kolaei, M. Tayebi, B.-K. Lee, The synergistic effects of acid treatment and silver (Ag) loading for substantial improvement of photoelectrochemical and photocatalytic activity of Na<sub>2</sub>Ti<sub>3</sub>O<sub>7</sub>/TiO<sub>2</sub> nanocomposite, Applied Surface Science, 540 (2021) 148359.



## Conclusion

In this thesis, we examined the effect of 4 strategies (acidic treatment with the assistance of ultrasonic waves, loading of noble metal, heterojunction with visible semiconductor, and optimization of NaOH concentration) to improve the photocatalytic and photoelectrochemical activity of sodium titanate for efficient degradation of organic pollutant and hydrogen production.

The acid treatment with different concentrations of HCl aqueous solution (0.01, 0.05, and 0.1M) under ultrasonic irradiation at 50°C and the Ag loading (0.3, 0.5, 1, and 2 wt%) by the impregnation method on the Na<sub>2</sub>Ti<sub>3</sub>O<sub>7</sub>/TiO<sub>2</sub> nanocomposite greatly improved the PEC performance and the photodegradation of RhB in aqueous solution. The acid treatment with HCl 0.1M led to a desirable loss of nanotubular structure along with the emergence of titania plate-like nanoparticles on the surface of hydrogen titanate nanotubes. The nanocomposite with the surface properties of the TiO<sub>2</sub> nanocrystal and the high surface area of titanate nanotubes showed a remarkable increase in photocatalytic activity under visible light irradiation. The acid treated NTOH0.1 showed 64.5% higher photodegradation activity than that of the untreated catalyst after 120 min. This enhancement is attributed to the removal of Na<sup>+</sup> as a recombination center of e<sup>-</sup> and h<sup>+</sup>, improving the crystallinity of the photocatalyst, enhancing the visible light absorption, and increasing the surface area during the acid treatment process. The NTOH0.1/Ag0.5 nanocomposite with the optimized acid treatment and silver loading showed 97.3% photodegradation of RhB after 60 min irradiation, which was 82.6% higher than that of the pristine catalyst, due to a combination of the acid treatment effect and the greatly enhanced surface plasmon effect of silver on the photocatalyst. The NTOH0.1/Ag0.5 photoanode also showed 2.7 times higher photocurrent density than that of the untreated photoanode.

Sodium titanate nanorods with multi-step edges synthesized on the surface of Ti foil as the substrate were favorite places for deposition of CdS nanoparticles with suitable band alignment to efficiently extend the absorption edge of the NTO into visible light region. The NTO photoanode deposited with CdS nanoparticles using 12 SILAR cycles (NTO/CdS12 heterostructure) showed highest PEC performance, compared to the pristine NTO and other NTO/CdS<sub>x</sub> photoanodes. The photocurrent density of the NTO/CdS12 photoanode was 2.37 mA/cm<sup>2</sup> at 1 V vs. RHE which was 36 times higher than that of the pure NTO photoanode. The NTO/CdS12 photoelectrode retained more than 95% of its initial photocurrent, even after 6,000 s of light irradiation. The noticeable improvement in PEC performance of NTO/CdS<sub>x</sub> photoanodes and their great stability can be attributed to the type II heterojunction between CdS and NTO and outstanding connection between CdS nanoparticles and NTO nanorods with multi-stage edges and Ti substrate that facilitate the transfer of photogenerated electrons to the surface of Ti substrate.

Finally, we optimized growth parameters including Ti source (Ti foil or TiO<sub>2</sub> thin layer) and NaOH concentration during the hydrothermal process to synthesize a new Ti/TiO<sub>2</sub>/Na<sub>2</sub>Ti<sub>3</sub>O<sub>7</sub> photoelectrode (500°C-6h+H<sub>2</sub>M) with great adhesion of two phases and their direct contact with the Ti foil. As a result, the synthesized photoelectrode showed a photocurrent density of around 0.46 mA/cm<sup>2</sup> V versus Ag / AgCl, which was 9.2 and 2.4 times higher than the pure Ti/Na<sub>2</sub>Ti<sub>3</sub>O<sub>7</sub> (Ti+H<sub>0.25</sub>M) and Ti/TiO<sub>2</sub> (500°C-6h) samples, respectively. More interestingly, this photoanode retained its initial photocurrent density even after 16 h, which was a great improvement compared to the FTO/Na<sub>2</sub>Ti<sub>3</sub>O<sub>7</sub> (powder form) photoanode reported in previous studies. This significant improvement in photocurrent density corresponds to the type II heterojunction between Na<sub>2</sub>Ti<sub>3</sub>O<sub>7</sub> and TiO<sub>2</sub> and their great contact with the Ti foil, facilitating the separation and transfer of photogenerated electrons and holes. In further investigation, to confirm the role of type II

heterojunction for efficient photogenerated charge carrier separation in the Ti/TiO<sub>2</sub>/Na<sub>2</sub>Ti<sub>3</sub>O<sub>7</sub> photoanode system, we applied an acid treatment (ion exchange) and then calcination treatment at different temperatures. The combined treatments converted the Na<sub>2</sub>Ti<sub>3</sub>O<sub>7</sub> phase in the Ti/TiO<sub>2</sub>/Na<sub>2</sub>Ti<sub>3</sub>O<sub>7</sub> photoanode to TiO<sub>2</sub>, which decreased its PEC performance. This performance reduction is attributed to forming a pure TiO<sub>2</sub> phase in the Ti/ TiO<sub>2</sub>/TiO<sub>2</sub> photoanode.